UiT
THE ARCTIC UNIVERSITY OF NORWAY

Faculty of Science and Technology
Department of Physics and Technology

Measuring Wind Using the Internal Stabilisation System of a Quadrotor Drone

—

Magdalena Simma
FYS-3900 Master thesis in physics, May 2018

"Imagination is more important than knowledge.
Knowledge is limited. Imagination encircles the world."
- Albert Einstein, 1929

Abstract

This thesis proposes a method of measuring wind using the data logged by the autopilot of a quadrotor drone. The approach is fundamentally different from other attempts found in the literature. Theoretical equations from works on quadrotor control are utilised and supplemented to form the theoretical framework. Static thrust tests provide the necessary parameters for calculating wind estimates. Flight tests are conducted at two different test sites with the quadrotor hovering next to a static 2D ultrasonic anemometer with wind speeds between 0 - 5 m/s. Estimated vertical wind speeds do not show the desired correlation. Horizontal wind estimates achieve exceptionally good results with RMSE values between 0.26 - 0.29 m/s for wind speed, and between 4.1° - 4.9° for wind direction, which is an improvement compared to the literature.

Acknowledgements

Firstly, I would like to thank my supervisors. Tobias Boström for providing the idea for this thesis and giving me valuable support and feedback while I was working on it. Håvard Mjøen for being my pilot and answering all my drone related questions.

Thank you to Pål Vevang for providing me with practical solutions for my experiments.

To Andreas Bjørkli-Eriksen and Tromsøhopp for giving me access to their ski jump tower and permission to fly there. Thank you for your trust.

A big thank you to Lars Erik for uncountable discussions about my project, extensive proofreading and your unlimited support.

Finally, I would like to thank my parents who have supported me in every possible way. Thank you for letting me choose my own path, even though it led me so far north.

Contents

List of Figures

List of Tables

Nomenclature

In this thesis, vectors are denoted with overhead arrows, while scalars are simple italic letters. An overhead dot symbolises a time derivative. The superscript T indicates a transposed matrix or vector. The subscripts x,y and z denote vector components in the BFF. The subscript h indicates the horizontal components x and y. The superscript VF specifies that the variable is in the vehicle frame.

α	Inclination angle of drone from vertical	[°]
β	Heading angle of drone relative to wind direction	[°]
Θ	Pitch angle	[°]
ρ	Air density	[kg/m^3]
σ_w	Standard deviation of wind speed	[m/s]
τ	Motor torque	[Nm]
Φ	Roll angle	[°]
Ψ	Yaw angle	[°]
Ω	Angular velocity of the drone	[rad/s]
ω	Rotational velocity of rotor	[rad/s]
$\dot{\omega}$	Rotor acceleration	[rad/s^2]
A	Area, cross section or area of the rotor disk	[m^2]
A_tot	Total rotor disk area of 4 propellers	[m^2]
$\vec{a}$	Specific acceleration	[m/s^2]
$\bar{c}$	Lumped linear drag coefficient	
$\hat{c}$	Coefficient including m, g, ρ, A	
c_1	$=8\rho A$	[kg/m]
c_D	Drag coefficient	
c_F	Lift coefficient	
c_T	Thrust coefficient	
d	Intercept of linear fit	[A]
E_kin	Kinetic energy	[J]
$\hat{e_\mathrm{z}}$	Unit vector in $z-$direction in BFF	
F	Force exerted by rotor	[N]
F_D	Drag force	[N]
F_G	Gravitational force	[N]
F_L	Lift force	[N]

FoM	Figure of merit	
f_{x}	Vehicle's lateral thrust	[N]
g	Gravitational acceleration	[m/s^2]
$\vec{H}$	Horizontal force induced by rotors	[J]
I	Moment of inertia of rotor blade	[kg m^2]
i	Motor current	[A]
i_{calc}	Calculated motor current	[A]
J	Advance ratio	
K_{r}	Matrix containing lumped drag coefficient	
K_{V}	Motor parameter	[rpm/V]
k	Inclination of linear fit	[A/V]
L	Length of air cylinder	[m]
l	Length of propeller	[m]
m	Mass of the drone	[kg]
m_{prop}	Mass of one propeller	[kg]
P_{a}	Aerodynamic power	[W]
P_{dissip}	Dissipated power	[W]
P_{el}	Electrical power	[W]
P_{H}	Power in horizontal force	[W]
P_{m}	Mechanical power applied to rotor	[W]
P_{r}	Power needed to rotate propeller	[W]
P_{T}	Power in thrust	[W]
P_{wind}	Power in the wind	[W]
$p_{\mathrm{U}}/p_{\mathrm{L}}$	Pressure above/below the rotor disk	[Pa]
p_{∞}	Pressure far up-/downstream of rotor disk	[Pa]
q	Linear momentum	[kg m/s]
$R_{\mathrm{v}}^{\mathrm{b}}$	Transformation matrix from VF to BFF	
T	Thrust force	[N]
TI	Turbulence intensity	
t	Time	[s]
U	Absolute value of induced velocity minus air velocity	[m/s]
V	Volume	[m^3]
v^{a}	Velocity of air at rotor disk	[m/s]
v^{i}	Induced velocity	[m/s]
v^{s}	Relative air velocity upstream in streamtube	[m/s]
v^{∞}	Velocity downstream in streamtube resulting from v^{i}	[m/s]
v_{a}	Air velocity	[m/s]
v_{g}	Ground velocity	[m/s]
v_{w}	Wind velocity	[m/s]
$\overline{v_{\mathrm{w}}}$	Mean wind velocity	[m/s]
v_{wt}	Wind tunnel flow speed	[m/s]

Glossary

2D Two Dimensional

3D Three Dimensional

ABL Atmospheric Boundary Layer

AC Alternating Current

AM Avinor Mast

BET Blade Element Theory

BFF Body Fixed Frame

CFD Computational Fluid Dynamics

DC Direct Current

DOP Dilution Of Precision

ESC Electronic Speed Controller

FoM Figure of Merit

GPS Global Positioning System

GS Ground Station

HAWT Horizontal Axis Wind Turbine

HDOP Horizontal Dilution Of Precision

IMU Inertial Measurement Unit

IRF Inertial Reference Frame

LIDAR LIght Detection And Ranging

MAF Moving Average Filter

PWM Pulse Width Modulation

RC Remote Control

RCOU pulse width modulated command sent from flight controller to the ESC/motor/RC output [7]

RMSE Root Mean Square Error

RPAS Remotely Piloted Aircraft System

RPM Rotations Per Minute

SJ Ski Jump

SODAR SOund Detection And Ranging

UAS Unmanned Aircraft System

UAV Unmanned Aerial Vehicle

VAWT Vertical Axis Wind Turbine

VF Vehicle Frame

Chapter 1

Introduction

1.1 Background

The trend towards renewable energy sources is present both in large but also in small scales. With the increasing power consumption which is highly localised in cities, power generation in urban areas becomes a topic of importance. Wind turbines which can be installed on the roofs of buildings have started to be considered as an energy source for urban areas as they provide renewable and affordable energy.

Urban areas hold some special challenges for the installation of wind turbines. The wind does not reach very high speeds and the airflow is highly dependent on the structure of surrounding buildings. Additionally, turbulence can be rather predominant. Thus, analysing the wind profile on site when considering the positioning of a small scale wind turbine is critical. Computational Fluid Dynamics (CFD) provides a widely used method for this. A digital model of the buildings and structures surrounding the proposed site needs to be created. Anemometer measurements from the area provide values of generally predominant wind speeds and directions. Those can then be put into a CFD model simulating the flow of the air around the digitally modelled buildings and structures. Turbulent areas as well as promising sites can be detected based on such simulations.

Nevertheless, a means of supplementing those simulations with actual local measurements would be desirable. Using anemometers for this task proves to be tricky as most instruments are either too expensive for the purpose or are not easily moveable. Furthermore, the process of acquiring reasonable data would be quite cumbersome.

1.2 Idea and Objectives

The idea for this thesis was conceived by Boström in 2015 when he saw a quadrotor drone flying around campus. Modern quadrotors contain an internal stabilisation system which is constantly counteracting the effects of the wind. By accessing the data of this autopilot, a measure for the local behaviour of the air should be derivable. The original idea was to get an empirical turbulence estimate based on the internal gyroscope measurements of the quadrotor. As turbulence can be considered as a measure of the variability of wind over time, research was made into measuring wind with a drone. Several accounts can be found where wind was measured with a fixed wing drone or with a measurement device mounted on a drone. The first is not practical in an urban environment since a fixed wing drone has to keep moving in order to stay airborne. The latter is problematic due to the drone-induced air stream which can disturb the measurements.

A few papers explore the options of measuring wind using the internal stabilisation system of a quadrotor. However, those accounts mainly focus on measuring horizontal wind only. The aim for this thesis is therefore to develop a measurement system that can measure the local wind velocity in three dimensions with the use of a quadrotor.

Another objective is the repeatability of the method. This means that another person owning the same quadrotor model should be able to use the measurement method easily without having to modify the drone in any way.

1.3 Significance

A wind measurement system that is based purely on the data acquired by flying with a quadrotor has several advantages. The mobility of the measuring system is not a problem and estimates can be taken from any desired spot. Also, quadrotors are easily accessible with prices being comparatively low. Additionally, they are widely researched and thus constantly improving their reliability and controllability. Consequently a good measurement system based on a quadrotor could be a valuable asset when considering where to place a wind turbine.

Since the idea for this thesis came up, it has been realised that wind energy might not be a very suitable solution for urban areas after all. However, the proposed measurement system is just as applicable in many other scenarios where it can be valuable. Wind conditions can be locally mapped in detail for design purposes of buildings, bridges or other infrastructure. Other practical purposes can be finding sweet spots for large wind power plants

in complex terrain or analysing the wind conditions in cities to model and predict the accumulation of snow.

1.4 Structure of the Thesis

The thesis contains seven chapters: introduction, theory, literature review, method, results, discussion and conclusion.

Chapter 2 provides the theoretical explanations and equations needed to understand the method developed in the course of the thesis. The four parts focus on wind theory, drone theory, aerodynamic theory and aviation theory.

Chapter 3 presents published works related to measuring wind with a quadrotor drone. Special attention is given to a paper by Allibert et. al. [6] which provides theoretical equations forming the foundation for the developed method.

Chapter 4 starts by explaining the proposed measurement method theoretically. It further describes the conduction of static and flight tests and elaborates on how the data from the quadrotor is analysed.

Chapter 5 presents the quadrotor estimated wind velocities from the test flights, compared to the actual measurements by the anemometer.

Chapter 6 then provides a discussion on the results, their accuracy and possible reasons for the deviations seen.

Chapter 7 summarises the results, discusses limitations of the method and proposes improvements and further work.

Chapter 2

Theory

2.1 Wind Theory

2.1.1 Wind and Turbulence

Due to the Earth's curvature, horizontal areas at different latitudes receive a different amount of solar radiation resulting in the air near the equator being warmer than at higher latitudes as well as the pressure varying. This induces the air masses in the atmosphere to move, creating a large scale wind system defined by the Hadley ($0° - 30°$ latitude), Ferrell ($30° - 60°$ latitude) and Polar cell ($60° - 90°$ latitude). Within these cells a circulation of air masses takes place due to the different temperatures and pressure as well as the air cooling off or warming up when moving to a different latitude. Additionally, the Coriolis effect induced by the Earth's rotation causes lateral air movements towards the east and west. On a smaller scale the wind pattern is influenced by local zones of high or low pressure, the Earth's surface structure as well as day and night variations due to varying heating capacities of different surfaces. [17]

At high altitudes the air can flow undisturbed at high velocities while the movement of air close to the ground is governed by friction. Vertical wind profiles can be established from fluid dynamics where the wind speed at ground level is generally assumed to be zero. Both the Log Law and the Power Law provide models for how the horizontal wind speed increases with height in steady flow over open areas [27].

In urban areas the wind is disturbed by buildings which block and redirect the airflow. This gives rise to turbulent areas where the flow is not laminar. Directly behind a building or other structure, the air can be redirected into a circular motion around an axis. This is called a rotor. Variations in wind

speed and direction that occur stochastically within a time period of less than 10 minutes are termed turbulence. Turbulence arises when kinetic energy in the wind is dissipated to thermal energy creating a cascade of eddies. This is a chaotic movement hard to describe by theory. A measure of turbulence is therefore given by a statistical analysis. The turbulence intensity TI is defined as

$$TI = \frac{\sigma_{\mathrm{w}}}{\overline{v_{\mathrm{w}}}} \tag{2.1}$$

where σ_{w} denotes the standard deviation of the wind speed and $\overline{v_{\mathrm{w}}}$ is the mean wind speed calculated over a time period of usually 10 minutes. The turbulence intensity typically lies between $0.1 - 0.4$. [27]

The power in the wind, which can be extracted via wind turbines, can be derived from the kinetic energy E_{kin}. [31]

$$E_{\mathrm{kin}} = \frac{1}{2}\, m\, v^2 \tag{2.2}$$

The power, which is the kinetic energy over time t, is thus given by

$$P_{\mathrm{wind}} = \frac{E_{\mathrm{kin}}}{t} = \frac{1}{2}\,\frac{m\, v^2}{t}. \tag{2.3}$$

Since the mass of air is air density ρ times volume V, it can be written as

$$m = \rho\, V = \rho\, A\, L = \rho\, A\, v_{\mathrm{w}}\, t, \tag{2.4}$$

where A is the area swept by the wind turbine and L is the length of the air cylinder passing through. Inserting into equation (2.3) results in

$$P_{\mathrm{wind}} = \frac{1}{2}\, \rho\, A\, v_{\mathrm{w}}^3. \tag{2.5}$$

2.1.2 Wind Measurement Devices

Instruments for measuring wind speed are commonly called anemometers. They come in a variety of forms based on different working principles. This section gives a short introduction to the most common ones, some of which can be seen in figure 2.1.

Two instruments that work with momentum transfer are cup anemometers and propeller anemometers. These sensors are simple, sensitive and relatively cheap. However they are also easily affected by environmental impacts such as dust or icing which alter their rotational ability.

A **cup anemometer** consists of typically three cups mounted to a vertical axis. The cups, catching the wind, rotate around this axis and from the angular velocity the wind speed can be derived. For turbulence measurements

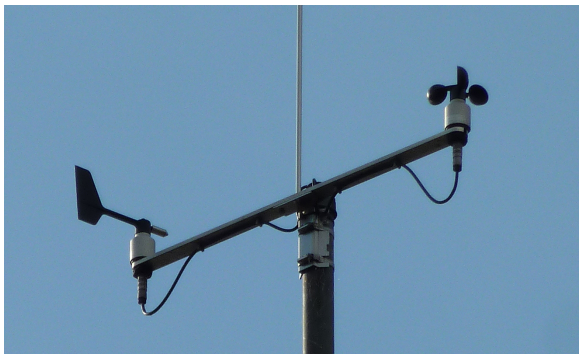

Cup Anemometer with Wind Vane

2D Ultrasonic Anemometer

Figure 2.1: Different types of anemometers [Photos: Simma]

small and lightweight sensors with little friction can be used. However, these anemometers only give horizontal wind speed.

A **propeller anemometer** consists of a propeller mounted onto a shaft. When wind is blowing onto the propeller, it rotates together with the shaft which drives a small generator. Propeller anemometers generally have a fast response and can be used in a configuration of three orthogonally placed anemometers to measure three dimensional (3D) wind speeds.

Both the cup and the propeller anemometer are commonly used in combination with a **wind vane**. This is a tail-shaped plate rotating around a vertical axis. In windy conditions it will always be in a downwind position, therefore giving an indication of wind direction. [27]

A **hot wire anemometer** consists of a thin wire made of platinum or tungsten. An electric current through the wire heats it to a temperature above ambient. Wind blowing past the wire cools it down which in turn affects the resistance in the wire. The resistance can thus be used to estimate the wind speed. Since hot wire anemometers are highly sensitive with a high frequency response and a good spatial resolution, they can be used for measuring turbulent flows. They are however quite fragile, orientation sensitive and not the cheapest. [36]

A **sonic anemometer** uses ultrasonic sound waves to measure both wind speed and direction. It consists of up to three pairs of transducers between which sonic pulses traverse. The time of flight is thereby dependent on the movement of the air within the anemometer, thus giving a measure for wind. Sonic anemometers exist in two dimensional (2D) configurations with two transducer pairs as well as in 3D configurations using three pairs. They can

also be used to measure turbulence with a time resolution of up to 20 Hz. [27]

Another category of anemometers are Doppler sensors which classify as remote sensing systems since they don't require a sensor at the actual point of interest for the measurement. High and expensive towers to mount wind sensors on are therefore not needed.

The **SOund Detection And Ranging (SODAR)** system works with acoustic backscattering from particles in the atmosphere. Acoustic signals are sent in an almost vertical direction and microphones detect the backscattered signal. The height of the measurement is determined from the travel time between emitting and receiving the signal. Motions of the air perpendicular to the direction of emittance result in a Doppler shift in the acoustic frequency of the scattered signal. This can be used to determine the wind speed. By using three simultaneous signals at different angles, 3D wind measurements can be conducted up to 300 m above land. However, these sensors have some issues, one of them being difficulties in measuring wind speeds below 4 m/s and above 18 m/s which limits their applicability. [27]

The **LIght Detection And Ranging (LIDAR)** system works on a very similar principle to that of the SODAR. It emits beams of light which interact with the air. The backscattered light is detected and the Doppler shift, which occurs due to backscattering by aerosols that move with the wind, is measured. Wind speed can therefore be determined up to around 200 m above ground and by sweeping the emitted beam around a circular path, 3D wind can be mapped. [27]

2.1.3 Wind Turbines

The idea of harvesting wind energy for practical applications has been investigated for about 4000 years [17] and several different implementations have been invented. Devices producing electrical energy from wind are generally called wind turbines. Beside the large scale wind turbines used in energy parks, a variety of small scale wind turbines is available. Those are more feasible to install in urban areas, especially on top of buildings.

According to equation (2.5) the power in the wind increases cubically with the wind speed. It is therefore desirable to position a wind turbine in a place of relatively high wind speeds, which often means high above the ground. A typical large scale wind turbine has a cut-in wind speed of about 4 m/s below which it does not produce any electricity. Above that the produced power increases with wind speed up to a shut-down wind speed of about 25 m/s at which the wind turbine is shut down to prevent damage. [17] In general a highly laminar flow is ideal for power production. Turbulent


Figure 2.2: Left: HAWT, Right: VAWT, Images with permission from [25]

air flow will not only lower the efficiency of the wind turbine but also cause additional stress on the airfoils which might lead to damage. [27]

There are two types of wind turbine configurations as shown in figure 2.2. A horizontal axis wind turbine (HAWT) stands with the horizontal rotation axis against the wind ("axial flow") while a vertical axis wind turbine (VAWT) has its rotational axis perpendicular to the wind ("cross flow"). [17]

HAWTs are the most common form of wind turbines used in electricity harvesting today. They usually have two to three blades that are rotating quite fast in order to interact with optimally all the air passing through the disk area which is swept by the rotor blades. Using a yaw mechanism, the top of the wind turbine can be adjusted so that the disk area stands directly against the wind.

VAWTs were first invented by Georges Darrieus in 1925. Their configuration with a vertical rotational axis and curved airfoils enables it to make use of wind from any horizontal direction without having to adjust the rotor position. This makes them more suitable for placement in slightly turbulent areas. However, it is not advisable to install wind mills in turbulent areas. One of the purposes of the method presented in this thesis is to find turbulent areas and rule them out as potential wind mill sites.

2.1.4 Wind Simulations

To characterise the air flow for a specific site, e.g. around a building, one can create 3D models of the site of interest and apply CFD to it. This will give a simulation of the flow behaviour for different input values like wind speed and direction. Those can be chosen based on an analysis of anemometer data at the site. Such an analysis commonly precedes the installation of wind turbines to ensure optimal placement. [24]

2.1.5 Urban Wind Power

The use of wind turbines for energy harvesting is not only confined to large scale power parks, but can also be applied to urban areas. As those usually have lower wind speeds, small scale wind turbines are used which also suit the more confined space. Additionally they are comparatively light and therefore easier to install on top of existing buildings. Wind turbines in urban areas may also profit from upwinds caused by houses or other structures, enhancing the wind velocity. Furthermore, roof mounted systems provide private persons or smaller companies with a means of producing their own energy. In combination with solar systems, energy can be harvested in various weather conditions.

Despite all those advantages, installing urban wind turbines comes with some challenges. The wind profile is highly dependent on the surrounding buildings making a detailed wind analysis a necessity for every case. Furthermore, turbulence intensities can be high which is not a favourable condition for energy harvesting. Even if an ideal position is found where the wind conditions are sufficiently laminar, the installation of a wind turbine might not be practical. The roof needs to be constructed in a way that supports the extra weight of the turbine. Additionally vibrations can cause fatigue in the building structure and noise emittance might be disturbing. Considering all of this, the usage of wind mills in urban areas unfortunately often is not feasible. [16]

2.2 Drone Theory

The use of the term drone (male bee) in context with unmanned flying vehicles dates back to the 1930s. A plane called "Queen Bee" was built that could fly without a pilot on board and was used as a target in gunnery training [4]. Today the terminology used for such vehicles is a bit more complex. When talking about a flying drone (as opposed to underwater or on-land drones) the term unmanned aereal vehicle (UAV) is used. To address the whole system including the ground station and controller one can use Unmanned Aircraft System (UAS) or Remotely Piloted Aircraft System (RPAS). UAVs can be divided into three subcategories. Fixed Wing UAVs are, as the name suggests, UAVs that resemble a plane with fixed wings. Helicopter UAVs resemble a traditional helicopter with one main rotor on top and a vertical rotor at the tail. In this thesis we are more concerned with multirotor UAVs, also called multicopters, which are rotorcrafts with multiple propellers. Depending on the amount and configuration of those they are often referred to as tricopters, quadcopters or quadrotors, hexacopters and octacopters. [10]

2.2.1 The IRIS$^+$ Quadrotor

Figure 2.3: 3DR IRIS$^+$ quadrotor [Photo: Simma]

The drone used in this thesis is the IRIS$^+$ quadrotor from 3DR shown in figure 2.3. Its four 3-phase brushless motors are set up in an X-configuration. The four propellers have a size and pitch of 9.5 inch and 4.5 inch respectively. The quadrotor has a weight of 1.371 kg and is powered by a 3 cell 5100 mAh Lithium Polymer battery. The drone can be used together with the Mission Planner ground station software which can be used to plan waypoints the drone then automatically visits. [29]

The flight controller used in the IRIS$^+$ is a 3DR Pixhawk Autopilot shown in figure 2.4. It takes the input given from the Remote Control (RC) or the Ground Station (GS) and passes on adequate signals to the four electronic speed controllers (see section 2.2.4) to control the four motors. The Pixhawk contains an assortment of sensors given in table 2.1. Using the readings from those sensors the Autopilot can autonomously stabilise the system in the air making the IRIS$^+$ very easy to fly. Using data from the Global Positioning System (GPS) the drone can be held in place keeping its position.

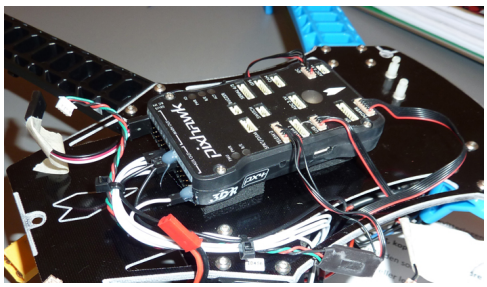

Figure 2.4: 3DR Pixhawk autopilot [Photo: Simma]

Table 2.1: List of sensors integrated in the Pixhawk [3]

Sensor	Model
Accelerometer and Gyroscope	Invensense MPU 6000 3-axis
Accelerometer and Magnetometer	ST Micro LSM303D 14 bit
Barometer	MEAS MS5611
Gyroscope	ST Micro L3GD20H 16 bit

2.2.2 Quick Guide to Flying a Quadrotor

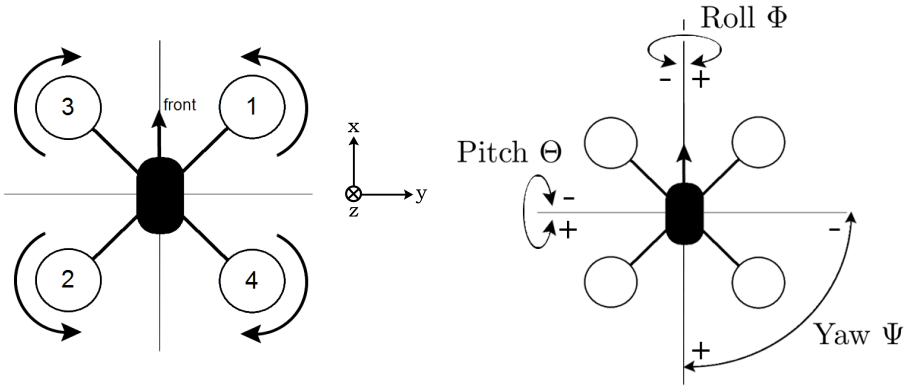

Figure 2.5: Left: Propeller configuration of a quadrotor drone with indication of the body fixed reference frame, Right: Roll, Pitch and Yaw angles.

Figure 2.5 shows the configuration of a typical quadrotor drone as well as the definitions of the roll, pitch and yaw angles. The quadrotor's four propellers are fixed to the X-shaped body of the drone where the box part contains all the sensors and control system. Would all of the rotors rotate in the same direction, the body of the quadrotor would experience a torque due to the propeller rotation causing the quadrotor to rotate about its z-axis. To ensure a zero net torque, two of the propellers therefore rotate counter clockwise (marked 1 and 2) while the other pair rotates clockwise (marked 3 and 4). To achieve hovering or pure vertical flight, all of the four propellers rotate with the same speed. By increasing the speed of the back rotors (2 and 4) while decreasing the speed of the front ones (1 and 3) a negative rotation around the drone's y-axis is achieved causing a negative pitch angle corresponding to a forward tilt of the quadrotor. The reverse of this will result in a positive pitch angle, i.e. backward tilt. Analogously a rotation around the drone's x-axis, i.e. changing the roll angle, can be achieved by different motor speeds for left (2 and 3) and right (1 and 4) propellers. For a rotation around the z-axis, i.e. change in yaw angle, the speed difference

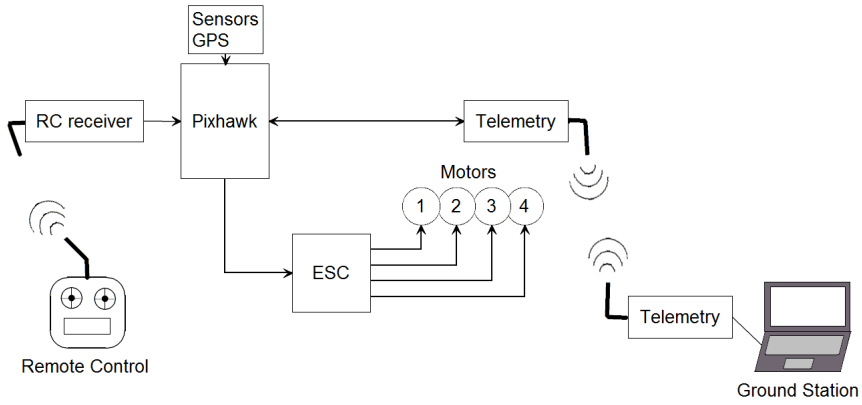

Figure 2.6: Scheme of the signal flow during a quadrotor operation. The control commands are sent from the RC to the RC receiver via a radio link. The Pixhawk interprets the commands together with the sensor readings to send RCOU signals to the ESC which in turn controls the four motors. A telemetry link between the drone and the ground station lets the pilot observe key variables in real time and also gives the option to control the quadrotor via the ground station.

between diagonal propeller pairs rotating clockwise (3 and 4) and counter clockwise (1 and 2) induces a torque about the z-axis.

When manually flying a quadrotor one does not control the four motors directly but rather provides input to the on-board flight controller about the desired attitude angles and throttle. Figure 2.7 shows a typical Remote Control used to manually fly a quadrotor. There are different modes, the RC can be used with, changing the assignment of the commands to the control sticks. In mode 2, which is normal in Europe, the left stick is used to control throttle (↕) and yaw angles (↔) while the right stick controls the pitch (↕) and roll angles (↔). The control signal from the RC is transmitted to the drone via a 2.4 GHz radio link (see figure 2.6). The Pixhawk autopilot then uses this input to calculate the amount of power each motor should receive.

Figure 2.7: Remote control: The left stick controls the throttle and yaw angle while the right stick controls pitch and roll angles. [Photo: Simma]

2.2.3 Flight Modes

To enable a more stable flight, quadrotors can be equipped with several sensors determining its position and attitude. A list of sensors contained in the IRIS$^+$ is given in table 2.1. Data from those sensors can be used by the flight controller to keep the drone's position or attitude constant and counteract disturbances, e.g. from wind. This makes the flight more smooth and easier for the pilot to control.

There is a series of preprogrammed flight modes which stabilise the drone differently in flight. The following is a list of the most relevant ones for this thesis [8].

- **Stabilise Mode**
  In this mode the drone is controlled manually via the RC. However, when the right control stick (roll and pitch) is released the flight controller automatically levels the drone, i.e. roll and pitch angles are zero. When flying in windy conditions, the drone would thus drift horizontally with the wind while its altitude and yaw angle can be controlled with the left control stick.

- **Altitude Hold**
  This mode levels the drone just like in the stabilise mode. However, if operated at 50 % throttle (e.g. when the left control stick is in a central position) this mode holds the drone at constant altitude utilising barometric measurements while pitch, roll and yaw are freely manoeuvrable by the pilot. Thus if both control sticks are released, the drone will hold its altitude while drifting with the wind. It should be noted though, that the quadrotor actually hold itself at a height of constant barometric pressure. This means that it will drift vertically, if the local pressure changes.

- **Loiter**
  With this mode the drone holds its current location, heading and altitude whenever the sticks on the RC are released (i.e. 50 % throttle). The horizontal position and attitude of the drone are hereby determined by the GPS and a magnetometer, while the barometric pressure determines the vertical position identical to the Altitude Hold mode. Disturbances from wind are counteracted by changes in the attitude of the drone.

- **Auto Mode**
  This mode enables the drone to follow a preprogrammed flight path defined by several waypoints.

2.2.4 From Pixhawk to Propeller

Figure 2.8 shows a sketch of the connection between the Pixhawk, the Electronic Speed Controller (ESC) and the motor with propeller.

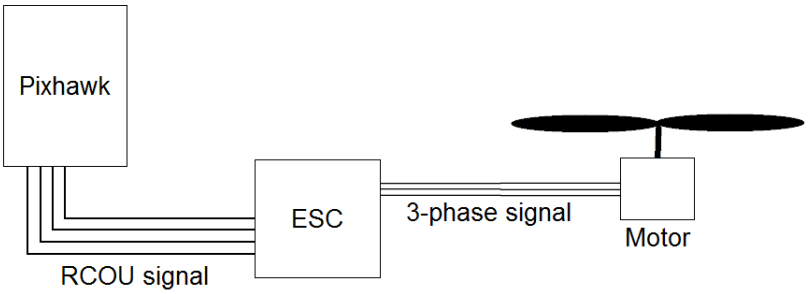

Figure 2.8: From Pixhawk to propeller - scheme of the electrical components

The RCOU signal is a pulse-width modulation (PWM) signal. The RCOU value lies between 1000 µs and 2000 µs and defines the pulse width in a 50 Hz signal. This value is produced by the Pixhawk autopilot and passed on to the ESC in order to control the four motors.

The ESC creates a three-phase alternating current (AC) signal to control the brushless electronic motor. It has the RCOU value as its input depending on which it controls the frequency of the output. The ESC gets its power from the on-board battery. [41]
On the IRIS+ quadrotor there is one central ESC that controls all four motors. This can be seen in figure 2.9.

The Rotations Per Minute (RPM) value is a measure of the rotational speed of the motor. This is controlled by the frequency of the three-phase power. It can be measured optically or with an rpm-sensor connected to the three-phase signal [1].

2.2.5 Data Stored by the Quadrotor

The data collected by the on-board sensors is stored in a log-file by the Pixhawk. Some of the data is transmitted to the ground station via a telemetry link so that variables like altitude, ground speed or battery voltage can be observed in real time. Table 2.2 lists some of the values the Pixhawk stores in its log-file. The data is collected in different groups each of which having a separate time vector. This is because data from different sensors are stored in different time intervals at different points in time. The time vectors for each group measure time in milliseconds from the insertion of the battery.

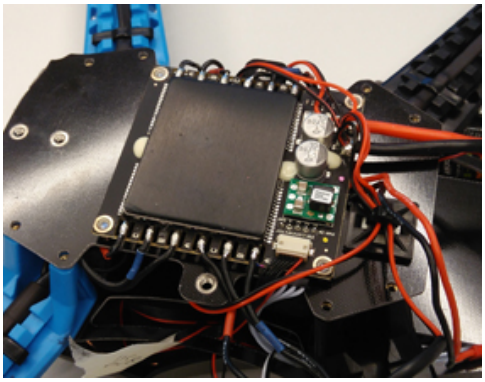

Figure 2.9: The ESC of the IRIS$^+$ [Photo: Simma]

Table 2.2: Relevant values stored in the Pixhawk log-file [7]

Group	Explanation	Variables stored
GPS	Data from GPS	time, latitude, longitude, altitude, ground speed, ground course, vertical velocity
ATT	Attitude	time, roll, pitch, yaw
IMU	Inertial Measurement Unit	time, 3D gyroscope, 3D accelerometer
RCOU	Remote Control Output	time, C1 (RCOU for motor 1), C2, C3, C4
CURR	Battery data	time, battery voltage, current drawn from battery
CTUN	Throttle & altitude info	time, altitude, barometric altitude, climb rate

2.2.6 GPS

To find the quadrotor's position with the Global Positioning System (GPS), signals from at least four satellites orbiting the earth are received. The distances to the satellites are then calculated from the time of flight and the position found from those through geometrical calculations [30]. The accuracy of the found position depends on the geometrical alignment of the used satellites which can be quantified by a dilution of precision (DOP) value. In the GPS data group stored by the Pixhawk, a value of horizontal dilution of precision (HDOP) is given. According to [7] a value of 1.5 is good, while values larger than 2 are not so good.

While the horizontal accuracy tends to be good, the vertical component has a larger error. This is because a GPS receiver can not connect to satellites below the horizon. Thus, the connected satellites are all on one side of the receiver, overhead, which affects the accuracy negatively.

2.3 Aerodynamic Theory

Describing the interaction between a propeller and its surrounding air is a very intricate task. Due to the rotation of the propellers, the rotor blades are exposed to varying relative wind speeds and incident angles over one revolution. Two main theories have been developed for rotors. Momentum theory models the rotor based on momentum transfer while Blade Element Theory looks at the aerodynamics of a small blade section. Before describing those theories in more detail in this section, an introdution to lift and drag is given.

2.3.1 Lift and Drag

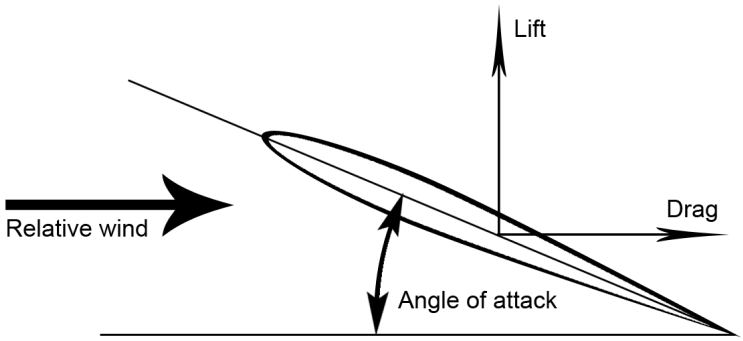

Figure 2.10: Lift and drag on an airfoil exposed to wind.

Lift and Drag are forces which describe the interaction of a solid object with a fluid, in this case air. Figure 2.10 shows an airfoil exposed to wind with the arrows indicating Lift and Drag forces. The drag force is acting in the same direction as the wind and effectively slows down the object. The drag equation is given by

$$F_{\mathrm{D}} = \frac{1}{2}\,\rho A c_{\mathrm{D}} v_{\mathrm{w}}^2 \tag{2.6}$$

where F_{D} is the drag force, ρ the air density, A the projected surface area of the airfoil which is exposed to the wind, c_{D} denotes the drag coefficient and v_{w} is the wind speed. [23]

The lift force is given by

$$F_{\mathrm{L}} = \frac{1}{2}\,\rho A c_{\mathrm{L}} v_{\mathrm{w}}^2 \tag{2.7}$$

where c_L is the lift coefficient. Lift acts perpendicular to the drag force. It arises from pressure differences on different sides of the airfoil due to the air passing at different speeds. For an airplane wing the air passing over the wing is moving faster than the air below the wing. This induces an area of lower pressure above the wing causing the wing to move upwards. In general the lift force is not necessarily upwards but perpendicular to the wind direction. [5]

The lift and drag coefficients are empirical values that depend on the shape of the object and have to be determined in wind tunnel tests.

2.3.2 Momentum Theory

To investigate the aerodynamics of a rotor blade and assess its basic performance, momentum theory can be applied. It makes the assumption of the rotor being an actuator disk which accelerates the air flowing through it. The resulting air flow forms a streamtube which can be seen in figures 2.11, 2.12 and 2.13 for different flight scenarios. This momentum change happening at the rotor disk generates a lifting force for which equations can be derived. The added velocity as the air moves through the rotor is the induced velocity v^{i}.

Momentum theory assumes the air to be incompressible as well as the flow being quasi-steady and one-dimensional. This means that the flow is assumed constant across the rotor disk while varying in the vertical direction. These assumptions imply that momentum theory will fail for certain flying conditions where the direction of the flow changes throughout the length of the streamtube. This can occur for example in rapid descent where vortices are created that envelope the whole rotor causing very unstable flight conditions. However, for the types of stable manoeuvres that are of interest for this thesis, momentum theory provides a good description. [39]

Hover [39]

Figure 2.11 shows the streamtube of a rotor in hover. The air far upstream has zero velocity while the air at the rotor has the induced velocity v^{i}. Far downstream the velocity is given by v^{∞}. A denotes the rotor disk area and A_2 the area of the streamtube far downstream. T is the thrust force induced by the rotor.

From the conservation of mass we can derive the following

$$\dot{m} = \rho A v^{\mathrm{i}} = \rho A_2 v^{\infty} \tag{2.8}$$

where m is the mass of the air and ρ is air density. The thrust can then be derived via the change of momentum $\dot{q} = \dot{m} v^{\infty}$ giving

$$T = \rho A v^{\mathrm{i}} \cdot v^{\infty}. \tag{2.9}$$

The momentum is hereby denoted by q in order to avoid confusion with pressure p. Another way of expressing thrust is via the difference in air pressure above (p_U) and below (p_L) the rotor disk

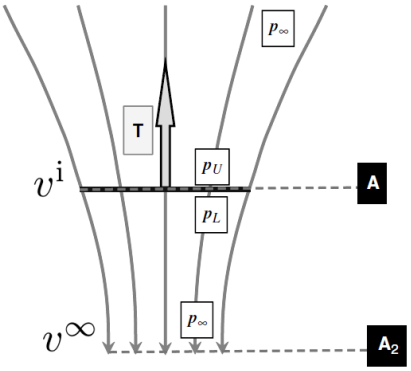

Figure 2.11: Streamtube of the airflow around a rotor in hovering flight [modified from 39, p. 24]

$$T = A(p_{\mathrm{L}} - p_{\mathrm{U}}). \tag{2.10}$$

To derive p_{L} and p_{U} Bernoulli's equation is applied, stating that the energy per unit volume before equals the energy after. Above the rotor this gives

$$p_\infty = p_{\mathrm{U}} + \frac{1}{2}\,\rho\left(v^{\mathrm{i}}\right)^2 \tag{2.11}$$

where $\left(\frac{1}{2}\rho\left(v^{\mathrm{i}}\right)^2\right)$ expresses the kinetic energy density of the fluid just above the rotor disk and p_∞ is the pressure far up- and downstream.

Below the rotor we get

$$p_{\mathrm{L}} + \frac{1}{2}\,\rho\left(v^{\mathrm{i}}\right)^2 = p_\infty + \frac{1}{2}\,\rho\left(v^{\infty}\right)^2. \tag{2.12}$$

Combining equations (2.11) and (2.12) results in

$$p_{\mathrm{L}} - p_{\mathrm{U}} = \frac{1}{2}\rho\left(v^{\infty}\right)^2. \tag{2.13}$$

Inserting this into equation (2.10) and substituting T from (2.9) yields

$$v^{\infty} = 2v^{\mathrm{i}}. \tag{2.14}$$

An expression for thrust is now found by inserting (2.14) into (2.9) yielding

$$\boxed{T = 2\rho A\left(v^{\mathrm{i}}\right)^2.} \tag{2.15}$$

The induced power of thrust is therefore

$$P_{\mathrm{T}} = T \cdot v^{\mathrm{i}} = 2\rho A\left(v^{\mathrm{i}}\right)^3. \tag{2.16}$$

Axial Flight [14]

For a rotor in axial flight a very similar discussion can be applied. Figure 2.12 shows the streamtube for this case including its velocities and streamtube area at the rotor disk as well as upstream and downstream. The thrust is still given by T.

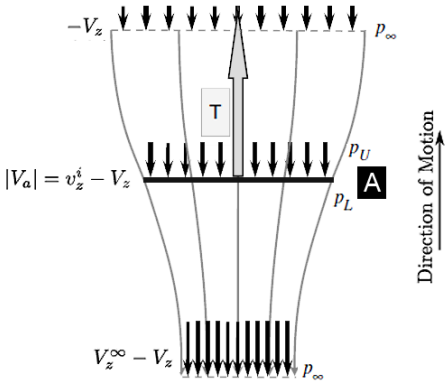

Figure 2.12: Streamtube of the airflow around a rotor in axial flight [modified from 14, 39]

First we define the velocity $\vec{v^{\mathrm{s}}}$ of the rotor (i.e. the velocity far upstream) as well as the total velocity $\vec{v^{\mathrm{a}}}$ of the air at the rotor disk by

$$\vec{v^{\mathrm{s}}} = \begin{pmatrix} 0 \\ 0 \\ v_z \end{pmatrix}, \; \vec{v^{\mathrm{a}}} = \begin{pmatrix} 0 \\ 0 \\ v_{\mathrm{z}}^{\mathrm{i}} - v_{\mathrm{z}} \end{pmatrix} \tag{2.17}$$

where $v_{\mathrm{z}}^{\mathrm{i}}$ is the induced velocity.

The mass flow rate is now given by

$$\dot{m} = \rho A |v^{\mathrm{a}}| \tag{2.18}$$

and the thrust force due to the change of momentum is given by

$$T = \underbrace{\dot{m}\left(v_{\mathrm{z}}^{\infty} - v_{\mathrm{z}}\right)}_{\text{momentum flux out}} - \underbrace{\dot{m}\left(-v_{\mathrm{z}}\right)}_{\text{momentum flux in}} = \dot{m} v_{\mathrm{z}}^{\infty} \tag{2.19}$$

yielding

$$T = \rho A |v^{\mathrm{a}}| \cdot v_{\mathrm{z}}^{\infty} = \rho A \left(v_{\mathrm{z}}^{\mathrm{i}} - v_{\mathrm{z}}\right) v_{\mathrm{z}}^{\infty} \tag{2.20}$$

Again, thrust can also be described by equation (2.10) and applying Bernoulli's equation gives

$$p_\infty + \frac{1}{2}\rho v_{\mathrm{z}}^2 = p_{\mathrm{U}} + \frac{1}{2}\rho \left(v_{\mathrm{z}}^{\mathrm{i}} - v_{\mathrm{z}}\right)^2 \tag{2.21}$$

above the rotor and

$$p_{\mathrm{L}} + \frac{1}{2}\rho \left(v_{\mathrm{z}}^{\mathrm{i}} - v_{\mathrm{z}}\right)^2 = p_\infty + \frac{1}{2}\rho \left(v_{\mathrm{z}}^{\infty} - v_{\mathrm{z}}\right)^2 \tag{2.22}$$

below. Combining (2.22) and (2.21) yields

$$p_{\mathrm{L}} - p_{\mathrm{U}} = \frac{1}{2}\rho \left(2v_{\mathrm{z}} + v_{\mathrm{z}}^{\infty}\right) v_{\mathrm{z}}^{\infty} \tag{2.23}$$

Inserting (2.23) into (2.10) and using (2.18) gives

$$v_{\mathrm{z}}^{\infty} = 2v_{\mathrm{z}}^{\mathrm{i}} \tag{2.24}$$

Substituting this into equation (2.20) results in the following expression for thrust

$$\boxed{T = 2\rho A|v^{\mathrm{a}}|v_{\mathrm{z}}^{\mathrm{i}} = 2\rho A\left(v_{\mathrm{z}}^{\mathrm{i}} - v_{\mathrm{z}}\right)v_{\mathrm{z}}^{\mathrm{i}}} \tag{2.25}$$

and the power is

$$P_{\mathrm{T}} = T\left(v_{\mathrm{z}}^{\mathrm{i}} - v_{\mathrm{z}}\right) = 2\rho A\left(v_{\mathrm{z}}^{\mathrm{i}} - v_{\mathrm{z}}\right)^2 v_{\mathrm{z}}^{\mathrm{i}} \tag{2.26}$$

Generalised Motion [14]

Figure 2.13 shows the streamtube for a rotor in general, non-axial motion. T denotes the thrust force while H is a horizontal force (perpendicular to T) occuring due to the horizontal motion of the rotor. The relative air velocity upstream is defined by

$$\vec{v^{\mathrm{s}}} = \begin{pmatrix} v_{\mathrm{x}} \\ v_{\mathrm{y}} \\ -v_{\mathrm{z}} \end{pmatrix}. \tag{2.27}$$

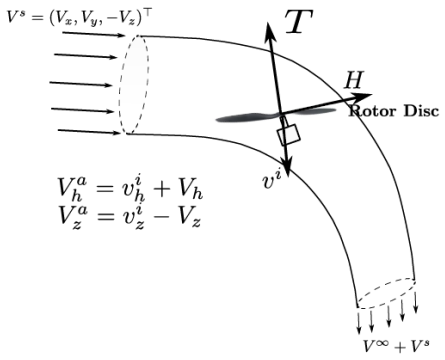

Figure 2.13: Streamtube of the airflow around a rotor in general flight [14, p. 6]

Both the air velocity at the rotor disk $\vec{v^{\mathrm{a}}}$ and the induced velocity $\vec{v^{\mathrm{i}}}$ now have components in all three directions and are in this discussion separated into a horizontal (subscript h) and vertical (subscript z) part

$$\vec{v^{\mathrm{a}}} = \begin{pmatrix} v_{\mathrm{h}}^{\mathrm{a}} \\ v_{\mathrm{z}}^{\mathrm{a}} \end{pmatrix} = \begin{pmatrix} v_{\mathrm{h}}^{\mathrm{i}} + v_{\mathrm{h}} \\ v_{\mathrm{z}}^{\mathrm{i}} - v_{\mathrm{z}} \end{pmatrix}. \tag{2.28}$$

The mass flow rate is still given by equation (2.18) and the force $\vec{F}$ exerted by the rotor derived from momentum conservation is

$$\vec{F} = \dot{m}\left(v^{\infty} + v^{\mathrm{s}}\right) - \dot{m}\left(v^{\mathrm{s}}\right) = \dot{m}v^{\infty} \tag{2.29}$$

where

$$\vec{T} = \begin{pmatrix} 0 \\ 0 \\ T \end{pmatrix}, \qquad \vec{H} = \begin{pmatrix} H_{\mathrm{x}} \\ H_{\mathrm{y}} \\ 0 \end{pmatrix}, \qquad \vec{F} = \vec{T} + \vec{H} = \begin{pmatrix} H_{\mathrm{x}} \\ H_{\mathrm{y}} \\ T \end{pmatrix} \tag{2.30}$$

The power from the rotor is given by

$$P = \vec{F}^{\mathrm{T}} v^{\mathrm{a}} = P_{\mathrm{T}} + P_{\mathrm{H}} \quad , \quad \begin{matrix} P_{\mathrm{T}} = T\left(v_{\mathrm{z}}^{\mathrm{i}} - v_{\mathrm{z}}\right) \\ P_{\mathrm{H}} = H\left(v_{\mathrm{h}}^{\mathrm{i}} + v_{\mathrm{h}}\right) \end{matrix} \tag{2.31}$$

Thrust force T
To find an expression for the thrust force, only the axial direction is considered. Equations (2.29) and (2.31) can thus be written as

$$T = \dot{m}\left(v_{\mathrm{z}}^{\infty} + (-v_{\mathrm{z}})\right) - \dot{m}\left(-v_{\mathrm{z}}\right) = \dot{m} v_{\mathrm{z}}^{\infty} \tag{2.32}$$

$$P_{\mathrm{T}} = T\left(v_{\mathrm{z}}^{\mathrm{i}} - v_{\mathrm{z}}\right) \tag{2.33}$$

The power P_{T} exerted by the rotor in the axial direction can also be found by the rate of kinetic power given by

$$P_{\mathrm{T}} = \underbrace{\frac{1}{2}\dot{m}\left(v_{\mathrm{z}}^{\infty} - v_{\mathrm{z}}\right)^2}_{\text{below rotor}} - \underbrace{\frac{1}{2}\dot{m}\left(-v_{\mathrm{z}}\right)^2}_{\text{above rotor}}. \tag{2.34}$$

Setting (2.34) equal to (2.33) and inserting (2.32) for T yields

$$v_{\mathrm{z}}^{\infty} = 2v_{\mathrm{z}}^{\mathrm{i}}. \tag{2.35}$$

Inserting this into (2.32) gives

$$\boxed{T = 2\rho A |\vec{v^{\mathrm{a}}}| v_{\mathrm{z}}^{\mathrm{i}}} \tag{2.36}$$

Horizontal force H
The derivation for the horizontal force is analogue to the thrust force. Using the conservation of momentum (2.29) and (2.31) can now be written as

$$H = \dot{m}\left(v_{\mathrm{h}}^{\infty} - v_{\mathrm{h}}\right) - \dot{m}\left(v_{\mathrm{h}}\right) = \dot{m} v_{\mathrm{h}}^{\infty} \tag{2.37}$$

$$P_{\mathrm{H}} = H\left(v_{\mathrm{h}}^{\mathrm{i}} - v_{\mathrm{h}}\right) \tag{2.38}$$

The rate of kinetic power gives

$$P_{\mathrm{H}} = \frac{1}{2}\dot{m}\left(-2v_{\mathrm{h}} v_{\mathrm{h}}^{\infty} + v_{\mathrm{h}}^{\infty}\right)^2 \tag{2.39}$$

Setting (2.39) equal to (2.38) and inserting (2.37) for H yields

$$\boxed{H = 2\rho A |\vec{v^{\mathrm{a}}}| v_{\mathrm{h}}^{\mathrm{i}}} \tag{2.40}$$

and for the power

$$P_{\mathrm{H}} = H\left(v_{\mathrm{h}}^{\mathrm{i}} + v_{\mathrm{h}}\right) \tag{2.41}$$

2.3.3 Blade Element Theory

With momentum theory alone the behaviour of a rotor in air can not be described fully. Blade Element Theory (BET) provides a different approach which can be used to close the system of equations. This theory looks at a small section of the rotor blade which can be described as an airfoil exposed to airflow. Thus lift and drag forces can be derived for the blade section. By then integrating over the whole blade length and over one revolution of the rotor, equations for thrust T, horizontal force H, torque τ and power P can be derived. As opposed to momentum theory, BET can account for varying incidence angles of the airflow due to the constantly changing azimuthal angle (angle of rotation of the rotor), different pitch angles for different types of propellers as well as an effect called blade flapping. The latter describes the tilting of the rotor plane due to the different relative velocities seen by the blades on opposing sides since one is advancing relative to the wind while the other is retreating. Another effect that can be accounted for in BET is tip losses. At the tip of the rotor blades the air is formed into vortices the size of which depends on the shape of the rotor blade. These vortices reduce the lift produced at the tips. This can be accounted for using a tip loss factor (typically around 0.97) which multiplied by the blade length provides the upper limit for the integration along the length of the blade.

2.4 Aviation Theory

In this section some basic principles of aviation will be outlined.

2.4.1 Reference Frames

For a multirotor, as for any aircraft, different reference frames can be applied. Here we consider them as they are usually defined in aerospace. [15]

The **inertial frame of reference (IRF)** is a coordinate system fixed on the ground. The x-axis points north, the y-axis east and the z-axis is directed downwards. The origin can be defined at a convenient location, e.g. take off point.

The **vehicle frame (VF)** is almost identical to the inertial frame. The only difference being the point of origin which here is placed in the centre of gravity of the vehicle.

The **body fixed frame (BFF)** is fixed to the body of the vehicle (see figure 2.14). Again its origin lies within the centre of gravity. The x-axis points out the front of the vehicle. The y-axis points out to the right and the z-axis

points out of the underside of the vehicle. To transform from the VF to the BFF a rotation has to be applied. This is given by the rotation matrix [15, p. 27]

$$R_v^b(\phi,\theta,\psi) = \begin{pmatrix} c_\theta c_\phi & c_\theta s_\psi & -s_\theta \\ s_\phi s_\theta c_\psi - c_\phi s_\psi & s_\phi s_\theta s_\psi + c_\phi c_\psi & s_\phi c_\theta \\ c_\phi s_\theta c_\psi + s_\phi s_\psi & c_\phi s_\theta s_\psi - s_\phi c_\psi & c_\phi c_\theta \end{pmatrix} \tag{2.42}$$

where $c_\alpha = \cos\alpha$, $s_\alpha = \sin\alpha$ and ϕ, θ and ψ are the roll, pitch and yaw angles.

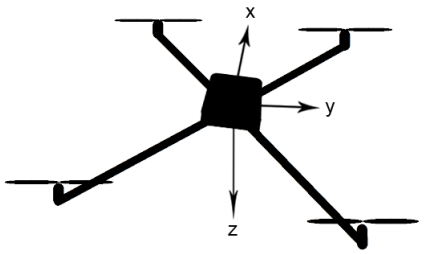

Figure 2.14: A quadrotor with its body fixed reference frame.

2.4.2 The Wind Triangle

For any vehicle moving in aerospace, three velocity vectors need to be distinguished:

- The **ground velocity** $\vec{v_g}$ is the velocity of the vehicle relative to the inertial frame of reference. It is important to note here that this ground velocity is a three dimensional vector. The ground speed which is saved to the logfile of the IRIS$^+$ drone, however, is the velocity of the drone projected onto the ground, i.e. the 2D horizontal ground velocity of the drone.
- The **wind velocity** $\vec{v_w}$ is the velocity at which the air moves relative to the ground.
- The **air velocity** $\vec{v_a}$ is the velocity of the vehicle relative to the surrounding air.

These three velocities are connected via

$$\vec{v_a} = \vec{v_g} - \vec{v_w}. \tag{2.43}$$

which is visualised in figure 2.15.

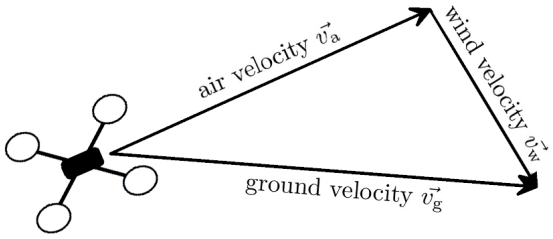

Figure 2.15: Wind triangle defined by the ground velocity $\vec{v_g}$, the wind velocity $\vec{v_w}$ and the air velocity $\vec{v_a}$

Chapter 3

Literature Review

The problem of wind estimation is a well researched one and several researchers have explored the idea of using drones for this. Some use fixed wing UAVs (e.g. [33], [18], [34]) and some explore the possibilities of mounting an anemometer onto a multirotor drone (e.g. [43], [35]). Of interest for this thesis, however, are mainly those who focused on estimating the local wind vector from the internal sensors of a quadrotor. This chapter gives a summary of research done on this.

When the idea for this thesis was conceived by Boström in 2015 there was very little to be found on the topic. However, as shown in this chapter, other researchers have since published related work.

3.1 Relating Thrust, Drag and Gravitational Forces

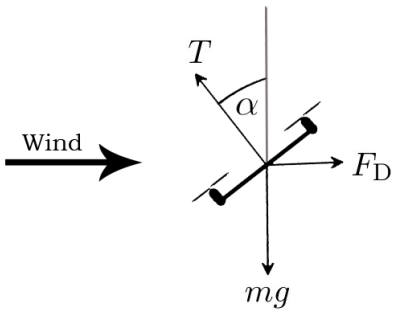

Figure 3.1: Forces acting upon a quadrotor exposed to horizontal wind.

Figure 3.1 shows a sketch of a quadrotor exposed to horizontal wind and the three force vectors acting on the drone. The thrust force acts perpendicular

to the plane of the drone which is inclined to the vertical by the inclination angle α. The gravity force $F_G = mg$ acts downwards. The magnitude of the drag force F_D is given by Rayleigh's drag equation

$$F_D = \frac{1}{2}\rho A c_D v_w^2 \tag{3.1}$$

where ρ is the air density, A the projected surface area of the drone which is exposed to the wind, c_D denotes the drag coefficient and v_w is the wind speed. The direction of the drag force is equal to the wind direction.
In stable flight without acceleration the three forces will equal to zero therefore giving

$$T\cos\alpha = F_G = mg, \tag{3.2}$$

$$T\sin\alpha = F_D. \tag{3.3}$$

Combining those two equations results in the following relation between the drag force and the inclination angle

$$F_D = m \cdot g \cdot \tan\alpha. \tag{3.4}$$

By combining this with equation (3.1) one can find the wind speed given that α, A, ρ and c_D are known.
It is important to note that this relation only holds due to the perpendicular nature of the gravity force and the drag force. For non-horizontal wind this relation will not be accurate.

3.1.1 Neumann and Bartholmai - 2015

Neumann and Bartholomai [32] were the first to pursue this method. They argued that the cross section A is relatively easy to find, however, finding the drag coefficient c_D for a quadrotor is tricky since the influence of the rotating propellers cannot easily be determined from standard tests. Neumann and Bartholmai therefore used wind tunnel experiments to correlate the roll and pitch angles of the drone to the wind speed. Again, this was only done for horizontal wind. After the development of a correlation function, flight tests were conducted to validate the method. Those were conducted with an ultrasonic anemometer mounted ca. 2 m above ground and the drone hovering close to it or following a quadratic path around the anemometer. The wind estimations from the quadrotor have a good correlation with the data from the anemometer. Calculated root mean square errors (RMSEs) are ± 0.60 m/s for the wind speed and $\pm 14.77°$ for the wind direction.

One important finding stems from their testing of different radial orientations of the quadrotor in the wind tunnel. The results showed that this does have an effect on the inclination angle but that it is negligible.

3.1.2 Palomaki et. al. - 2017

Palomaki et. al. [35] applied the same idea but refrained from using a wind tunnel. They combined equations (3.1) and (3.4) to

$$v_{\mathrm{w}}^2 = \hat{c} \tan \alpha \tag{3.5}$$

where the coefficient $\hat{c}$ includes m, g, ρ and A. This coefficient was then empirically determined by flying the quadrotor in hover between three pillar-mounted 2D sonic anemometers at a height of 10 m above ground. Here the calculated RMSE from four test flights lie between 0.3 and 0.9 m/s for the wind speed and between 10° and 21° for the wind direction.

Both of these papers determine the wind direction with a geometrical calculation from the tilt direction of the drone.

3.2 Other Approaches With a Quadrotor

The three papers presented below, apply three different approaches of estimating wind velocities with the use of a quadrotor. The key ideas are respectively the use of differential thrust, aircraft motion models and mounting an anemometer to the quadrotor. All three works limit their research to 2D wind.

3.2.1 Marino et. al. - 2015

Marino et. al. [28] present an evaluation of a quadrotor drone as a "Flying Wind Sensor". Their work is aimed at defining optimal sites for wind-turbine placements while their method is based on the understanding that a unique relationship between the thrust from each of the four motors and the flight condition exists. To find this relation, experiments in a wind tunnel were conducted varying the flow speed and incidence angle (by tilting the quadrotor towards the wind) while measuring the power consumption of all four rotors. Differential power between the rotors can thus be utilised to find the wind direction. A bijection between two 2D planes is needed, the first plane containing power and differential power whereas the second contains wind speed and wind direction. From the wind tunnel data it was found that such a unique bijection only is possible for low wind speeds of $v_{\mathrm{w}} <\sim$ 1.4 m/s and low incidence angles $\phi <\sim 5°$. This limits the applicability of the proposed method which according to the paper's conclusion could be improved using other multicopter configurations.

3.2.2 Gonzalez-Rocha et. al. - 2017

Gonzalez-Rocha et. al. [22] based their wind-velocity estimation on aircraft motion models. Equations of motion for a Kinematic Particle model, a Dynamic Particle model and a Dynamic Body model are derived. Wind tunnel tests were conducted with various flow speeds, incidence angles and propeller speeds while measuring three components of both aerodynamic force and torque. From those measurements a linear relation between the thrust coefficient c_T and the advance ratio J is found. The latter is defined by

$$J = \frac{v_\mathrm{wt}\,\sin(\alpha)}{\omega\, l}, \tag{3.6}$$

where v_wt is the wind tunnel flow speed, α the incidence angle (= tilt angle of the drone from the vertical when wind is horizontal), ω the propeller speed and l the propeller disk diameter. Therefore, if the advance ratio J is known, one can obtain the thrust coefficient c_T and further also the total quadrotor thrust T via

$$T = c_\mathrm{T}\,\rho\,\omega^2\,l^4. \tag{3.7}$$

From flight experiments the pitch and roll angles of the drone as well as horizontal drag parameters were related to the drone's heading angle β (i.e. yaw relative to the wind direction) and horizontal speed via the azimuthal model seen in figure 3.2.

To obtain a wind estimate with help of the kinematic particle model, the pitch and roll angles from the pixhawk data log are used together with this azimuthal model to obtain the vehicle's air velocity v_a. The wind velocity v_w is then found by subtracting v_a from the vehicle's ground velocity v_g.

When using the dynamic particle model, the measured pitch and roll angles were related to the vehicle's lateral thrust $f_\mathrm{x} = T\,\sin(\alpha)$. First v_wt was found using the azimuthal model and inserted into equation (3.6) to find the advance ratio. By using the experimentally determined correlation between J and c_T as well as equation (3.7) the total thrust T can then be found and thus lateral thrust f_x determined. A state observer was further used to estimate the vehicle's air velocity v_a from that. The wind velocity was then found via $v_\mathrm{w} = v_\mathrm{g} - v_\mathrm{a}$.

The accuracy of wind estimates from this method is limited by the accuracy of the motion models. The estimates are able to follow the trend of the wind but with low accuracy especially in fast varying wind conditions. An improvement of the method could be achieved by implementing the more complex dynamic body model.

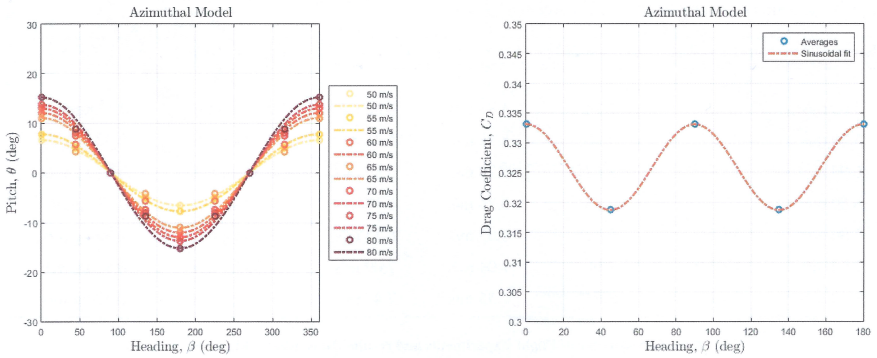

(a) Equilibrium tilt angles ϕ_{eq} and θ_{eq} as a function of β.

(b) Drag coefficient, C_D, as a function of β.

Figure 3.2: Azimuthal model from Gonzalez-Rocha [22]

3.2.3 Wolf et. al. - 2017

Wolf et. al. [43] focus on acquiring wind data with a quadrotor aiming to replace weather balloons in measuring atmospheric data. First a method involving the use of anemometers mounted on the quadrotor is investigated. From a static flow test a low-interference zone is found which is optimal for placing the sensor. At a distance of at least 0.7 m from the center of gravity, the influence of the rotor induced airflow on wind measurements is found to be minimal. Furthermore, the paper investigates the correlation of roll and pitch angles of the quadrotor with wind speed and direction. Tests were done with the quadrotor in a hovering position while applying horizontal wind at different speeds and from varying directions using a fan. However, no actual measurement technique based on this is proposed yet.

3.3 Quadrotor Control

The following two papers focus their research on improving the quadrotor's control algorithm. In order to achieve this, an estimate of the quadrotor's air velocity is made.

3.3.1 Waslander and Wang - 2009

Waslander and Wang [42] propose a wind estimator for quadrotor position control based on accelerometer data. A dynamic model of the vehicle's motion is developed that relates all forces and moments that act on the vehicle in still air to state parameters like position, velocity and acceleration that

are measured in-flight. Since this is assumed to be a complete description, any deviations in the accelerometer data from the expected values based on the dynamic model must be attributed to the wind. Thus a wind estimate can be found from accelerometer data. Additionally a prediction of the wind velocity is proposed based on models for static wind and wind gusts. From simulations the authors find their method to be promising although further testing and development is needed.

3.3.2 Allibert et. al. - 2014

Allibert et. al. [6] propose a method of estimating the air velocity of a quadrotor in the body-fixed frame by designing an observer based on both aerodynamic theory and accelerometer data. The velocity estimate can then be used for controlling the vehicle.

The linear dynamics of a quadrotor in the air can be expressed in the BFF as [6]

$$\dot{\vec{v_{\mathrm{a}}}} = -\Omega \times \vec{v} + gR^T \hat{e_{\mathrm{z}}} - \frac{1}{m} T \hat{e_{\mathrm{z}}} - \frac{1}{m} \vec{H} \tag{3.8}$$

where v_{a} is the drone's air velocity, Ω its angular velocity, m its mass, $R = R_v^b$ the transformation matrix from the inertial frame to the BFF, T is the Thrust and $\vec{H}$ the horizontal drag force from the rotors. The Inertial Measurement Unit (IMU) measures the specific acceleration $\vec{a}$ which is given by

$$\vec{a} = -\frac{1}{m} T \hat{e_{\mathrm{z}}} - \frac{1}{m} \vec{H}. \tag{3.9}$$

If the quadrotor is moving slowly, the vertical component of the drag force is negligible and

$$\vec{H} = \begin{pmatrix} H_{\mathrm{x}} \\ H_{\mathrm{y}} \\ 0 \end{pmatrix}$$

Therefore the acceleration can be used as a measure for T and H and one can write

$$\boxed{-m\vec{a} = \begin{pmatrix} H_{\mathrm{x}} \\ H_{\mathrm{y}} \\ T \end{pmatrix}} \tag{3.10}$$

To provide a correlation between T, $\vec{H}$ and aerodynamic power P_{a}, momentum theory is applied. For a single rotor this yields

$$T = 2\rho A v_{\mathrm{z}}^{\mathrm{i}} U \tag{3.11}$$

where ρ is air density, A the rotor disk area, $v_{\mathrm{z}}^{\mathrm{i}}$ the z-component of the induced velocity v^{i} and

$$U = |\vec{v^{\mathrm{i}}} - \vec{v_{\mathrm{a}}}| \tag{3.12}$$

with v_{a} being the vehicle's air velocity and $|\cdot|$ denoting the absolute value. The total thrust of all four rotors is then given by

$$\boxed{T = c_1 v_{\mathrm{z}}^{\mathrm{i}} U} \tag{3.13}$$

where $c_1 = 8\rho A$. As often done in momentum theory, only the vertical component of the induced velocity is considered, thus

$$\vec{v^{\mathrm{i}}} = \begin{pmatrix} 0 \\ 0 \\ v_{\mathrm{z}}^{\mathrm{i}} \end{pmatrix}. \tag{3.14}$$

For the horizontal drag force $\vec{H}$ a lumped model is used, based on the work in [12]

$$\boxed{\vec{H} = -TK_{\mathrm{r}}\vec{v_{\mathrm{a}}}}, \qquad K_{\mathrm{r}} = \begin{pmatrix} \bar{c} & 0 & 0 \\ 0 & \bar{c} & 0 \\ 0 & 0 & 0 \end{pmatrix} \tag{3.15}$$

where $\bar{c} > 0$ is a lumped linear drag coefficient. Parasitic drag, which occurs due to the airframe, is neglected in this paper, since according to (2.6) it depends quadratically on v_{a} and the quadrotor is considered to be in near hover conditions (i.e. small v_{a}).

The thrust power and horizontal drag power are given by

$$P_{\mathrm{T}} = T\left(v_{\mathrm{z}}^{\mathrm{i}} - v_{\mathrm{z}}\right) \tag{3.16}$$

$$P_{\mathrm{H}} = -\vec{H}^{\mathrm{T}}\vec{v} \tag{3.17}$$

which can be connected via

$$P_{\mathrm{a}} = P_{\mathrm{T}} + P_{\mathrm{H}} \tag{3.18}$$

to describe the aerodynamic power P_{a} which is the power supplied to the airflow by the rotors.

The mechanical power applied to the rotor is given by

$$P_{\mathrm{m}} = \tau\omega \tag{3.19}$$

where τ is the torque through the rotor shaft and ω is the rotational speed of the rotor. It is related to the aerodynamic power according to [13]

$$P_{\mathrm{m}} = P_{\mathrm{a}} + P_{\mathrm{dissip}} + P_{\mathrm{r}}. \tag{3.20}$$

where P_{dissip} denotes the power that is dissipated in the process of generating aerodynamic power and P_{r} is the power needed to rotate the propeller. The latter is given by (3.21) where I is the moment of inertia of the rotor blade and $\dot{\omega}$ is its rotational acceleration. The dissipated power behaves according to (3.22) where FoM is the Figure of Merit. It is an efficiency factor given for the motor-propeller system in hover and stems from different effects like tip losses that reduce the efficiency of the rotors.

$$P_{\text{r}} = I\omega\dot{\omega} \tag{3.21}$$

$$P_{\text{dissip}} = P_{\text{a}}\frac{1 - FoM}{FoM} \tag{3.22}$$

Using (3.22), equation (3.20) can be rewritten to

$$\boxed{P_{\text{m}} = \frac{1}{FoM}P_{\text{a}} + P_{\text{r}}.} \tag{3.23}$$

This derivation results in a system of equations connecting the variables $v_{\text{a}} = (v_{\text{x}}, v_{\text{y}}, v_{\text{z}})$, v_{z}^{i}, $\vec{H}$ and T. By measuring accelerometer data, the system can be solved for the vehicle's air velocity v_{a} provided some parameters are determined first. The torque τ can be found by connecting the motor parameter K_{v} and the measured current i via $\tau = 1/K_{\text{v}} \cdot i$. The rotor acceleration $\dot{\omega}$ is found from the measured rotational velocity ω by applying a complementary filter as described in [13]. The FoM is determined from a static thrust test.

Allibert et. al. propose an observer that applies the derived equations to in-flight measurements. The resulting evaluation of the vehicle's attitude and velocity is then used to control the quadrotor. In order to test the observer, a simulation is run with the simulated quadrotor following a circular motion. The vertical velocity is thereby varying sinusoidally. The input values to the observer, since no actual measurements are conducted, are simulated by adding a random noise-signal to the known values. Figure 3.3 shows the result of this simulation. It is visible that the estimated velocities $\hat{V}$ (black) follow the true velocity V (yellow) quite well. $\bar{V}$ (blue) shows the velocity calculated algebraically from the accelerometer data without applying the observer. ϵ (red) denotes the difference between the estimated $\hat{V}$ and the true velocity V.

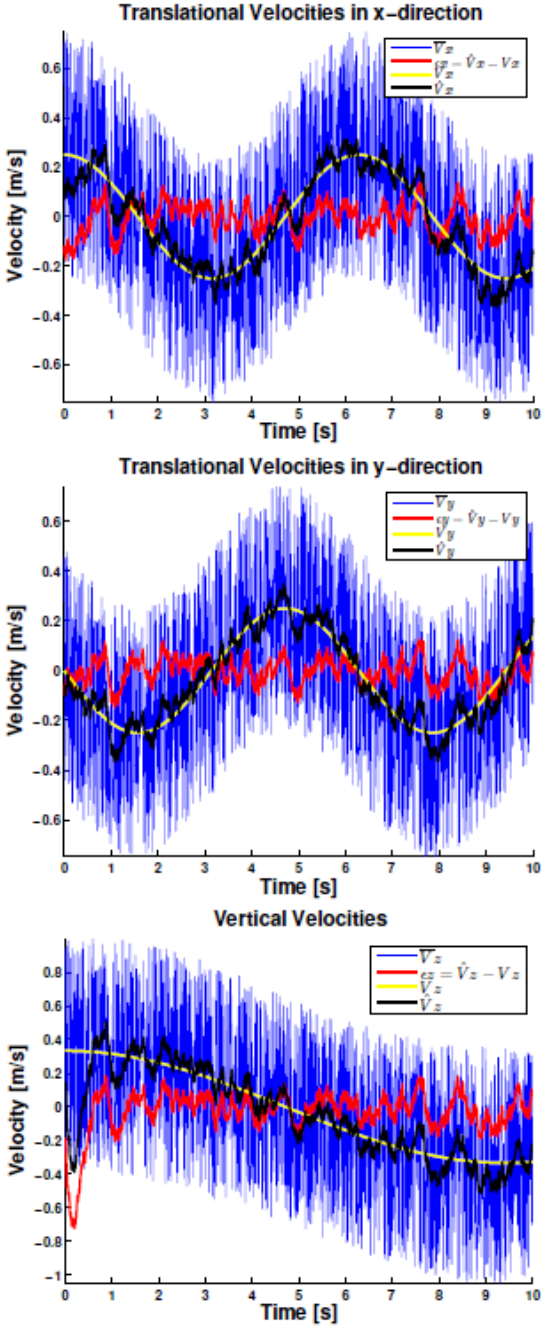

Figure 3.3: Results from Allibert [6]

Chapter 4

Method

This chapter presents the method used to estimate wind velocity from the measurements of the IRIS$^+$ quadrotor. The first section 4.1 summarises the theory underlying the proposed measurement method. Section 4.2 describes the static thrust tests, that were conducted. The gathering of data through test flights with the drone is explained in section 4.3 and section 4.4 focuses on how the collected data is analysed.

4.1 Methodological Theory

The works mentioned in chapter 3 on measuring wind with a quadrotor drone focus on measuring 2D wind. This thesis, however, aims for measuring 3D wind. The method therefore uses a fundamentally different approach to those presented in the literature [6, 22, 32]. The theoretical framework uses the theoretical equations presented by Allibert et. al. [6] which provide a means of calculating the quadrotor's air velocity in the BFF. By then transforming the air velocity to the IRF and further applying the wind triangle, an estimate for wind velocity can be achieved.

The following paragraphs summarise the assumptions and equations that form the theory. In addition, a discussion is given on how to solve the equations as well as which parameters and variables are needed to do so.

4.1.1 Assumptions

Two main assumptions underlie the equations providing the theoretical description of the method.

- Parasitic drag from the airframe is neglected since it is proportional to the squared air velocity. This is a reasonable assumption for quadrotors in near hover conditions [6]. Bangura and Mahony [12] state 10 m/s as the upper limit for this assumption.

- The aerodynamic conditions are assumed to be the same for all four rotors and an average rotor speed and average induced velocity are applied. This also includes the assumption of having the same flapping angles and drag forces for all four rotors. Again this is a reasonable assumption for a slowly moving quadrotor. [6]

4.1.2 Equations, Parameters and Variables

The equations used in this thesis to determine the drone's air velocity v_a in the BFF are based on [6]. They are defined in (4.1) to (4.10). Equation (4.1) stems from the linear dynamics of the quadrotor.Equations (4.2) to (4.7) are aerodynamic equations based on momentum theory while equations (4.9) and (4.10) are mechanical equations. Tables 4.1 and 4.2 list the parameters and variables needed in order to solve this set of equations for $\vec{v_\mathrm{a}}$.

$$\vec{a} = -\frac{1}{m}T\hat{e_\mathrm{z}} - \frac{1}{m}\vec{H} \quad (4.1)$$
$$\vec{H} = -T\bar{c}\left(v_x\hat{e_\mathrm{x}} + v_y\hat{e_\mathrm{y}}\right) \quad (4.2)$$
$$T = 8\rho A_\mathrm{tot} v_\mathrm{z}^\mathrm{i} U \quad (4.3)$$
$$U = |\vec{v^\mathrm{i}} - \vec{v_\mathrm{a}}| \quad (4.4)$$
$$P_\mathrm{a} = P_\mathrm{T} + P_\mathrm{H} \quad (4.5)$$
$$P_\mathrm{T} = T\left(v_\mathrm{z}^\mathrm{i} - v_\mathrm{z}\right) \quad (4.6)$$
$$P_\mathrm{H} = -\vec{H}^\mathrm{T}\vec{v} \quad (4.7)$$
$$P_\mathrm{m} = \frac{1}{FoM}P_\mathrm{a} + P_\mathrm{r} \quad (4.8)$$
$$P_\mathrm{m} = \tau\omega \quad (4.9)$$
$$P_\mathrm{r} = I\omega\dot{\omega} \quad (4.10)$$

Table 4.1: Parameters needed to solve the set of equations

Parameters		
m	$1.371\,\mathrm{kg}$	Mass of the drone
ρ	$1.268\,\mathrm{kg/m^3}$	Air density
A_tot	$0.1829\,\mathrm{m^2}$	Total rotor disk area
I	$6.55 \cdot 10^{-5}\,\mathrm{kg\,m^3}$	Propeller moment of inertia
$\bar{c}$	0.015	Lumped linear drag coeff.
FoM	0.6072	Figure of merit

Table 4.2: Variables needed to solve the set of equations

Variables needed		Unknown variables	
$\vec{a}$	Accelerometer data	$\vec{v}$	3D air velocity
ω	Rotational velocity of propeller	v_z^i	Vertical induced velocity
$\dot{\omega}$	Rotational accel. of propeller	$\vec{H}$	Horizontal drag force
τ	Motor torque	T	Vertical thrust

Some of the parameters given in table 4.1 are easily measured. The mass m of the drone is found by weighing the drone with propellers mounted and the battery in place. The air density used is the value for atmospheric pressure and a temperature of 5° C [20], which is a reasonable assumption for Tromsø. However, varying the air density by $\pm\,0.05\,\mathrm{kg/m^3}$, which corresponds to a change in temperature of $\pm\,10°\,\mathrm{C}$, hardly affects the results, and the error is thus negligible. The total rotor disk area is given by $A_{\mathrm{tot}} = 4 \cdot \left(\frac{l}{2}\right)^2$ where $l = 9.4" = 24.13\,\mathrm{cm}$ is the diameter, or total length of the propeller. For the calculation of the moment of inertia of the propeller, a simplifying assumption is made. The propeller is seen as a rod of length l rotating around its centre. The moment of inertia can thus be calculated using $I = \frac{1}{12}\, m_{\mathrm{prop}}\, l^2$ where $m_{\mathrm{prop}} = 13.5\,\mathrm{g}$ is the mass of the propeller.

The lumped linear drag coefficient $\bar{c}$ is found empirically from experiments, the details of which will be described further in section 6.1.

As mentioned in section 3.3.2, the Figure of Merit (FoM) is an efficiency factor given for the motor propeller system in hover. It relates the mechanical power P_{m} provided to the motor to the aerodynamic power P_{a} created by the rotation of the propeller according to equation (4.8). The FoM can be determined from a static thrust test (see section 4.2), where both P_{m} and P_{a} are measured. The slope of a linear fit to the data then gives the figure of merit.

As for the variables needed to solve the system of equations (table 4.2), the accelerometer data is the only one measured directly by the quadrotor and stored in the pixhawk log. Neither the propellers' rotational velocity or acceleration, nor the motor torque are directly measured. To find these, a relation between them and other, directly measured variables like the battery voltage and RCOU value need to be established. This is also done based on data acquired via a static thrust test and will be explained further in section 4.2.3.

4.1.3 Solving for the Air Velocity

Once all parameters and variables are determined, the set of equations defined in (4.1 - 4.10) can be solved for the unknown variables and the vehicle's air velocity $\vec{v_{\mathrm{a}}}$ can be found.

As $\vec{H}$ does not have a component in $\hat{e_{\mathrm{z}}}$, (4.1) yields

$$T = -\,m \cdot a_{\mathrm{z}}. \tag{4.11}$$

By further inserting (4.2) into (4.1), the horizontal air velocities

$$v_{\mathrm{x}} = +\frac{a_{\mathrm{x}}}{a_{\mathrm{z}}\bar{c}} \tag{4.12}$$

$$v_{\mathrm{y}} = +\frac{a_{\mathrm{y}}}{a_{\mathrm{z}}\bar{c}} \tag{4.13}$$

are found. (4.2) is then inserted into (4.7) to give

$$P_{\mathrm{H}} = T\bar{c}\left(v_{\mathrm{x}}^2 + v_{\mathrm{y}}^2\right) = \frac{-m}{a_{\mathrm{z}}\bar{c}}\left(a_{\mathrm{x}}^2 + a_{\mathrm{y}}^2\right). \tag{4.14}$$

Then P_{m} and P_{r} are calculated according to (4.9) and (4.10) respectively. By combining (4.5) with (4.8), P_{T} can be found via

$$P_{\mathrm{T}} = (P_{\mathrm{m}} - P_{\mathrm{r}})\, FoM - P_{\mathrm{H}}. \tag{4.15}$$

Rearranging (4.6) results in the following expression

$$\left(v_{\mathrm{z}}^{\mathrm{i}} - v_{\mathrm{z}}\right) = \frac{P_{\mathrm{T}}}{T}. \tag{4.16}$$

(4.4) can be rewritten as

$$U = |\vec{v^{\mathrm{i}}} - \vec{v}| = \sqrt{\left(v_{\mathrm{x}}^{\mathrm{i}} - v_{\mathrm{x}}\right)^2 + \left(v_{\mathrm{y}}^{\mathrm{i}} - v_{\mathrm{y}}\right)^2 + \left(v_{\mathrm{z}}^{\mathrm{i}} - v_{\mathrm{z}}\right)^2} \tag{4.17}$$

and since the induced velocity $\vec{v^{\mathrm{i}}}$ is assumed to only have a vertical component $v_{\mathrm{z}}^{\mathrm{i}}$, it follows that

$$U = \sqrt{v_{\mathrm{x}}^2 + v_{\mathrm{y}}^2 + \left(v_{\mathrm{z}}^{\mathrm{i}} - v_{\mathrm{z}}\right)^2}. \tag{4.18}$$

The induced velocity can then be calculated from (4.3) to be

$$\vec{v^{\mathrm{i}}} = v_z^{\mathrm{i}}\hat{e_{\mathrm{z}}} = \frac{T}{8\rho A_{\mathrm{tot}} U}\hat{e_{\mathrm{z}}} \tag{4.19}$$

and finally inserting back into (4.6) yields the vertical air velocity

$$v_{\mathrm{z}} = v_{\mathrm{z}}^{\mathrm{i}} - \frac{P_{\mathrm{T}}}{T}. \tag{4.20}$$

4.1.4 Finding the Local Wind Velocity

Two more steps are needed to determine the local wind velocity $\vec{v_{\mathrm{w}}}$ from the calculated air velocity of the quadrotor.

First, the air velocity has to be transformed to the vehicle frame via

$$\vec{v_{\mathrm{a}}^{\mathrm{VF}}} = \left[R_v^b\left(\phi, \theta, \psi\right)\right]^T \cdot \vec{v_{\mathrm{a}}} \tag{4.21}$$

where $R_v^b\left(\phi, \theta, \psi\right)$ is the transformation matrix defined in (2.42).

The last step is the application of the wind triangle. Rearranging equation (2.43) yields

$$\vec{v_{\mathrm{w}}} = \vec{v_{\mathrm{g}}} - \vec{v_{\mathrm{a}}^{\mathrm{VF}}} \tag{4.22}$$

with $\vec{v_{\mathrm{g}}}$ being the vehicle's ground velocity given in the inertial reference frame. Since the IRF and VF are identical apart from their point of origin, velocities from both reference frames can simply be used together. The quadrotor's ground velocity is another variable to be determined from the quadrotor's measurements which is further described in section 4.4.5.

4.2 Static Thrust Test

In a static thrust test, only one motor-propeller system is mounted onto a test rig. By powering the single motor while taking different measurements like thrust, voltage, current etc. valuable insights can be gained.

4.2.1 Simple Test Rig

As a first approach, a relatively simple test rig, as seen in figure 4.1, was used. The motor with propeller is mounted on the vertical arm of an L-shaped structure, which is free to rotate around an axis where the two arms connect. If the motor is turned on, the aerodynamic thrust force F_{T} created by the rotor causes a rotation of the L-shaped structure around its mounting. The horizontal arm thus presses down on a scale with the same force $F = F_{\mathrm{T}}$. The thrust force can therefore be measured by multiplying the output of the scale in kg with the Earth's gravitational acceleration $g = 9.81\ \mathrm{m/s^2}$.

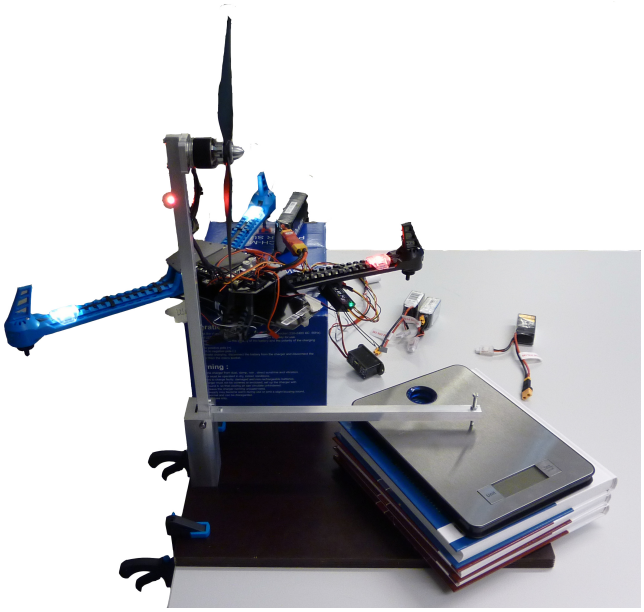

Figure 4.1: Simple static thrust test rig [Photo: Simma]

Since the mounting of a single motor onto the test rig calls for some dismantling of the quadrotor, it was decided to use an IRIS$^+$ drone with a broken arm as it wouldn't be ready for flight for a while. The clockwise rotating motor was disassembled from the broken back right arm, keeping the electrical connection to the ESC intact. Figure 4.2 shows the electrical components which were connected to the quadrotor in addition to the supply battery, their details are listed in table 4.3. As only one of the four motors was supposed to be operating, the pixhawk autopilot was not used. Instead, a telemetry link between a controller and the drone was set up with the X8R receiver from FrSKY. Thus, the RCOU signal could be adjusted via the controller and transmitted to the quadrotor through the telemetry link. The ESC then converted it into a motor signal. A current sensor was connected to the IRIS+ battery and an RPM sensor was connected to the output of the ESC. The measurements of both those sensors as well as an internal measure of battery voltage were transmitted to the controller via the telemetry link, where the data was stored in a telemetry log file.

The experiment was conducted by connecting a fully charged battery to the quadrotor-sensor system. Via the controller a certain RCOU value was chosen causing the motor to rotate accordingly. Scale measurements were noted manually every ten seconds until the battery was discharged to a critical voltage. The IRIS+ battery is designed to provide about ten minutes of flight time, thus discharging a full battery with only one active motor would take a while. For time efficiency reasons, a different battery with the same

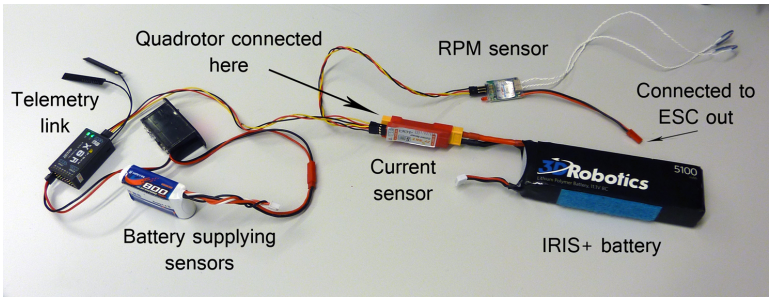

Figure 4.2: Electrical setup for simple static thrust test [Photo: Simma]

Table 4.3: Electrical components used in the static test rig

Component	Model	Manufacturer
Telemetry link	X8R 8/16 ch telemetry	FrSKY
RPM sensor	Smart Port RPM sensor	FrSKY
Current sensor	Smart Port Current sensor 40 A	FrSKY
Battery supplying sensors	LiPo 800 mAh	HAIYIN
IRIS$^+$ battery	LiPo 5000 mAh 11.1 V 8C	3DRobotics
Battery used for testing	LiPo 850 mAh 11.1 V 75C	TATTU

voltage but lower mAh-rating was therefore used. The same experiment was repeated with RCOU values ranging from 1450 - 1700 μs in intervals of 50 μs.

The measurements gained from this experiment are listed in table 4.4 compared to the setup described in the next subsection.

4.2.2 Dynamometer

Since the simple test rig didn't provide a measure for motor torque, a second static thrust test was conducted using the RCbenchmark series 1580 thrust stand and dynamometer. The measurements listed in table 4.4 are all measured by the device directly.

Table 4.4: Measurements taken by the static thrust tests

Measurements	Test Rig	Dynamometer
Thrust	✓	✓
Torque		✓
Battery voltage	✓	✓
Current drawn from battery	✓	✓
Rotational velocity of motor	✓	✓
RCOU values	✓	✓

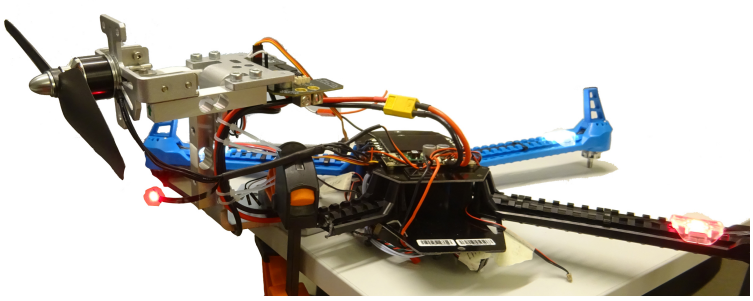

Figure 4.3: Static thrust test setup with the dynamometer [Photo: Simma]

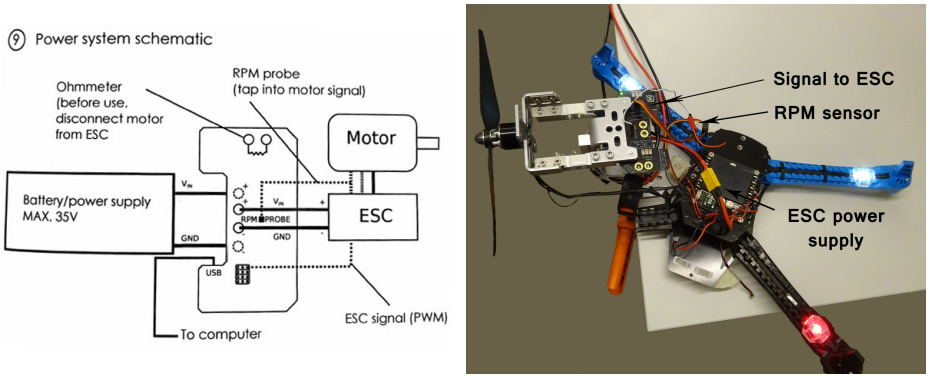

Figure 4.4: Left: Power schematic of the dynamometer [37], Right: Image of the cables connected [Photo: Simma]

Figure 4.3 shows the experimental setup using the dynamometer. After calibrating the thrust and torque measurements of the dynamometer as described in the manual [37], the device was fastened to the edge of a table using c-clamps. Then the motor and propeller were mounted onto the dynamometer and the electronics connected as shown in figure 4.4. As before, the drone with the broken arm was used for this test. The power to the dynamometer and ESC was provided by a switch mode power supply, where the output voltage can be adjusted manually between $5 - 15\,\mathrm{V}$ DC. The dynamometer is connected to a computer via USB. With the RCbenchmark software, the RCOU value can be controlled and all measurements stored in log files.

During the conduction of the static thrust test with the dynamometer, a certain voltage value was set on the power supply. Then a new log was started and the input values to the ESC (RCOU value) manually adjusted. RCOU values from $1400 - 1750\,\mu\mathrm{s}$ were used with increments of $50\,\mu\mathrm{s}$. For each setting of the RCOU value the motor was left to run for a few seconds to collect several data points before changing to the next higher RCOU

value. After having done this for the desired RCOU values, the voltage was adjusted, a new log started and the RCOU values run through again.

A total of 12 different voltage settings were tested. For two of those the RCOU range is between 1450 - 1700 µs, four have a range of 1400 - 1700 µs and the last 6 voltage measurements were conducted at the range of 1400 - 1750 µs. This gives a total of 88 different combinations of voltage and RCOU values that were tested.

4.2.3 Data Processing

Comparison of Datasets

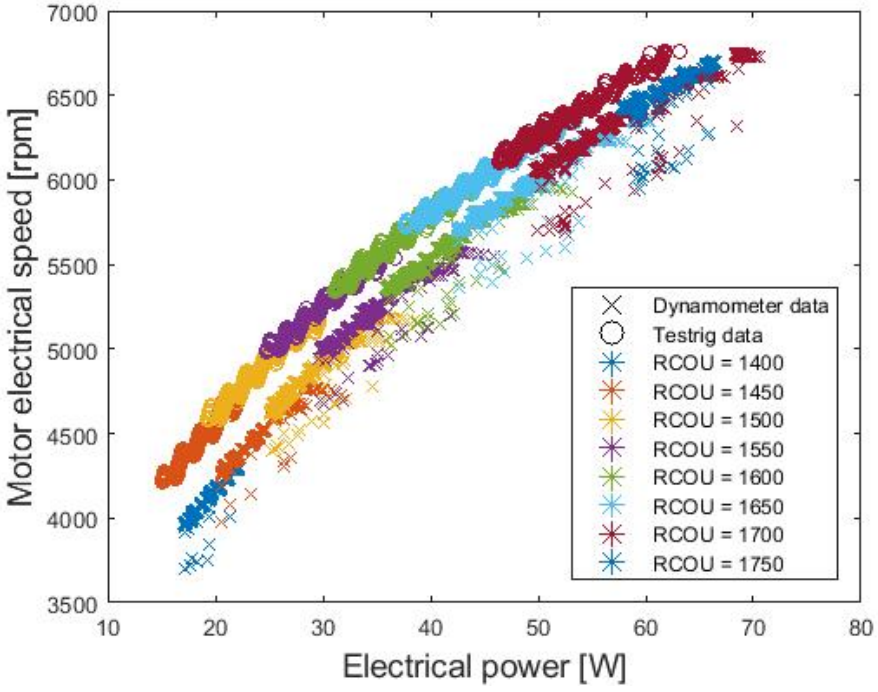

Figure 4.5: Comparison of dynamometer and test rig data. The dynamometer data is marked with x while the data from the test rig is indicated by circles. The different colours represent different RCOU values between 1400 and 1750 μs. The test rig data appears with an offset to the left towards lower electrical power at the same motor speed and RCOU value as the dynamometer data.

When comparing the data from the first test rig to the data acquired with the dynamometer, a considerable offset is found. Figure 4.5 exemplifies this offset in a plot of motor speed over electrical power. The dynamometer data is indicated with the symbol x while the test rig data is represented by

circles. The different colours represent different RCOU values. As can be seen, the curves have a similar trend, however, the test rig data seems to be offset towards lower electrical power values.

In a quick test, the motor was run with the dynamometer setup while simultaneously measuring the current with the FrSKY current sensor. This measurement showed about 0.5 A lower current values in the FrSKY current sensor compared to the dynamometer measurements. At a voltage of roughly 10 V this corresponds to a power offset of about 5 W which explains the offset seen in figure 4.5.

The dynamometer data is assumed to be more accurate, since all data was collected with one device. It could further be verified with the help of an amperemeter that the current value given by the dynamometer was the correct one. Thus, the data from the first test rig is considered faulty and only the dynamometer data is used in further analyses.

Figure Of Merit

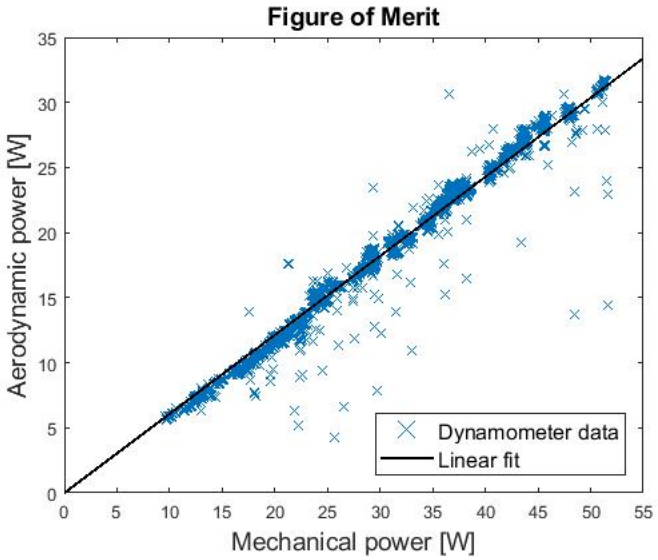

Figure 4.6: Plot of aerodynamic power over mechanical power. The slope of the linear fit is the FoM.

As explained in section 4.1.2, the FoM is found from a plot of aerodynamic power over mechanical power as seen in figure 4.6. Neither of these powers are directly measured, but they can easily be derived from the measurements taken in the static thrust test.

The mechanical power P_{m} is found by multiplying motor torque τ with the rotational speed ω of the propeller. Since the rotational speed is measured in rpm, attention has to be paid to the correctional factor in the following equation.

$$P_{\mathrm{m}} = \tau \cdot \omega = \tau \cdot \omega[rpm] \cdot \frac{2\pi}{60\,\mathrm{s}} \tag{4.23}$$

The aerodynamic power P_{a} is given by multiplying thrust T with the velocity of the air through the rotor area. Due to the experiment being static, this velocity is the induced velocity as it is described in momentum theory for a hovering vehicle. Equation (2.15) relates thrust to the induced velocity yielding

$$v_{\mathrm{i}} = \sqrt{\frac{T}{2\rho A}} \tag{4.24}$$

where ρ is air density and $A = (l^2/4) \cdot \pi$ is the rotor disk area with l being the rotor length. Thus the following equation for aerodynamic power can be derived

$$P_{\mathrm{a}} = T \cdot v_{\mathrm{i}} = \sqrt{\frac{T^3}{2\,\rho\,(l^2/4)\,\pi}} = \sqrt{\frac{2\,T^3}{\rho\,l^2\,\pi}} \quad . \tag{4.25}$$

The FoM can now be found from the slope of a linear fit through the datapoints. The fit shown in figure 4.6 is forced through the origin and the figure of merit is found to be $FoM = 0.6072$.

Rotational Velocity vs. Electrical Power

The rotational velocity of the propellers is not measured by the quadrotor in flight. However, it can be calculated if the electrical power of the motor is known. Figure 4.7 shows the rotational velocity measured in the static thrust test plotted over the electrical power which is the product of voltage and current measured by the dynamometer. A quadratic function given by equation (4.26) is fitted to the data providing the means to calculate the rotational velocity ω.

$$\omega[rpm] = -0.506 \cdot P_{\mathrm{el}}^2 + 96.673 \cdot P_{\mathrm{el}} + 2468.5 \tag{4.26}$$

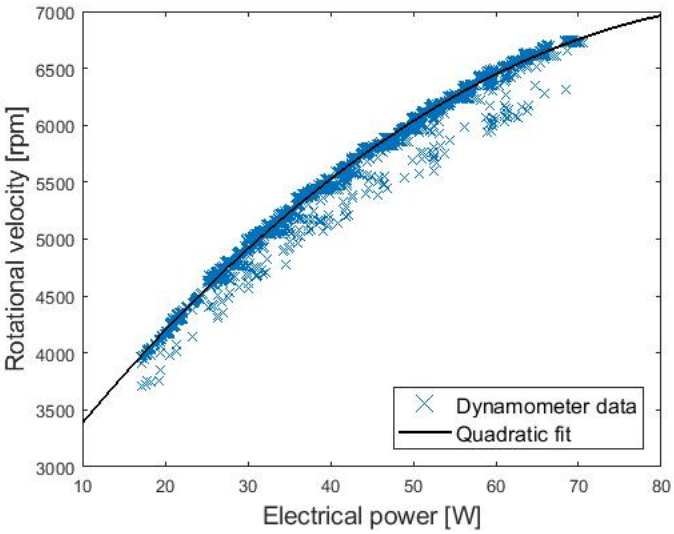

Figure 4.7: Rotational velocity over electrical power from static thrust test. A quadratic fit is laid to the measurements.

Torque vs. Electrical Power

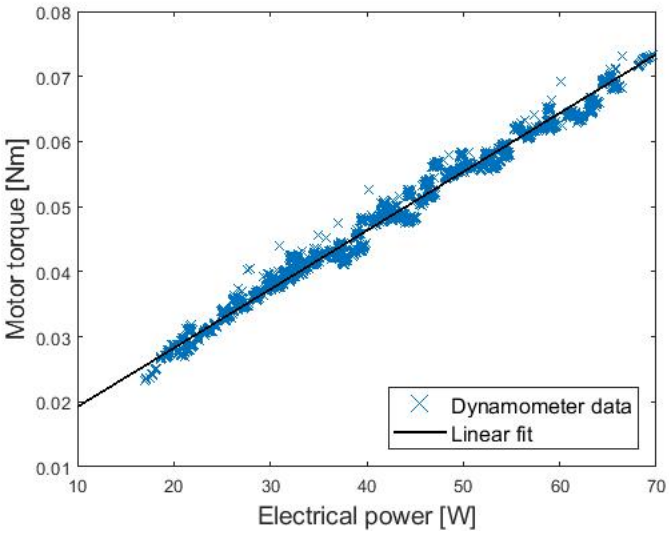

Figure 4.8: Torque over electrical power from static thrust test. A linear fit is laid to the data.

The torque τ of the motor on the rotor shaft can also be calculated from known electrical power. Figure 4.8 shows the torque measured by the dy-

namometer over the measured electrical power. The linear fit that is laid to the data is described by

$$\tau = 0.000903 \cdot P_{\text{el}}^2 + 0.0102 \tag{4.27}$$

In [6] Allibert et. al. propose to calculate the motor torque via $\tau = 1/K_{\text{v}} \cdot i$ where K_{v} is a motor constant and i is the current measured in flight. The motor constant of the IRIS$^+$ is known to be $K_{\text{v}} = 920\,\text{rpm/V}$. However, as can be seen in figure 4.9, this calculation results in too low torque values compared to those measured in the static thrust test. Thus equation (4.27), which is established from the static thrust test, is used in this thesis to calculate motor torque.

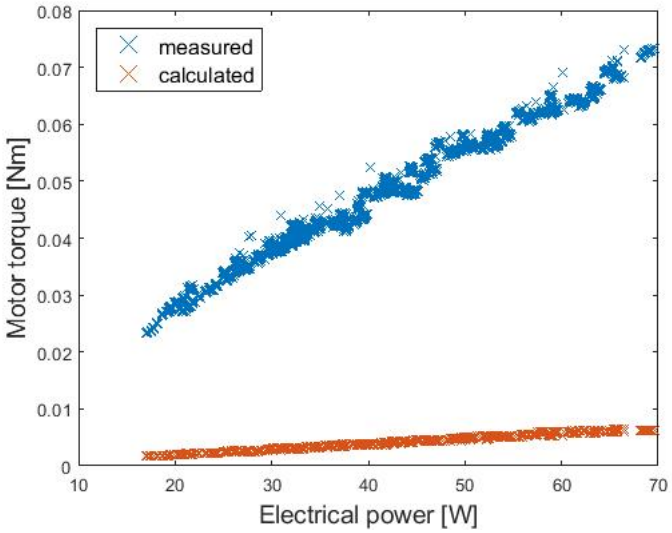

Figure 4.9: Comparison of measured torque and torque calculated from the motor constant K_{v}.

Current vs. Voltage and RCOU

Both the above calculations of rotational velocity and torque need a measure of electrical power and thus of voltage and current. The voltage measured both in flight and in the static thrust test is the battery voltage. The current measurement is a bit more problematic. The measurement taken both in flight and in the static thrust test is the current drawn from the battery. During the static tests, this can be considered equal to the current that drives one motor. In flight, however, the current drawn from the battery is feeding four motors plus the autopilot. The current measured in flight can therefore not be used for the proposed calculations.

To solve this problem, a mathematical description for the current of one motor is constructed. The battery voltage together with the RCOU signal form the basis of the model since they can be measured in flight. During the static thrust test, measurements of current have been made for eight different RCOU values and voltages between 10.7 - 12.2 V.

For each of the RCOU values, current is plotted over voltage. Then a linear curve is fit to the data points and its slope k and offset d noted. Figure 4.10 exemplifies this for the RCOU value of 1650 μs. Then all found k and d values are plotted over RCOU as seen in figure 4.11 and two more linear fits are created.

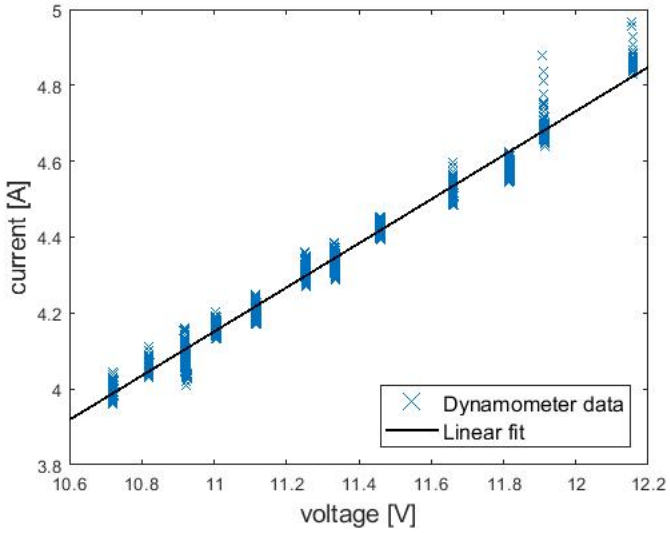

Figure 4.10: Current over voltage for RCOU = 1650 μs with a linear fit resulting in an inclination value $k = 0.581\,\mathrm{A/V}$ and an offset $d = -2.24\,\mathrm{A}$.

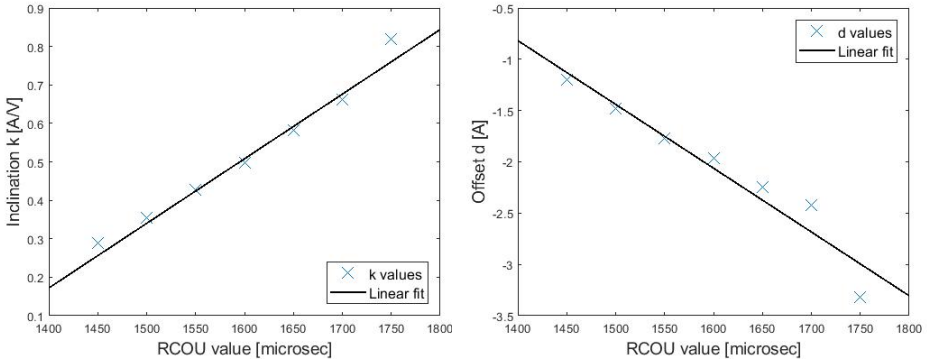

Figure 4.11: k and d values plotted over RCOU with a linear fit. RCOU values ranging from 1450 μs to 1750 μs.

When flying the quadrotor, measurements of RCOU and battery voltage V are taken. From the last two fits, a k and d value can be found for a given RCOU value. The corresponding current i_{calc} is then found via

$$i_{calc} = k \cdot V + d. \tag{4.28}$$

Figure 4.12 shows a comparison of the raw data measured by the dynamometer and current values calculated according to the described method. It can be seen that the calculated curves fit the data well for some RCOU values (e.g. RCOU = 1500 μs, 1700 μs) while its offset for others can be up to 0.5 A (RCOU = 1400 μs). The offsets also vary between being positive and negative. Reasons for this could be inaccurate current measurements by the dynamometer or a too simplistic approach of this linear model. Higher accuracy could be achieved by conducting further measurements with additional RCOU values.

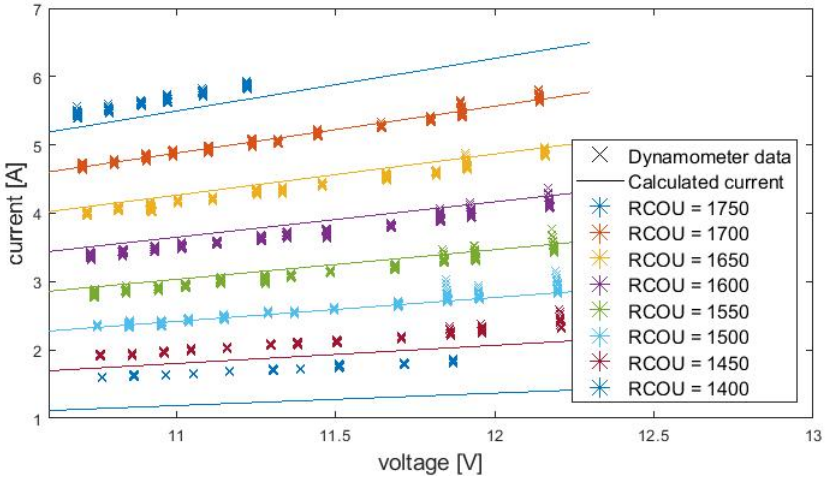

Figure 4.12: Comparison of measured current values and calculated ones based on the described model. The calculated current has offsets from the measured data of up to 0.5 A.

To improve the results of this model, it can also be limited to a smaller range of RCOU values. The observation justifying this, which will be described in section 4.4.5, is that the RCOU values of interest mainly lie between 1550 μs and 1650 μs. Figure 4.13 shows the k and d values plotted for the three RCOU values within that range with linear fits through the data points. The comparison of calculated and measured current values in figure 4.14 shows that this limited range improves the accuracy of the model. Thus the k and d values to use in equation (4.28) are found via (4.29) and (4.30).

$$k = \quad 0.0015 \cdot RCOU - 1.948 \tag{4.29}$$
$$d = -0.0047 \cdot RCOU + 5.536 \tag{4.30}$$

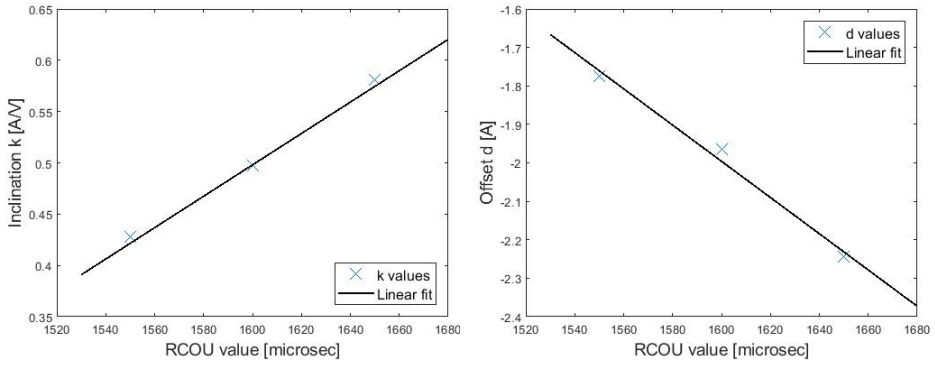

Figure 4.13: k and d values plotted over RCOU with a linear fit. RCOU values ranging from 1550 μs to 1650 μs.

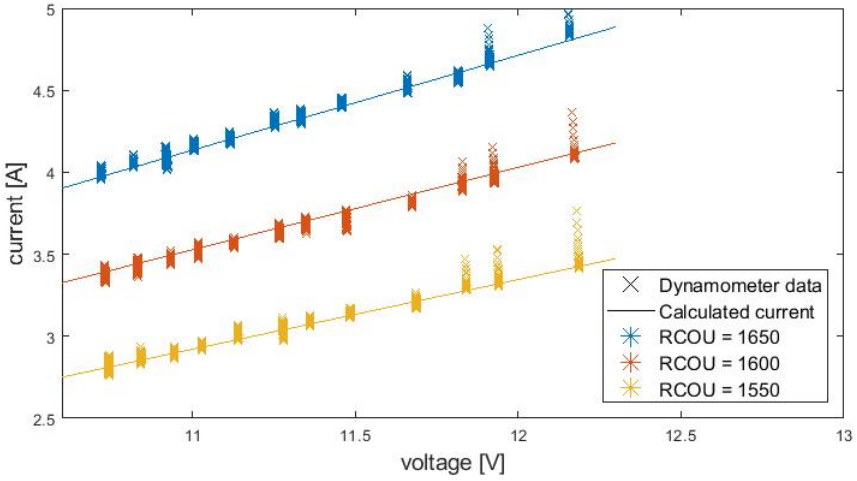

Figure 4.14: Comparison of measured current values and calculated ones based on the model for the limited RCOU range of 1550 μs to 1650 μs. The alignment is good.

4.3 Test Flights

In order to test the method, some test flights have to be conducted. For this, the quadrotor is flown close to a static anemometer providing reference

measurements of the wind speed and direction. Since the method is based on the quadrotor's reaction to the wind, it is important that the drone is not manually controlled by the pilot but flown in an autonomous mode.

4.3.1 The WindSonic Anemometer

A WindSonic anemometer option 1 [21] from Gill Instruments was used for the wind measurements. The 2D ultrasonic anemometer was previously mounted at 6 m height on an antenna mast which is operated by Avinor at Grønnåsen, Tromsø [24]. Due to its low height among the surrounding trees it didn't provide valuable measurements and was therefore dismounted from the mast. A second, identical anemometer is still mounted on this mast at a height of 21 m above the ground, logging the wind speed and direction once every minute.

The programme 'Wind' from Gill Instruments is used to set up the anemometer. Figure 4.15 shows the cable set-up for connecting the WindSonic to a computer. The anemometer is set to measure horizontal wind speed in polar coordinates at the instrument's maximal frequency of 4 Hz. The wind direction is thereby measured clockwise in degrees from north, i.e. wind from east corresponds to a wind direction of 90°.

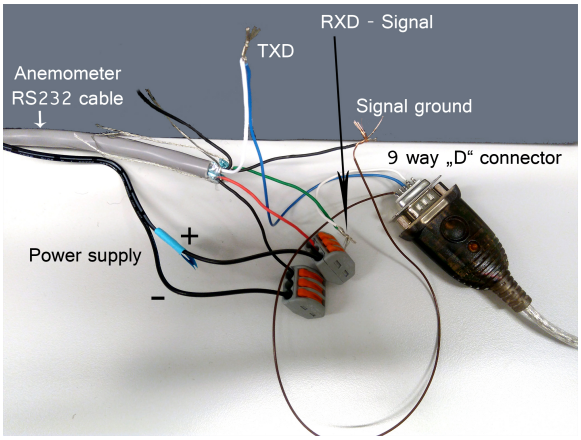

Figure 4.15: Cables connecting the WindSonic anemometer to a computer. [Photo: Simma]

The resolution of the anemometer is given to be 0.01 m/s for wind speed and 1° for wind direction while the accuracy is given by ±2 % for wind speed and ± 2° for wind direction at a wind speed of 12, m/s.

In order to store the measurements, the anemometer was set up together with a SpaceLogger S10 data logger [38]. The logger receives all measure-

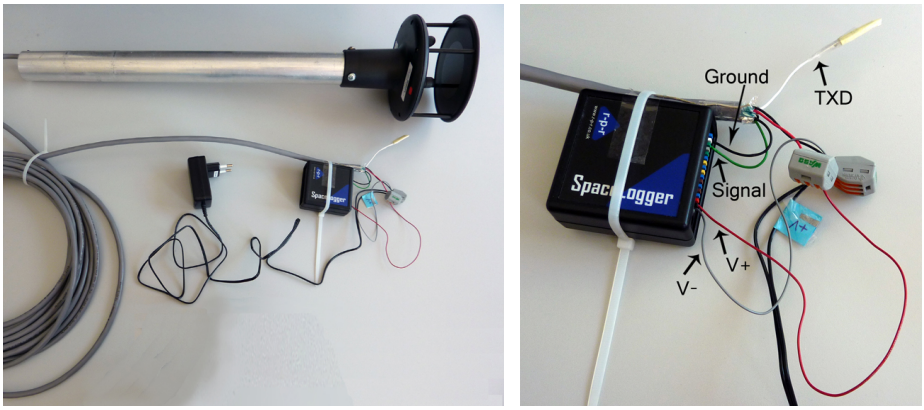

Figure 4.16: Cable connection of the WindSonic anemometer with the SpaceLogger data logger. [Photos: Simma]

ments taken by the anemometer and stores them as a .csv file onto a 2 GB SD card. To initiate a time stamp for the data logging, the SD card contains a set-up file. In this file a certain date and time have to be specified. The card is then inserted into the logger and at the designated time, a small button has to be pressed which sets the time and the logger starts logging. This introduces a small uncertainty in the time measurements. Additionally, the time stamp is only accurate down to the second. Since the anemometer provides measurements four times a second, the error in time is estimated to be ± 250 ms.

Both the logger and the anemometer are provided with 12 V DC current. The wiring for this can be seen in figure 4.16.

4.3.2 Flights at Grønnåsen Ski Jump Tower

The tallest ski-jump tower positioned at Grønnåsen in the centre of the island of Tromsø was picked as the site for some test flights. It provides easy access to install the anemometer high above the ground where wind speeds are higher. Additionally, it is situated close to the university which again makes it very accessible.

The anemometer which is fixed to a round mounting tube with a diameter of 44.45 mm was fastened to a 2 m long quadratic metal pole with a width of 5 cm. This pole was then vertically placed in the corner of the railing of the ski jump tower and fastened to it with several straps as shown in figure 4.17. The correct vertical position of the pole was assured using a water level. The directional orientation of the anemometer was determined from the map shown in figure 4.18 since magnetic compasses were disturbed by the metal construction of the ski jump tower. The error of the anemometer's

Figure 4.17: The WindSonic anemometer mounted on the ski jump tower to measure horizontal wind. [Photos: Simma]

orientation is assumed to be $\pm 5°$.

The ski-jump tower is located within the control zone of the airport meaning that all flight activity has to be coordinated with the Tower [11]. The time window in which flights with UAVs can be permitted is between 11:00 and 13:00 on some weekdays.

The first set of test flights at the ski-jump tower were conducted on 13.02.2018. The IRIS$^+$ took off and landed on the platform just below the mounted anemometer. Three flights were conducted where the quadrotor was manually flown to a position at the same altitude as the anemometer at a distance of about 2 m. There it was changed to Loiter mode, automatically holding its position for about 8 minutes using one full battery.

A second set of test flights was conducted at the ski jump tower on 16.04.2018 with the same flight procedure as in February. However, the anemometer was mounted in two different configurations this time. For the first three flights, the anemometer was mounted to measure both vertical wind velocity as well as the horizontal wind speed in the north-south direction. As can be seen in figure 4.19, this was achieved by fastening the round mounting tube at a 90° angle to the 2 m long quadratic pole which was again vertically placed in the corner of the railing. The round mounting tube was then oriented to face eastwards, resulting in the desired measurement

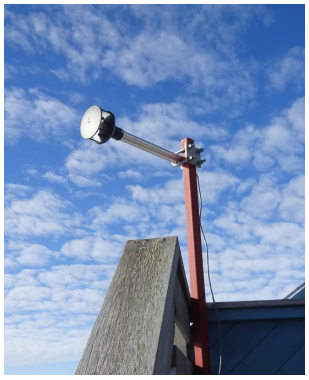

Figure 4.19: Anemometer on ski jump measuring vertical wind. [Photo: Simma]

Figure 4.18: Map of the area where the ski-jump is positioned. The buildings in the bottom right corner of the left image belong to the University of Tromsø. The map on the right shows a compass centred in the position of the anemometer. The angle between magnetic north and the railing used to align the anemometer is shown to be 50 ± 2 degrees. Maps taken from [2].

directions of the anemometer. The last three test flights were conducted with the same anemometer configuration as for the February measurements.

In total, six test flights were conducted between 11:00 and 13:00 that day. For both anemometer configurations, the drone was positioned south of the anemometer for two whole flights, while it held its position east of the anemometer for one. While in the eastern position, the quadrotor started facing south. After about half the battery time, the quadrotor was rotated on the spot to face east for the rest of the battery time. In the southern position, the quadrotor held its heading for a whole battery time, facing south and east respectively.

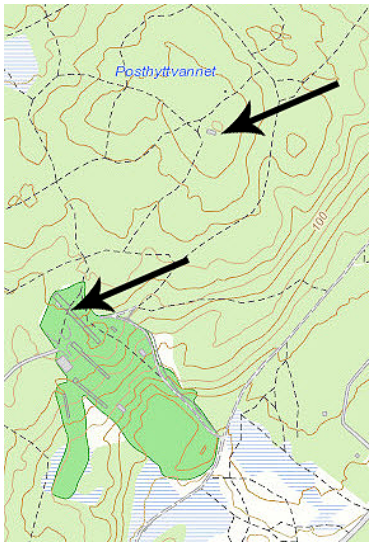

Figure 4.20: Map indicating positions of the anemometers mounted on the ski jump and Avinor's antenna mast. Map taken from [2].

As mentioned previously, a second WindSonic anemometer is permanently installed on an antenna mast operated by Avinor. Figure 4.20 shows the position of the mast as well as the position of the anemometer that was mounted on the ski jump. The distance between the two anemometers is

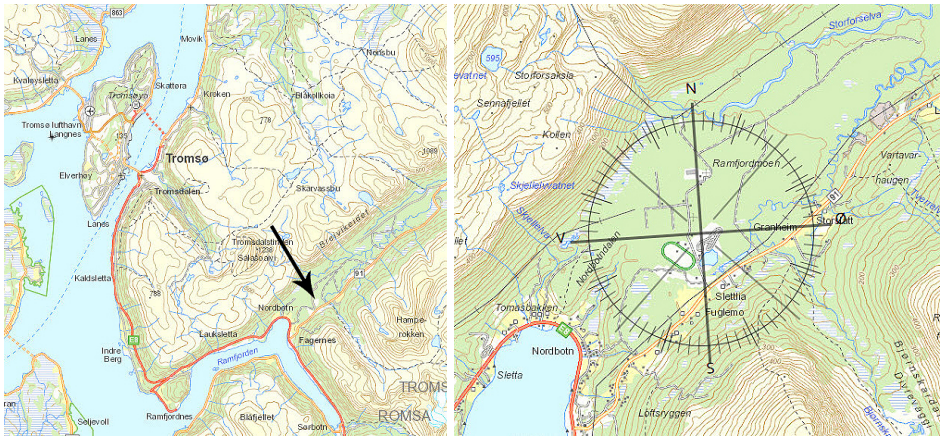

Figure 4.21: Maps of the Ramfjordmoen area showing the test flight site and its orientation. Maps taken from [2].

240 m [2]. Data from the anemometer on the mast was collected after the conduction of the test flights at the ski jump tower. This anemometer is also set up with a SpaceLogger S10 and measures wind speed and direction once every minute. Due to the closeness of the two anemometers, similar wind conditions at the two sites are to be expected. However, the anemometer mounted on the ski jump tower might be affected by rotors and turbulence caused by the structure of the ski jump. The aim in collecting data from the permanently installed anemometer is to compare the general wind conditions to the measurements from the ski jump in order to evaluate the disturbances that might occur.

4.3.3 Flights in Ramfjordmoen

On 27.04.2018 another set of five test flights was conducted at Ramfjordmoen motorstadion, which is in a valley about 12 km inland from Tromsø. Figure 4.21 shows the test flight site marked on a map. As can be seen, the valley is quite big and laminar flow is expected. Figure 4.22 depicts the two anemometer configurations that were used and the quadrotor hovering close by. As in the last test flights at the ski jump, the anemometer was used both in a vertical and a horizontal position. The 2 m long pole was stuck in a heap of snow keeping it stable and the anemometer and data logger were powered by a battery of the same type as the ones used in the quadrotor, providing 12 V.

The first three flights were conducted with the anemometer measuring the vertical and the horizontal north-south wind component. The quadrotor was hovering in a different position for each flight, but with roughly the same ori-

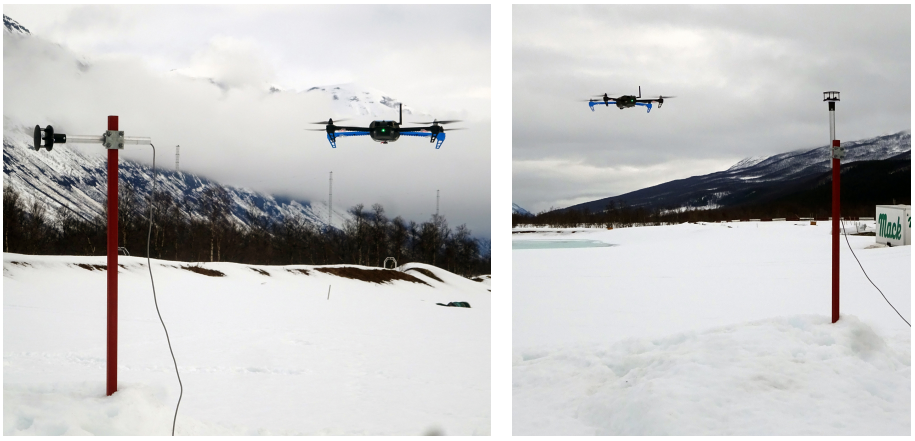

Figure 4.22: Ramfjordmoen test flight site with two different anemometer configurations and the quadrotor flying close to it. [Photos: Simma]

entation. For the last two flights, the anemometer measured both horizontal wind components and again the quadrotor was held in two different positions but with about the same heading. For each flight, the quadrotor held its position in Loiter mode until the battery's charge was depleted. Care was taken, that the quadrotor was not positioned in front of the anemometer, as seen by the wind, which was coming from a north-eastern direction.

4.4 Data Analysis

All MatLab codes discussed in this section can be found in the appendix.

4.4.1 Importing Data to Matlab

The measurements made in flight are stored in a .log file named with the date and time of the flight. It can be accessed by connecting the quadrotor to a computer. With the Mission Planner software from ArduPilot [9] the .log file can be transformed into a MatLab file. The option for this can be found in the tab *Flight Data - DataFlash Logs*. The created MatLab file contains the data organised in numerical matrices where each matrix represents a data group containing the respective variables. A number of cell arrays containing the lables for each data group matrix are given as well.

In order to extract the relevant information and save it in a more structured form, the MatLab function *MRdataCutMean4.m* was created. It extracts the relevant measurements, cuts them down to a defineable time interval and saves the data into a structure arrray. Additionally, the function calculates

a mean value for each variable over the defined time interval and creates a series of plots. An example of how to call the function is given below.

```
filename = '2018-02-13 11-15-25.log-161762.mat'; %data to load
t0 = 293807;    %defines start point for new time vectors [ms]
tstart = 0;         %starttime measured from t0 [ms]
                    %(i.e. 93e3 = 93 s after t0)
tend = 822346 - t0; %endtime measured from t0 [ms]
plots = 1;          %to turn plots on/off [1/0]

Flight1 = MRdataCutMean4(filename,t0,tstart,tend,plots);
```

`filename` defines the data file to load. The time `t0` is used as a starting point for the new time vector created by the function. This could for example be the time of take off. The start- and endtime `tstart` and `tend` define the time interval the data is cut to, measured from `t0`. The variable `plots` can be used to suppress the creation of plots.

In this case, data from one of the flights at the skijump is loaded. How the relevant time interval is found is described in the following section. The time-cut vectors are returned to the structure array `Flight1`. As an example, the stored longitude data can be accessed via `Flight1.GPS.long`.

4.4.2 Finding the Right Timeframe of the Measurements

Since the quadrotor has to be flown to and from the desired measuring spot, the start and end time of the actually valid data has to be determined. This can be easily done by looking at the ThrIn command which is to be found in the CTUN data group in the pixhawk log. It documents the command inputs given through the controller. When the quadrotor is set to Loiter mode, all control sticks are released and the ThrIn value stays constant. Thus start and end times can be found between which the ThrIn is constant. To check their validity, the flight path between those two points in time can be plotted.

The time measurements given in every data group are measured in ms from the quadrotor's initiation. This will further be referred to as UAV time. To transform this into local time, the GPS data group has to be consulted. In this group both the UAV time and GPS time are given, through which a connection can be found. GPS time is measured in weeks from 06. January 1980 and in milliseconds within the week. This can then be translated to local time (GMT+1) by consulting a GPS to UTC time converter [26]. It should be noticed that GPS time currently is 18 s ahead of UTC time due to leap seconds which are ignored by GPS time. The mentioned GPS to

UTC time converter does not account for those. Furthermore, one should be aware of summer and winter time when transforming to local time.

4.4.3 Adding Anemometer Data

Since the time stamp of the anemometer data is given in local time, `t0`, `tstart` and `tend` have to be transformed to local time as described in section 4.4.2 to identify the relevant anemometer data. As mentioned earlier, the time stamp is only accurate down to the second with four measurements taken per second. Those measurements are therefore assumed to be taken at .00, .25, .50 and .75 s every second. Thus if for example `tstart` is found to be at 32.684 s, the first anemometer measurement after `tstart` is at $t_{A1} = 32.750\,s$. Since the time vectors of the IRIS+ data are measured in milliseconds from `t0`, an according time vector for anemometer data is created. The first anemometer measurement is therefore marked to be taken at $t_{A1} - t0$ while the time interval between all consecutive measurements is 250 ms.

This time vector together with the amplitude and angle of the measured wind velocity are added to the structure array `Flight1` as a substructure. The values can be accessed through `Flight1.Anem.time`, `Flight1.Anem.ampl` and `Flight1.Anem.angle` respectively.

4.4.4 Creating Uniform Time Vectors

Now that all the measurements are stored in a single structure array, they can be modified to have a uniform time description. This is necessary because the different data groups store their measurements with different sampling rates with slightly varying intervals between measurements. Thus vectors from different data groups cannot simply be used together, since they do not agree in time. The data groups providing relevant measurements for the further calculation of wind velocity are specified in table 2.2. Of those, the IMU group has the highest sampling rate of about 40 Hz, while the data groups ATT and RCOU sample at approximately 10 Hz, GPS at 5 Hz and the CURR group at ca. 0.98 Hz. The anemometer measures at 4 Hz.

In order to create a uniform time vector for all measurements, time is divided into time-bins of a specified length. All measurements of the same kind taken within one time-bin are averaged giving one measurement per time-bin. As a result, new vectors are created for all measurements that agree time wise and can therefore be used together in calculations. The MatLab function *CreateTimeBinnedVectors.m* is created for this purpose and the file *CalcBin.m* is used to run the function for all measured variables of the data

groups IMU, ATT, CURR and RCOU. The GPS data, though needed for calculations later on, is excluded for now, as it needs to be modified before creating time-binned vectors.

The length of the time-bins can be chosen freely and 0.5 s provides a good starting value. However, it should be noted that problems might occur if this interval is chosen too small. For variables with a low sampling rate some bins might then not contain any measurements and thus return `NaN` in the time-binned vector which causes problems further on.

Since the battery voltage is measured just below once every second, it is interpolated before creating the time-binned vector to prevent this problem. This is done by adding multiple data points in between each measured value with the added points taking the value of their nearest measured neighbour. This provides enough data points for a bin-interval of 0.5 s. The interpolation is done with the file *InterpolatingVoltage.m*.

4.4.5 Parameters and Variables

The MatLab file *Parameters.m* is used to define the parameters specified in table 4.1. The derivation of the needed variables as specified in table 4.2 is done in the file *Variables.m*.

The 3D acceleration $\vec{a}$ is given by the accelerometer measurements which are not further modified.

The current is calculated from measured voltage and RCOU values. Since the assumption was made that aerodynamic conditions for all four rotors are the same, the mean value of all four RCOU values is used in the calculation. From the flight data, which is exemplified in figure 4.23 for one of the flights at the ski jump, it is found that the mean RCOU value is mostly confined to an interval of $1550 - 1650\,\mu$s for the quadrotor in Loiter mode, which justifies the use of the limited model for calculating current as described in equations (4.28) to (4.30).

From the flight data it is further found, that the RCOU values corresponding to motors 3 and 4 (clockwise rotation) are generally higher than those of motors 1 and 2 (counter clockwise rotation). This systematic error most likely stems from the opposite rotational direction of the two mentioned motor pairs. It is assumed that the effect of this is cancelled by using the mean RCOU value for current calculations. To minimise the error from this assumption, a second static thrust test could be conducted with a differently rotating motor mounted to the dynamometer. By looking at the connection between RCOU values and the rotational velocity of the propeller for both rotational orientations, the systematic error could better be compensated

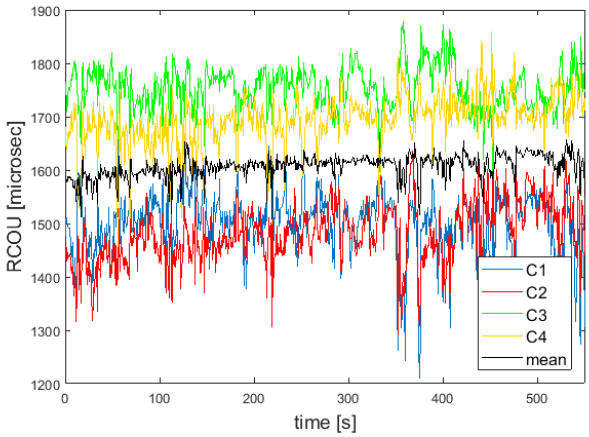

Figure 4.23: RCOU values of the four motors and their mean shown over time for one of the flights at the ski jump. Values of motors 3 and 4 are generally higher than those of the other two motors. The mean RCOU is mostly confined to an interval of $1550\,\mu\text{s} - 1650\,\mu\text{s}$.

for.

When the current is calculated, electrical power is found via $P_{el} = V \cdot i_{calc}$. Based on equations (4.26) and (4.27), the rotational velocity ω and the motor torque τ are then calculated from P_{el}. The rotational acceleration $\dot{\omega}$ of the propeller is further found by taking a time derivative of ω.

The last variables calculated in the MatLab file *Variables.m* are the components of the vehicle's velocity in the inertial reference frame (i.e. relative to the ground). The pixhawk logs a measurement of the vertical velocity in the GPS data group providing a measure of v_g^z. The horizontal velocity is given by the ground speed saved in the GPS data group. As this only gives a speed and no direction, the flight path is consulted. From longitude and latitude measurements, the direction of flight between two consecutive data points can be established. Consequently, v_g^x, v_g^y and v_g^z are found and time-binned vectors of those variables can be calculated as well.

4.4.6 Final Calculations

Now that all necessary parameters and variables are found and stored as vectors in MatLab, equations (4.11) to (4.20) can be implemented to find the quadrotor's air velocity $\vec{v_a} = [v_x, v_y, v_z]^T$. This is done in the MatLab file *CalcVehicleAirSpeed.m* which also transfers the air velocity into the vehicle frame according to equation (4.21) and applies the wind triangle based on equation (4.22). As a result, the local three dimensional wind velocity is

estimated.

Finally, the MatLab file *CalcVehicleAirSpeed.m* implements a comparison of the estimated wind velocity with the actual wind measurements from the Wind Sonic anemometer. The measured wind velocities, which are given in polar coordinates, are therefore transformed to $x-$ and $y-$velocities to make the data comparable and comparison plots are produced.

Based on those plots, the lumped drag coefficient $\bar{c}$ can be determined empirically. This is done by manually adjusting it and comparing the resulting estimate to the anemometer measurements. The $\bar{c}$ value resulting in the best fit can then be found.

Chapter 5

Results

This chapter presents the results from the flight tests that were conducted. It should be noted that estimates for all three components of wind velocity are found from the quadrotor data. However, since the WindSonic anemometer only measures in 2D, just two of the three components of the wind estimate are presented here. Section 5.1 focuses on the results from the flights conducted at the ski jump tower in February while the test flights conducted there in April are presented in section 5.2. The results of the last set of test flights, which were conducted in Ramfjordmoen are shown in section 5.3. In the following, the wind velocities resulting from the quadrotor measurements will be denoted wind estimates, while the anemometer data will be called measurements. This is to simplify the terminology when talking about the results.

5.1 February Flights at the Ski Jump

Figure 5.1 shows the results of the three test flights conducted at the ski jump tower in February. It can be seen that the horizontal wind velocities calculated from the drone measurements exert the same general behaviour as the wind velocities measured by the anemometer. However, the estimates from the drone measurements tend to be too high. The results of the third test flight show a very good correlation between calculated and measured wind speed in the $x-$direction while the behaviour of the estimate in the $y-$direction seems rather uncorrelated except for the time interval between 330 s and 420 s.

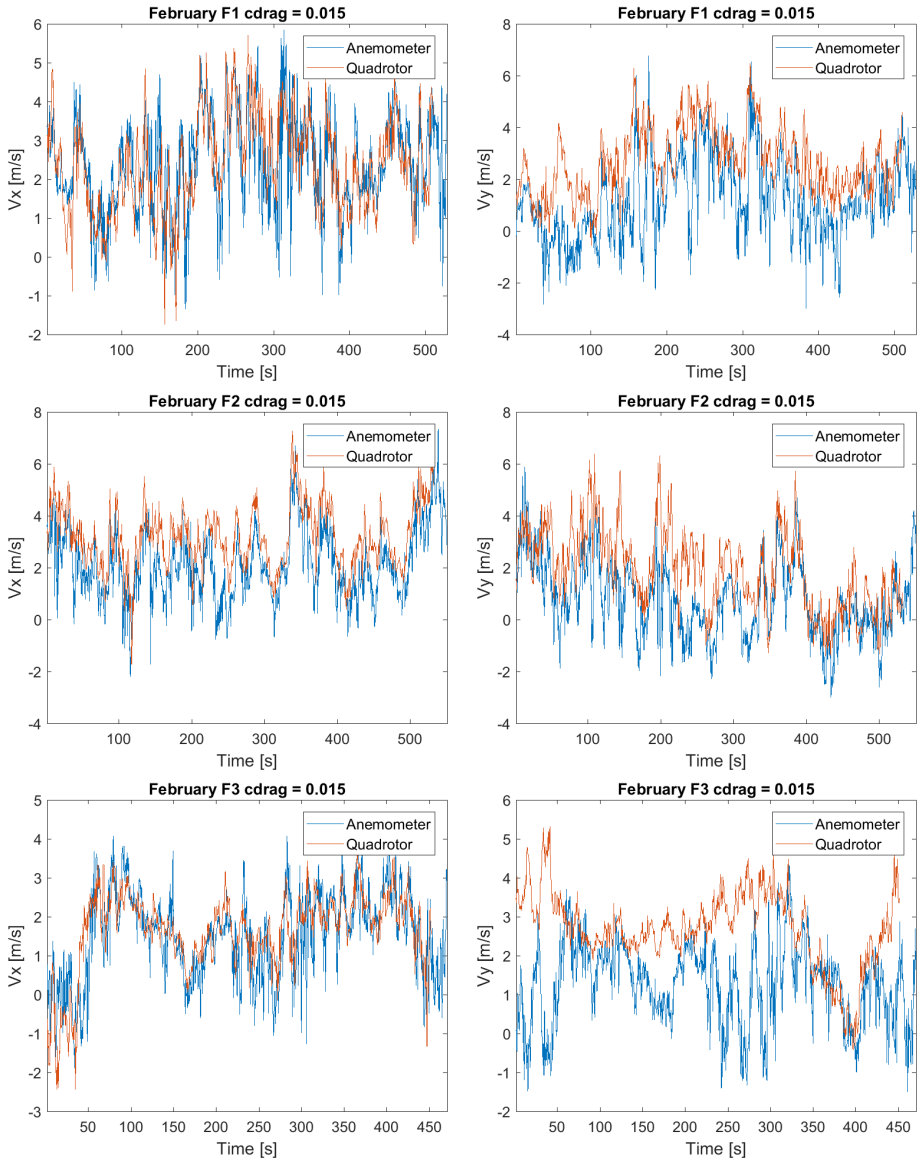

Figure 5.1: Wind measurements done at the ski jump tower in February with the anemometer placed to measure horizontal wind. The quadrotor estimate is shown in red, the anemometer measurements in blue.

5.2 April Flights at the Ski Jump

The results from the test flights conducted at the ski jump tower in April were not as good as the ones from February. The following two subsections present the results for both the vertically and horizontally measuring anemometer.

5.2.1 Vertically Measuring Anemometer

This part presents the results from the first three test flights conducted at the ski jump in April. The flights are numbered to be 1A, 1B, 2 and 3 where A and B indicate the parts of the first test flight with different quadrotor heading. For these flights, the anemometer was mounted in order to measure one vertical and one horizontal wind velocity component. The $x-$component points northwards, while the $z-$direction is defined downwards.

The results in the vertical component do not correspond well and a quite big offset is found between the measured and calculated wind speed. While the vertical speed the anemometer measures is only slightly negative, the estimates from the drone data show vertical wind speeds between -2 m/s and -5 m/s. It should be noted that a positive v_z corresponds to downwards wind due to the definition of the axes. Thus, the quadrotor seems to experience more upwind than the anemometer. As the test site is elevated and on top of a structure, a general upwind (negative v_z) is to be expected.

The estimates of the horizontal wind component follow the general shape of the measurements quite well in flights 1A and 3, however, an offset of up to 0.5 m/s is present. For flights 1B and 2 the estimates do not correlate as well with the measured data. Another observation based on the horizontal components in figure 5.2 is that the calculated results overestimate the wind speed relative to the anemometer measurements in flights 1B and 3 while it is underestimated in flights 1A and 2.

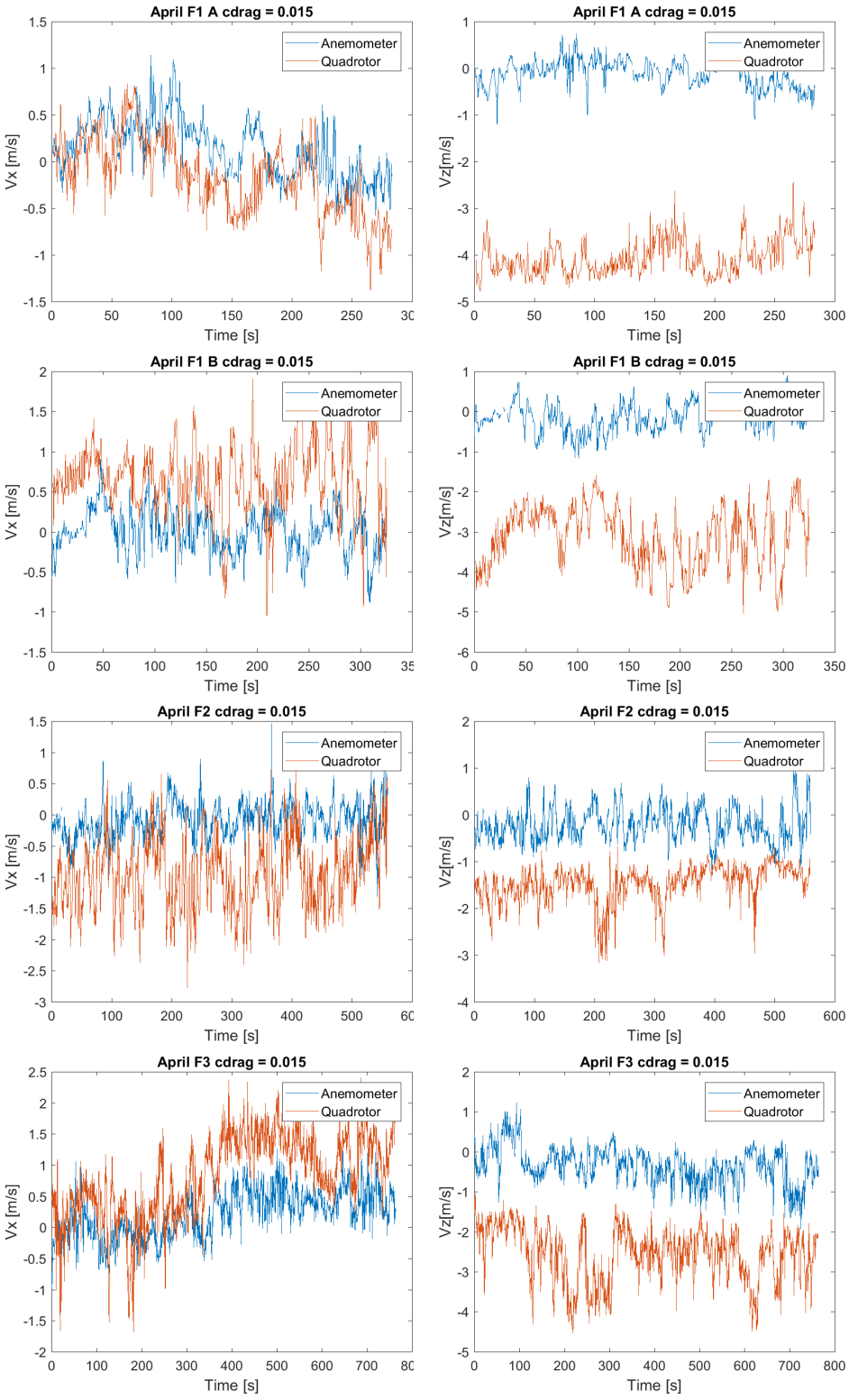

Figure 5.2: Wind measurements done at the ski jump tower in April with the anemometer placed to measure vertical wind. The quadrotor estimate is shown in red, the anemometer measurements in blue.

5.2.2 Horizontally Measuring Anemometer

This part focuses on the last three test flights conducted in April, where the anemometer was mounted in order to measure two components of horizontal wind. The $x-$component is hereby defined to point northwards, while the $y-$component points eastwards. The flights are numbered flight 4, 5, 6A and 6B where A and B again indicate the different headings of the quadrotor in the last flight. Figure 5.3 shows the measured and estimated wind velocities found from the last three test flights conducted at the ski jump tower in April.

When looking at the top images in figure 5.3 depicting flights 4 and 5, fairly good agreement in the results can be seen. In flight 4, the $x-$component of the estimated values have a negative offset of about 0.5 m/s while the $y-$component shows a slightly positive offset of about 0.2 m/s as compared to the anemometer measurements. Apart from these offsets, the estimate follows the wind variations measured by the anemometer exceptionally well.

The results of flight 5 show that the estimate follows the measured velocity variations very well in the $x-$direction. In the $y-$direction this is the case only up to about 400 s after which the quadrotor based wind speeds gravely overestimate the measured ones by about 1 - 1.5 m/s.

The quadrotor estimate from flight 6A follows the general shape of the anemometer measurements while having a negative offset in the $x-$direction and a positive offset in the $y-$direction. In flight 6B, the negative offset in the $x-$direction is smaller while the positive offset in the $y-$direction is larger than in flight 6A. Further, the correlation of the overall shape of the wind measurements is not as good as in flight 6A.

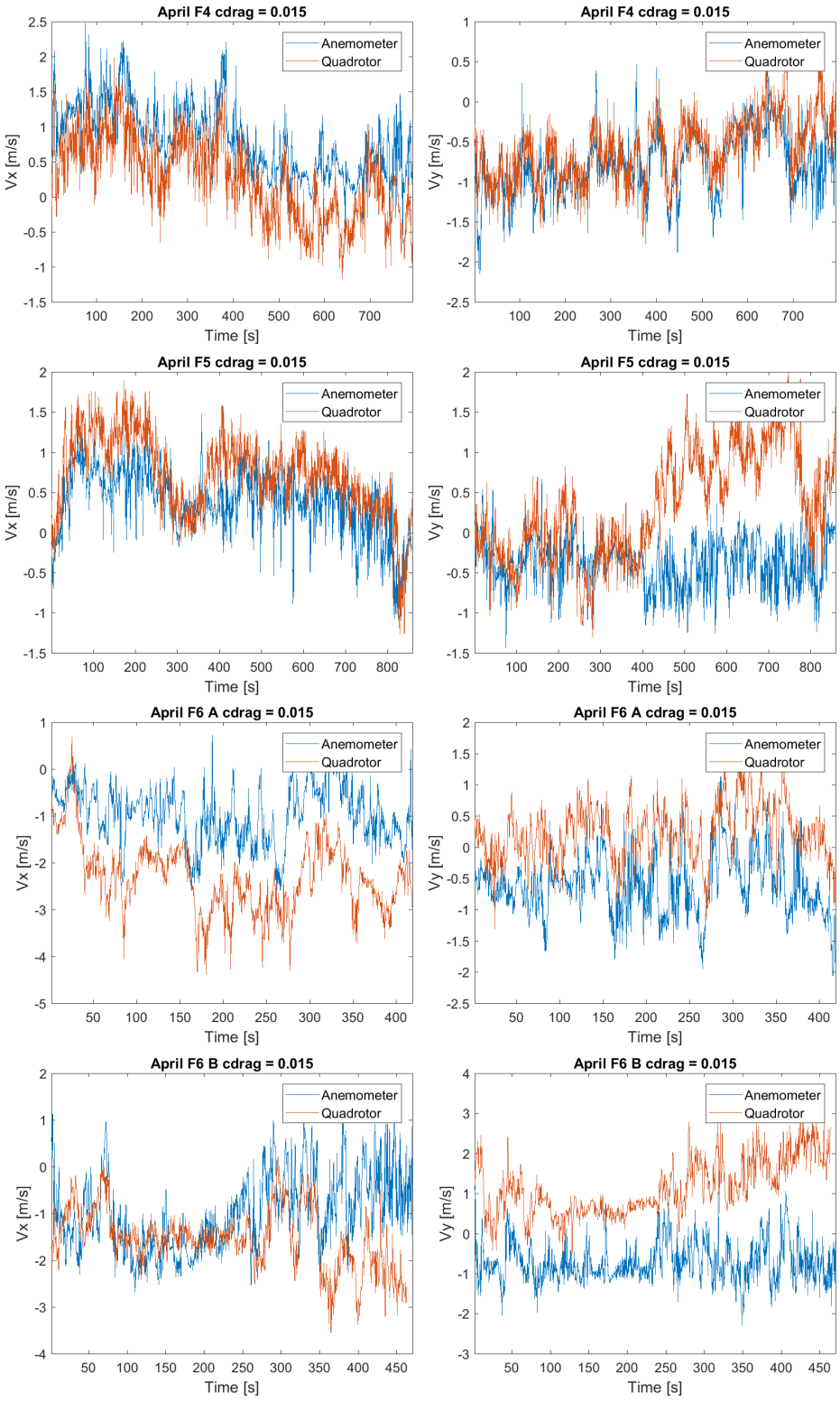

Figure 5.3: Wind measurements done at the ski jump tower in April with the anemometer placed to measure horizontal wind. The quadrotor estimate is shown in red, the anemometer measurements in blue.

5.3 April Flights in Ramfjordmoen

5.3.1 Vertically Measuring Anemometer

Figure 5.4 shows the results from the test flights in Ramfjordmoen, with the anemometer measuring a vertical wind component.

The horizontal component in flights 1,2 and 3 show an overall similar shape of the anemometer measurements and the quadrotor wind estimates. However, an offset of about 1 m/s is observed with the anemometer measuring higher wind speeds in the negative $x-$direction (i.e. stronger winds from north).

The vertical component shows little correlation between the measured and estimated wind speeds. While the anemometer measures wind speeds between ± 0.4 m/s with a slight tendency towards negative wind speeds (i.e. upwind), the quadrotor estimates negative wind speeds of 2 - 3 m/s. The variation in the estimate is also stronger than in the anemometer measurements

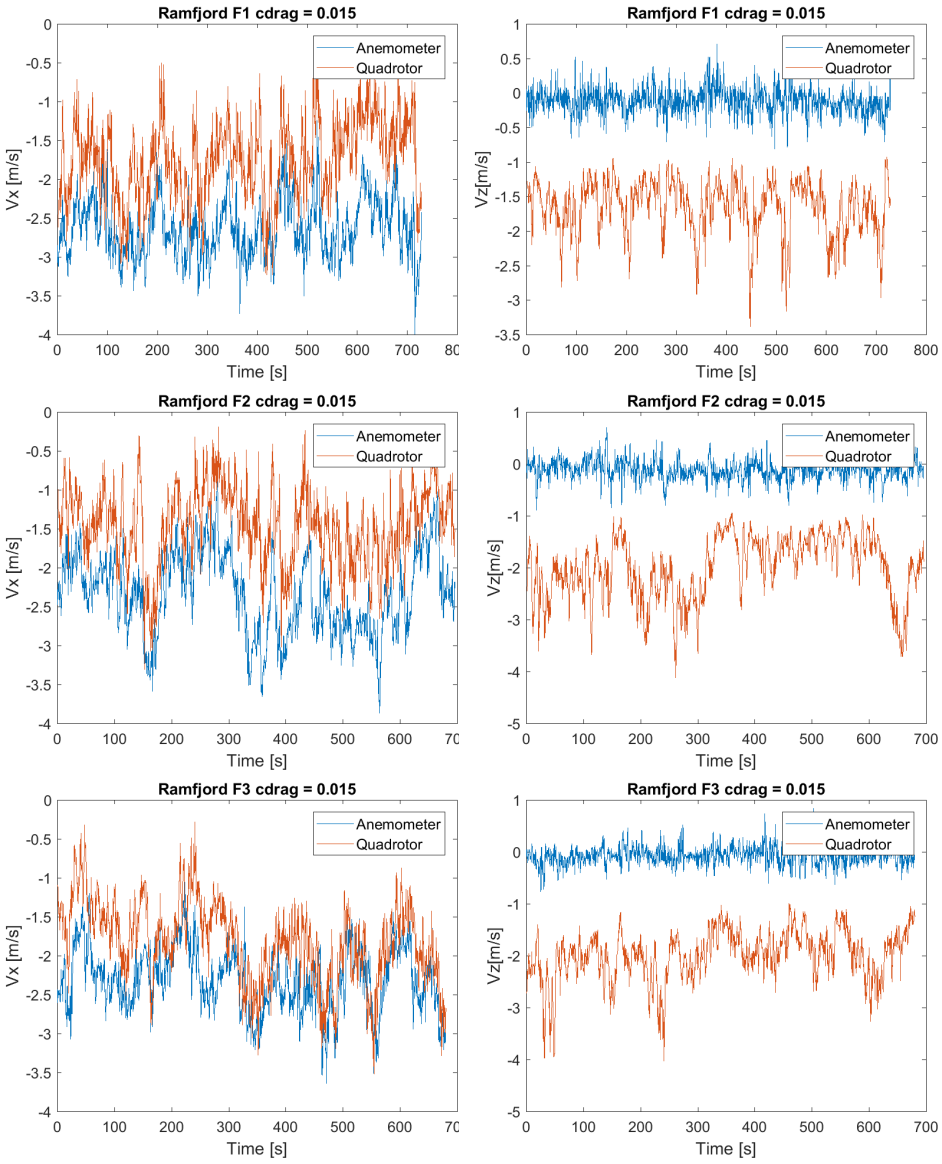

Figure 5.4: Wind measurements done in Ramfjordmoen in April with the anemometer placed to measure vertical wind. The quadrotor estimate is shown in red, the anemometer measurements in blue.

5.3.2 Horizontally Measuring Anemometer

Figure 5.5 shows the results of the flights at Ramfjordmoen which were conducted with the anemometer measuring horizontal wind speeds. For both flights good results are achieved. The estimated wind velocities follow the shape of the anemometer measurements very well. Especially the $y-$component in flight 4 has an exceptionally good correlation between estimate and measurement. A slightly positive offset of the estimate in respect to the measurements is observed in all other components.

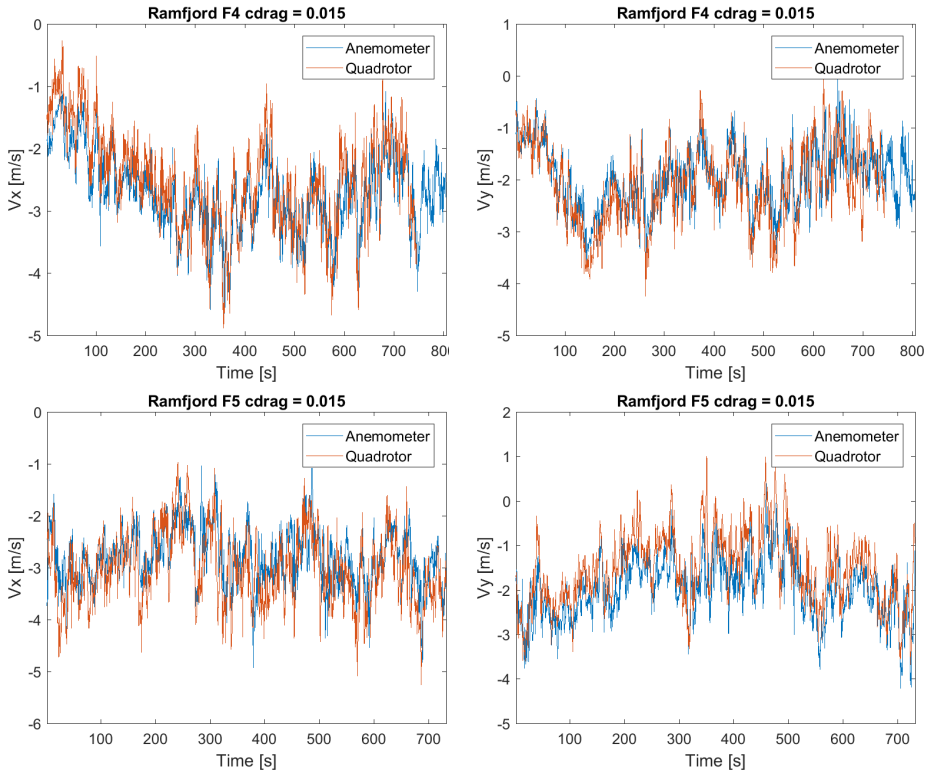

Figure 5.5: Wind measurements done in Ramfjordmoen in April with the anemometer placed to measure horizontal wind. The quadrotor estimate is shown in red, the anemometer measurements in blue.

Chapter 6

Discussion

This chapter provides a discussion of the results and reasons for differences between the estimates and anemometer measurements. Section 6.1 discusses the determination of the drag coefficient and the error connected to it. In section 6.2 the different wind conditions during the test flights and their influence on the results are discussed. Section 6.3 focuses on the reasons for deviations during the test flights with the vertically measuring anemometer, while section 6.4 discusses the results for the horizontally measuring device. Finally, section 6.5 concludes the chapter with other minor sources of error.

6.1 The Drag Coefficient

The drag coefficient $\bar{c}$ is determined by comparing the wind estimate from the quadrotor to the anemometer measurements. Varying $\bar{c}$ in the calculations will effect the shape of the wind estimate. Thus, by comparing the estimate to the measurement for several different $\bar{c}$, an optimal value for the drag coefficient can be found which results in the best match. This was done for both the $x-$ and $y-$component of the three flights in February, flights 4 and 5 conducted at the ski jump in April and flights 4 and 5 conducted in Ramfjordmoen. The other flights were excluded due to the lack of correlation between the estimates and the measurements. Reasons for this will be discussed in the following sections. The values found to result in the best match for the examined flights varied between 0.012 and 0.018 and a mean value of $\bar{c} = 0.015$ was determined. The standard deviation is found to be 0.0023. A higher accuracy could be achieved by considering data from more test flights.

To exemplify this, figure 6.1 shows the comparison of the estimate and measurement in the $x-$direction for flight 5 conducted in Ramfjordmoen. This

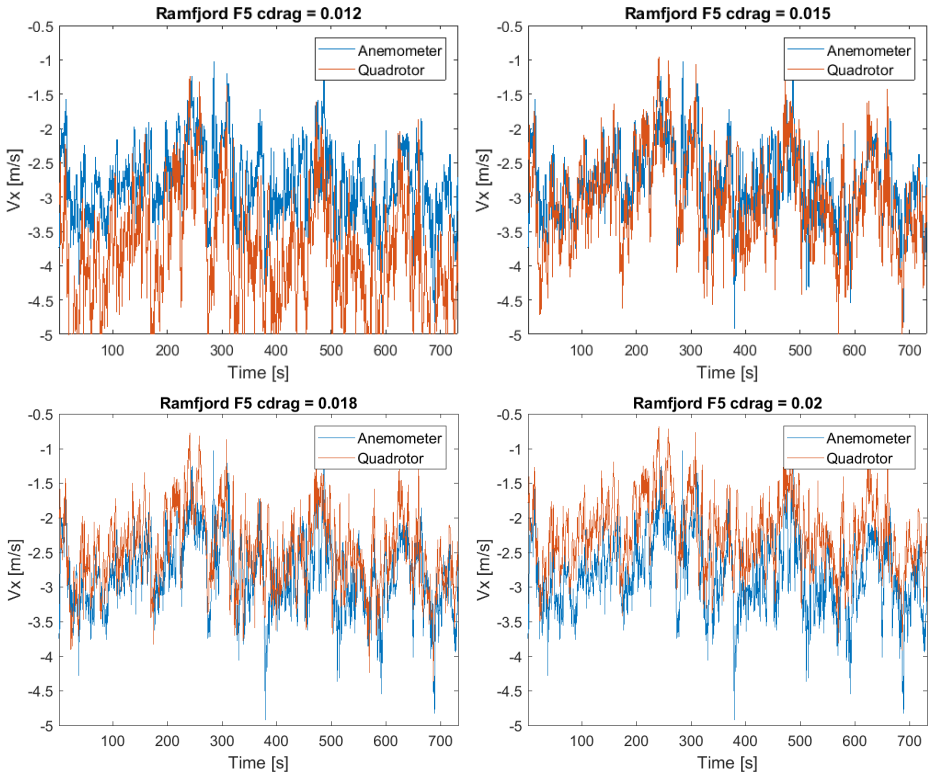

Figure 6.1: The effect of different drag coefficients $\bar{c}$ on the wind estimate in the $x-$direction shown for flight 5 conducted in Ramfjordmoen. Top left: $\bar{c} = 0.012$, Top right: $\bar{c} = 0.015$, Bottom left: $\bar{c} = 0.018$, Bottom right: $\bar{c} = 0.020$. The best fit is found to be with $\bar{c} = 0.015$.

is done for four different drag coefficients. It can be seen that a higher drag coefficient results in a higher estimate of wind velocity (i.e. less negative) with lower variation. Similar plots of other flights with the wind velocity lying in the positive range show the opposite behaviour, i.e. for higher $\bar{c}$ the estimate approaches lower wind values with the variation shrinking as well. Thus, in general a higher drag coefficient will shift the estimate towards zero and reduce the amplitude of the variation.

The predominant cause for the error in $\bar{c}$ is different wind conditions experienced by the quadrotor and the anemometer. Since the determination of the drag coefficient is based on a comparison of the quadrotor estimate and the wind velocities measured by the anemometer, different wind conditions will affect the findings of $\bar{c}$ gravely. Such variations in wind conditions can occur due to turbulence in the area or the anemometer being affected by the quadrotor's downwash, i.e. the air stream produced by the rotors. Optimally, measurements would be conducted in a wind tunnel, where all wind parameters are known. For test flights conducted outdoors, the variance in

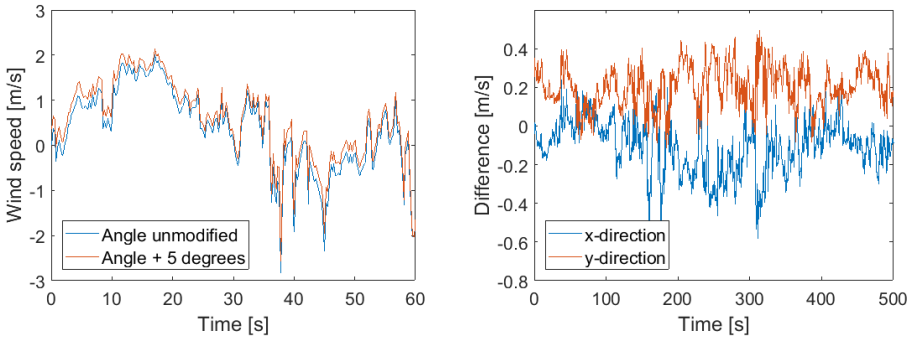

Figure 6.2: Error in measured wind velocity based on the anemometer being oriented 5° away from north depicted for flight 1 conducted in February. Left: Anemometer measurements in the $y-$direction compared to the wind speed resulting from the angle measured by the anemometer being modified with $+5°$. Right: Difference between the velocity resulting from a $+5°$ modification in anemometer angle and the unmodified data. This is shown for both the $x-$ and $y-$direction. Differences of up to 0.4 m/s are found.

wind has to be considered.

Further factors affecting the accuracy of the drag coefficient are the uncertainties in the measured and estimated wind velocities. One source of error is the anemometer orientation. As described in section 4.3.2, the error of the anemometer's orientation is assumed to be $\pm 5°$. Figure 6.2 shows the wind speed measured by the anemometer exemplified for the $y-$direction of flight 1 in February. For the figure, the wind direction measured by the anemometer was modified by $+5°$ and the result plotted in the left image compared to the unmodified measurements to show the effect of this error. The right image is the subtraction of the unmodified wind speed from the one resulting from this angle modification. This is done for both the $x-$ and $y-$direction showing offsets of up to 0.4 m/s.

It should be kept in mind that the found drag coefficient of 0.015 still has a relatively large error. As it is used in the calculations of the wind estimate based on quadrotor data, offsets between these estimates and the anemometer measurements in the figures in chapter 5 might be a result of this uncertainty in $\bar{c}$. Based on figure 6.1 these offsets could be up to about 0.4 m/s. Again, this accuracy can be improved by analysing data from multiple, reliable test flights.

6.2 Wind Conditions During Test Flights

For the three sets of test flights that were conducted, the wind conditions were quite different. In order to illustrate this, figures 6.3 and 6.6 indicate the quadrotor's heading angle and the direction of the wind for all the different flights. Additionally, the anemometer's position is indicated relative to the quadrotor's position as well as whether the device is measuring vertically or horizontally. The distances in the sketches are not to scale.

It should also be noted that the indicated wind direction is a mean value from the anemometer measurements throughout the duration of the flight. The actual direction of the wind might vary with time. For the vertically measuring anemometer, the horizontal wind direction cannot be extracted. For the first three flights at the ski jump tower in April, no wind indication is therefore given. For the first three flights in Ramfjordmoen, the indicated wind direction is the same as the one measured during the last two flights. This is a good estimate, since the wind was quite stable and not changing direction at this site.

6.2.1 Flights at the Ski Jump

For the test flights conducted at the ski jump, very different wind conditions were measured which influence the results greatly. This motivates a short discussion on how the structure of the ski jump influences the air flow for wind from different directions. The left image in figure 6.5 shows the orientation of the ski jump. Since the anemometer is positioned on the slope side of the ski jump tower, it stands quite freely against wind coming onto the ski jump from that side. Wind coming from the opposite direction will hit the tall side of the ski jump first and the air will be redirected by it before reaching the anemometer behind it. Additionally, the stairs to reach the top of the ski jump are on the north-east side of the structure, meaning the anemometer is more hidden from wind coming from that direction as opposed to wind from south-west. The assumption based on all these observations is, that wind coming from an eastern to south-western direction should not be gravely disturbed by the structure, though it might be enhanced by the slope of the ski jump creating upwind. Wind coming from other directions are more likely to create rotors and turbulence at the placement of the ski jump anemometer.

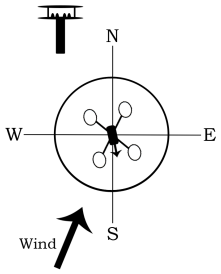

Feb. Flight 1

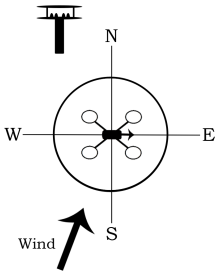

Feb. Flight 2

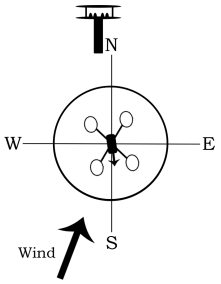

Feb. Flight 3

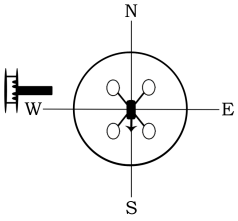

Apr. Flight 1A

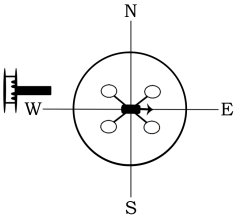

Apr. Flight 1B

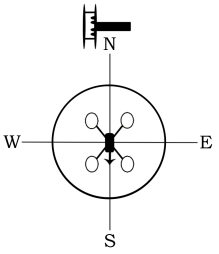

Apr. Flight 2

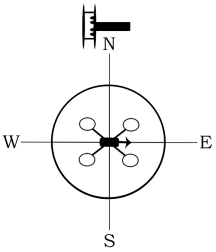

Apr. Flight 3

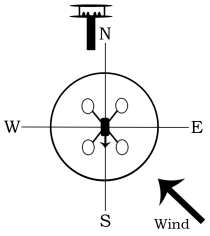

Apr. Flight 4

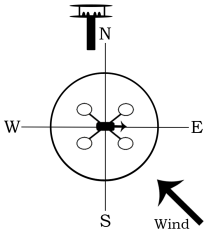

Apr. Flight 5

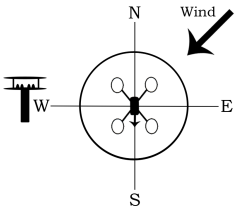

Apr. Flight 6A

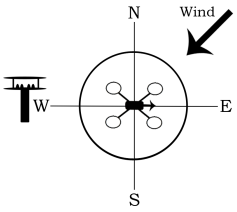

Apr. Flight 6B

Figure 6.3: Sketches indicating the quadrotor's heading angle, the wind's general direction and the quadrotor's position relative to the anemometer for the test flights conducted at the ski jump tower in February and April. Distances are not to scale.

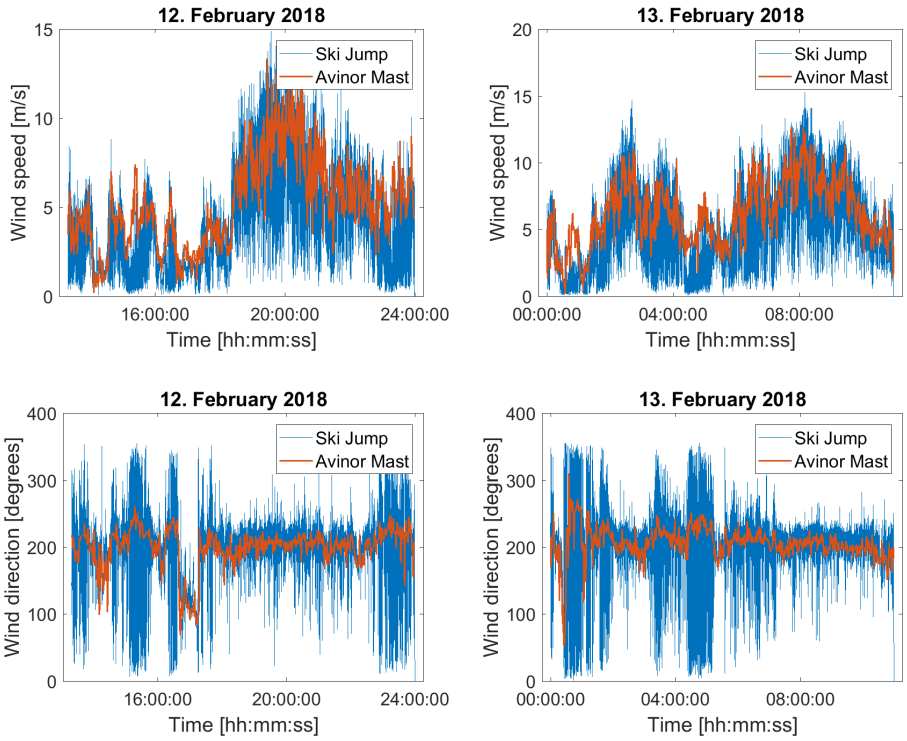

Figure 6.4: Wind speed and direction measured by the AM anemometer and the SJ anemometer between 13:19 on 12.02.2018 and 11:00 on 13.02.2018.

One way of verifying this assumption is by considering the data collected by the anemometer which is permanently installed on the nearby antenna mast operated by Avinor. This will further be referred to as the Avinor mast (AM) anemometer, while the anemometer mounted on the ski jump will be named the ski jump (SJ) anemometer. Since the distance between the two anemometers is a mere 240 m, it is assumed that the wind conditions at the two sites would be nearly identical, had there not been a ski jump tower disrupting the air flow.

The SJ anemometer was only temporarily installed for the durations of the two sets of test flights. For the flights in February though, it was mounted on the day prior to the conduction of the test flights and was measuring continuously from 13:19 on 12.02.2018 to 13:00 on 13.02.2018 when the test flights were concluded. Figure 6.4 shows the data from the almost 22 hours of measurements without a quadrotor present compared to the data collected by the AM anemometer. The top figures show the wind speed while the bottom figures show the wind direction. Although the data from the SJ anemometer shows more noise, both anemometers seem to measure similar wind conditions for the whole time period given. Thus, the measurements from the Avinor mast can be used as an indication for the general behaviour

of wind in the area. Nevertheless, deviations in the wind velocity measured at the SJ will occur, due to the structure of the ski jump. The wind direction from the measurements shown in figure 6.4 was mostly centred around 200°, i.e. south-south-western wind, which confirms that the wind flow reaching the SJ anemometer from that direction is not significantly disturbed by the structure of the ski jump, though some deviations remain.

February

During the conduction of the test flights at the ski jump in February, both anemometers again measured the same general wind direction with wind speeds of up to 6 m/s. The wind was coming from a south-south-western direction, implying little influence of the ski jump structure on the air flow. The resulting estimates for those flights (figure 5.1) therefore agree with the anemometer measurements quite well, though some offsets, especially in the $y-$component of flight 3, remain. Those could still be due to momentarily different wind conditions at the sites of the anemometer and the quadrotor.

April

During the test flights at the ski jump in April, the wind conditions were less stable and the wind was coming from more unfortunate directions, where the anemometer was more obstructed by the structure of the ski jump. The right image in figure 6.5 shows the wind directions measured by the SJ anemometer compared to the AM anemometer. The former are hereby indicated with blue arrows, while the latter are shown in red. For the first three flights, no wind direction was measured by the ski jump anemometer, since it was measuring vertically. For **flights 1 and 2**, the AM anemometer detected west-north-western wind, which is not very fortunate for the given placement of the SJ anemometer and different wind conditions are to be expected at the positions of the SJ anemometer and the quadrotor. During **flight 3**, the wind direction found by the AM anemometer was south-south-eastern, which should lead to less disturbance influencing the SJ anemometer. Considering the $x-$components in figure 5.2, the estimate in flight 3 does indeed show the best correlation with the measurements of the first three test flights at the ski jump in April. Nevertheless, the estimate still shows rather large deviations, possible reasons for which will be discussed in section 6.3.

For the last three test flights, where the anemometer was measuring horizontally, measurements of wind direction are depicted in figure 6.5 for both anemometers.

During **flight 4** both anemometers measured south-eastern wind with a

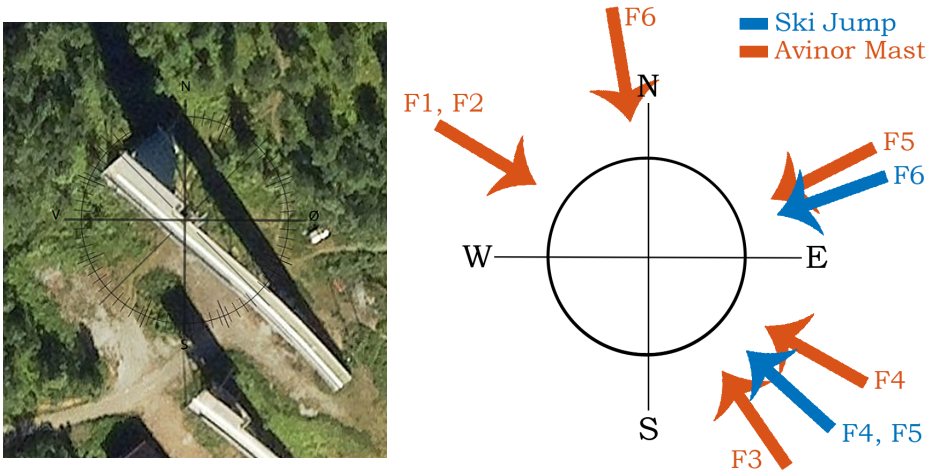

Figure 6.5: Left: Satellite image of the ski jump with a compass centred in the position of the anemometer. Image taken from [2]. Right: Compass rose with arrows indicating wind directions for the six test flights conducted at the ski jump tower in April. The red arrows indicate the wind direction measured by the AM anemometer and the blue arrows indicate the wind direction measured by the SJ anemometer.

deviation of only up to 20°. This is a wind direction which should result in little disturbance by the ski jump structure and indeed, of these last three test flights (see figure 5.3), flight 4 gives the best results.

The AM anemometer measured east-north-eastern wind during **flight 5** while the SJ anemometer still measured south-eastern wind. This could suggest the presence of wind rotors around the ski jump anemometer as a result of the wind blowing sideways onto the ski jump. The results (figure 5.3) are still quite good up to about 400 s into the flight. After that, the $y-$component of the quadrotor overestimates the anemometer measurements by 1.5 m/s. The reason for this could be a change in wind direction. The AM anemometer shows a mean wind direction of 94° during the first 400 s of flight time, while the mean for the second part of the flight was 39°. Figure 6.3 shows that the quadrotor was positioned south of the anemometer for this flight. It was hovering at a horizontal distance of about 2 - 3 m from the anemometer but at roughly the same height. This means that the quadrotor was positioned at a greater distance from the structure of the ski jump. Thus when the wind direction was changing from being easterly to being north-easterly, the anemometer would have become more obstructed by the ski jump while the quadrotor might have been less influenced by this. It is therefore assumed, that the wind conditions for this part of the flight were not the same at the positions of the anemometer and the quadrotor causing the discrepancies between the estimate and the measurements.

During **flight 6** the AM anemometer measured northern wind while the SJ anemometer detected wind from an east-north-eastern direction. Since the wind was now hitting the ski jump at the tall side first, the presence of rotors seem a reasonable explanation for the different wind directions measured. This also explains the disagreements between the estimates and measurements for parts A and B of this flight in figure 5.3.

6.2.2 Flights in Ramfjordmoen

At the test site in Ramfjordmoen, where the last set of flights was conducted, quite laminar flow was expected, especially since the wind was coming from a north-eastern direction, i.e. coming out of the valley (see figure 4.21). Although the results from the vertically measuring anemometer are not very good, the estimates from the last two flights, with the anemometer measuring horizontal wind, fit the measurements exceptionally well. This indicates that the wind conditions were indeed almost identical at the positions of the quadrotor and the anemometer.

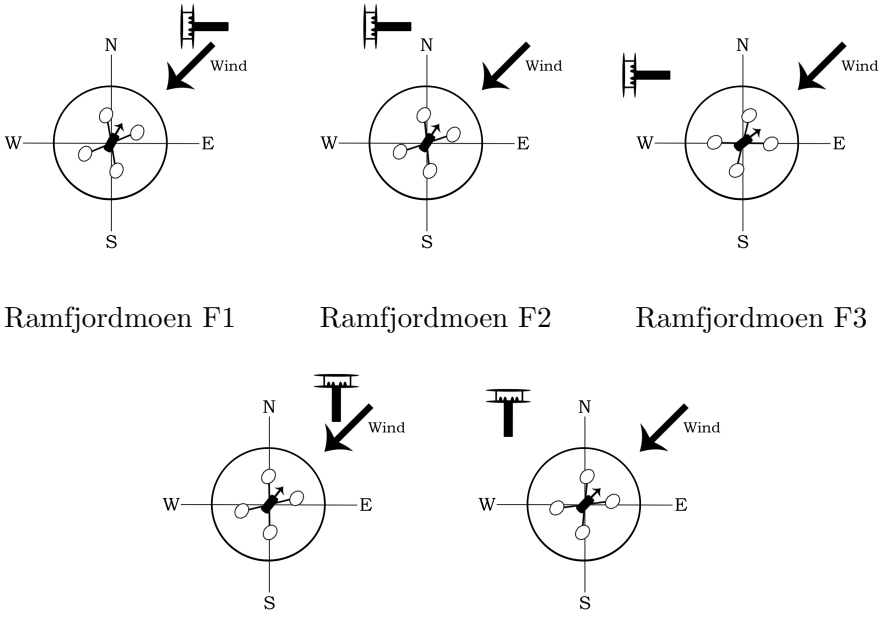

Figure 6.6: Sketches indicating the quadrotor's heading angle, the wind's general direction and the quadrotor's position relative to the anemometer for the test flights in Ramfjordmoen. Distances are not to scale.

6.3 Vertically Measuring Anemometer

From figures 5.2 and 5.4, which show the results from the vertically measuring anemometer configurations used in the last two sets of test flights, it can be seen that the estimates do not agree with the measurements well. As discussed in section 6.2, different wind conditions at the anemometer and the quadrotor might have an impact on this, however, some other influences might be predominant. These will be discussed in this section.

6.3.1 Anemometer Causing Turbulence

One problem could be the anemometer causing turbulence when positioned to measure vertical wind. The WindSonic is designed to be used horizontally as it measures the air flow between two flat, round plates. In places this anemometer would commonly be used, horizontal wind speeds will be predominant with only small vertical wind velocities. When placing the anemometer at a 90° angle to its intended orientation, the stronger horizontal winds can hit the round plates of the anemometer at an angle which was not intended for this device. This might cause rotors and turbulence affecting the measurements. If the wind was flowing in the north-south direction, aligned with the orientation of the anemometer, this effect would be negligible. However, during the test flights, the wind was coming from a north-eastern or eastern direction, meaning it would hit the anemometer at an angle and possibly cause disturbances of the measurements. To quantify this disturbance, tests could be made with the anemometer in a wind tunnel or similar set up. Using a different type of anemometer, ideally a 3D ultrasonic anemometer, would eliminate this problem. For the given results, it is reasonable to conclude that the turbulence caused by using the WindSonic anemometer vertically is the main cause for the discrepancies between the measurements and the estimates in the horizontal component. While it does influence the vertical component similarly, the larger discrepancies found there must have a different cause.

6.3.2 Quadrotor Downwash

When looking at the vertical component of the results, the large offset between the estimates and the measurements is evident. The offset varies between 1 - 4 m/s in all the vertical measurements and the overall shape of the estimate does not agree with the shape of the anemometer measurements. One possible explanation could be that the anemometer is affected by the downwash produced by the quadrotor and thus seeing less upwind than the quadrotor.

During the test flights for this thesis a distance between the quadrotor and the anemometer of about 2 m was kept. This is based on the findings of Wolf et. al. [43], that for a comparable quadrotor, the interference of the quadrotor induced airflow is minimal at the horizontal distance of at least 0.7 m from the drone's centre of gravity. However, the downwash can affect the anemometer measurements if the quadrotor is positioned above the anemometer or tilted away from it. Since the quadrotor angles itself to stand against the wind, its downwash is not straight down, but angled slightly away from the wind. Thus, if the anemometer is positioned behind the quadrotor, it will be more affected by this downwash than if it were positioned next to the quadrotor as seen from the direction of the wind. The anemometer's measurements will be most affected by this downwash in the vertical direction, as the tilting angles of the quadrotor are small.

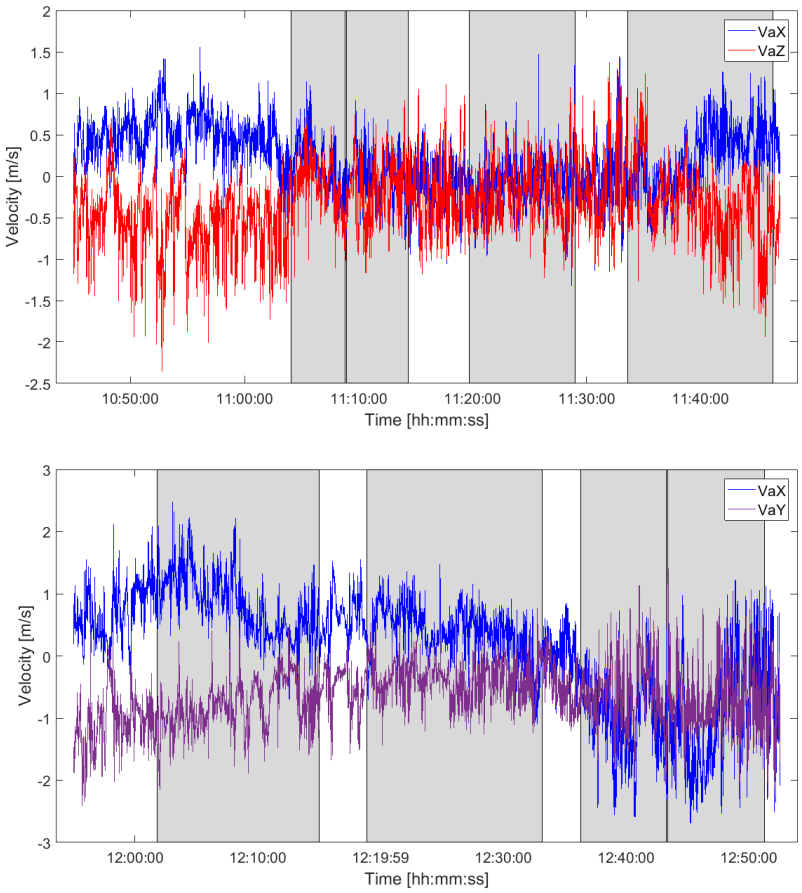

Figure 6.7: Plots of the anemometer measurements between 10:45 and 12:52. The shaded areas correspond to the times when data was collected with the quadrotor. Top: Vertical anemometer setup measuring $v_{\mathrm{a}}^{\mathrm{x}}$ and $v_{\mathrm{a}}^{\mathrm{z}}$, Bottom: Horizontal anemometer setup measuring $v_{\mathrm{a}}^{\mathrm{x}}$ and $v_{\mathrm{a}}^{\mathrm{y}}$.

One indication for the quadrotor's downwash affecting the vertical measurements at the ski jump can be found in figure 6.7, which shows the wind velocities measured by the anemometer over the period of all six conducted test flights at the ski jump in April. The times when data was collected with the quadrotor are marked with the grey shading. The top image shows the $x-$ and $z-$velocities measured by the first anemometer configuration, while the bottom image shows the measurements of the second, horizontal anemometer configuration measuring $x-$ and $y-$velocities. When looking at the top image, which shows the wind speeds measured by the anemometer continuously from 10:45 to 11:45, a considerable change in both vertical and horizontal wind speed is seen at 11:04, which is when the quadrotor starts hovering close to the anemometer. The horizontal wind speed is shifted towards lower values, i.e. stronger wind from north, while the vertical wind speed is shifted towards higher values, i.e. stronger downwards wind. This is what would be expected if the downwash does indeed affect the anemometer's measurements. However, the wind speed only increased by about 0.5 m/s which is not enough to explain the offsets of up to 4 m/s found between the vertical estimate and the measurements in figure 5.2. Thus, the downwash might have affected the results, especially since the quadrotor was positioned east or south of the anemometer, which would have been in front of the anemometer relative to the wind direction for some of the flights, but it is not the main cause of the deviations.

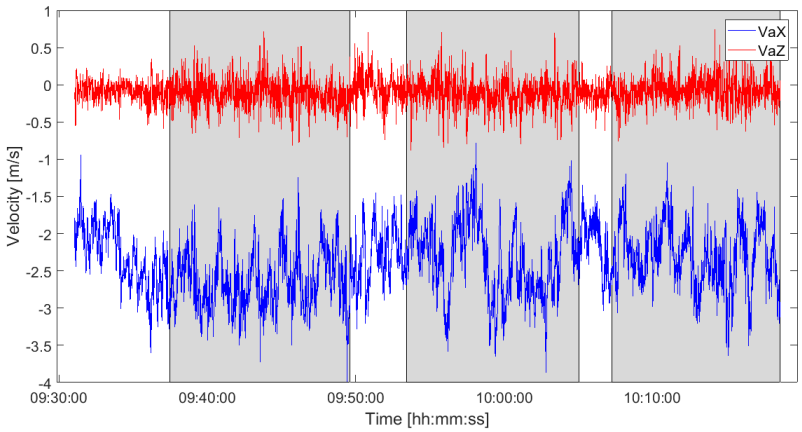

Figure 6.8: Measurements of the vertically measuring anemometer at Ramfjordmoen between 09:30 and 10:18 on 27.04.2018. The shaded areas indicate the times data was collected with the quadrotor.

A similar plot of the anemometer measurements gathered during the test flights at Ramfjordmoen is shown in figure 6.8 for the first three test flights during which the anemometer was measuring vertically. Here, the vertical component does not change between the shaded and non-shaded areas, sug-

gesting no disturbance of the measurements by the quadrotor downwash. This observation matches the fact that care was taken to place the quadrotor either next to or behind the anemometer as seen by the wind, but never in front of it (see figure 6.6).

6.3.3 Accuracy of Altitude Hold

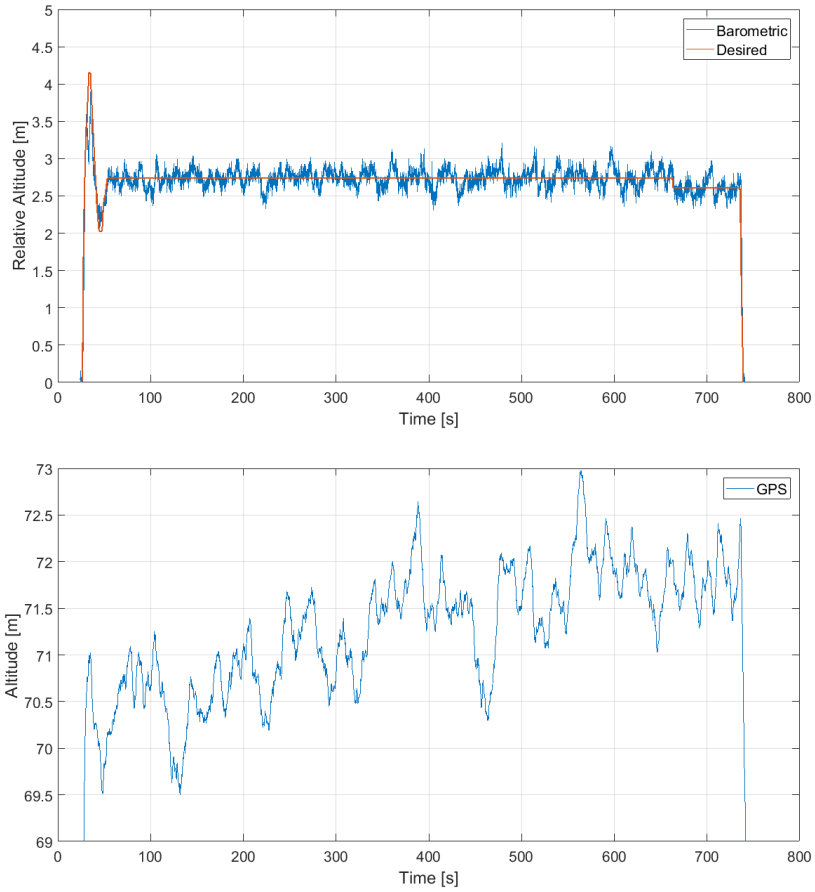

Figure 6.9: Altitude measured by the quadrotor during flight 3 in Ramfjordmoen. Top: Barometric and desired relative altitude, Bottom: GPS altitude

This leaves the question of what causes the wind estimates to deviate so much from the measurements. The most likely reason is the uncertainty in the altitude measurements of the quadrotor. When the quadrotor was holding its position in Loiter mode, variations in its position could be observed. Horizontally, these variations were limited to about 0.5 m with only a few larger displacements from stronger wind gusts. Vertically however, the quadrotor was observed to be rising or falling slowly at times with the over-

all variation of altitude being up to 3 m. The reason for this can be found in figure 6.9 which exemplifies the altitudes measured by the barometer and GPS of the quadrotor for flight 3 in Ramfjordmoen. As explained in section 2.2.6, the quadrotor keeps its altitude based on barometric pressure. Thus if the pressure changes, the quadrotor will rise or fall accordingly. The top image in figure 6.9 shows the desired relative altitude, which the quadrotor is trying to hold, as well as the relative altitude established by the barometer. It can be seen that the barometric altitude varies about the desired value by ± 0.3 m. This is a result of the 10 cm resolution of the barometer [40] and the finite response time of the quadrotor. The altitude measured by the GPS (bottom image) shows a much larger variation between 69.5 - 73 m which agrees with the observations made during the flights.

Since the method is based on the quadrotor holding its position and counteracting the influence of the wind, these large variations in altitude make the method very unreliable in the vertical direction. Improvements could be made by using a different and more accurate method of determining and holding the quadrotor's altitude.

A further disturbance can come from vibrations which can cause the quadrotor to move up or down. A reason for this could be badly balanced propellers.

6.4 Horizontally Measuring Anemometer

From figure 5.1, 5.2 and 5.5, which show the results from the test flights with the horizontally measuring anemometer, quite good agreements can be seen. As discussed in section 6.2, the quadrotor estimates from the April flights at the ski jump have a larger discrepancy due to unfortunate wind conditions. However, a correlation of the overall shape of the measurements can still be seen. The estimates and measurements from the February flights at the ski jump agree very well, though they might still have some influence of the wind conditions being slightly different at the two measurement sites. The flights at Ramfjordmoen, where the most laminar flow and thus almost identical wind conditions at the quadrotor and anemometer site were expected, show the best results.

Figure 6.10 shows the results of the last two test flights conducted in Ramfjordmoen after a 10 s moving average filter (MAF) was applied to the data. Table 6.1 contains the root mean square errors (RMSEs) found for the $x-$ and $y-$components of both flights. They were determined for the results, as they are shown in chapter 5, where the data was averaged into bins of 0.5 s as well as for the 10 s MAF as seen in figure 6.10. The larger values of between 0.45 m/s and 0.55 m/s found from the former can be a result of noise and slight time deviations between the estimate and the measure-

ments. The RMSE values based on the 10 s average lie between 0.23 m/s and 0.30 m/s. These are very good values compared to the ones achieved in the works presented in chapter 3.

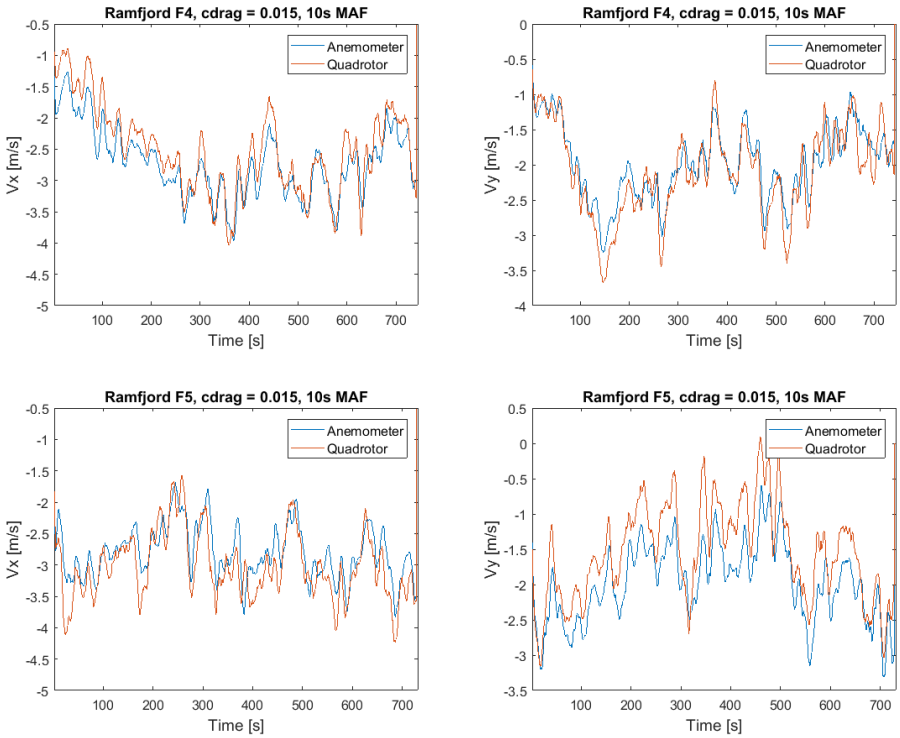

Figure 6.10: Results from flights 4 and 5 conducted in Ramfjordmoen with a 10 s MAF applied to the data.

Table 6.1: RMSE values of the wind estimates for flights 4 and 5 conducted in Ramfjordmoen given in m/s

	0.5 s average		10 s MAF	
Flight	$x-$dir.	$y-$dir.	$x-$dir.	$y-$dir.
Ramfj. F4	0.45	0.50	0.23	0.24
Ramfj. F5	0.58	0.55	0.30	0.28

Table 6.2: RMSE values of the wind estimates for flights 4 and 5 conducted in Ramfjordmoen expressed for wind speed and wind direction.

	0.5 s average		10 s MAF	
Flight	Speed [m/s]	Direction [°]	Speed [m/s]	Direction [°]
Ramfj. F4	0.49	8.9	0.26	4.1
Ramfj. F5	0.56	10.6	0.29	4.9

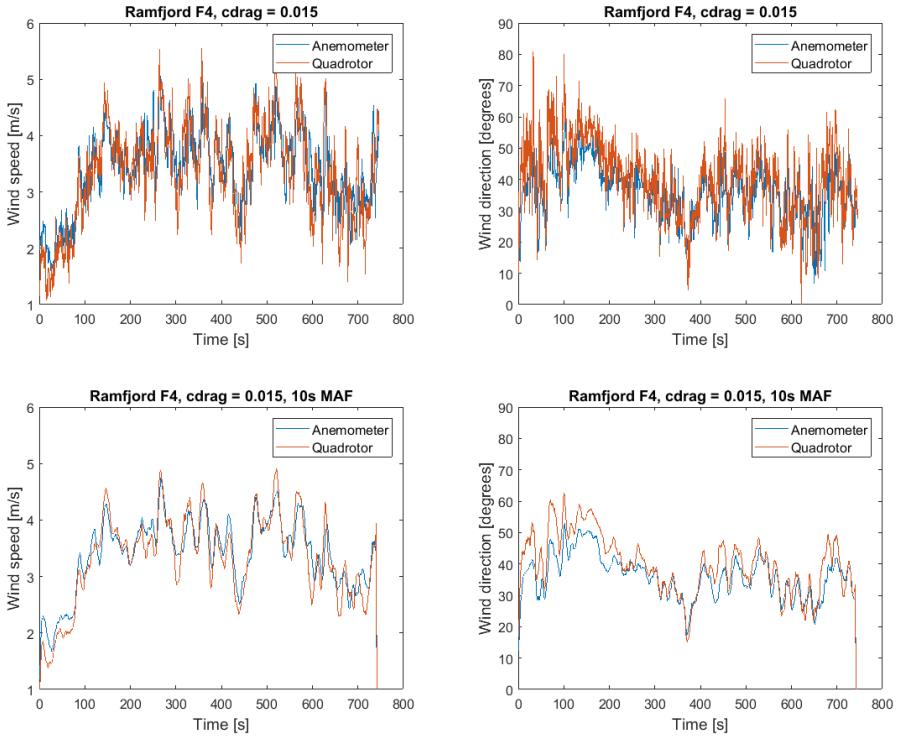

Figure 6.11: Results from flight 4 conducted in Ramfjordmoen transformed to polar form. Top: Data binned in 0.5 s intervals, Bottom: Data treated with a 10 s MAF.

Table 6.3: RMSE values of the wind estimates expressed for wind speed and wind direction compared to results from the literature [32, 35].

	Speed [m/s]	Direction [°]	Data averaging
This thesis	0.26 - 0.29	4.1 - 4.9	10 s MAF
Neumann, Bartholmai	0.36 - 0.60	14.0 - 14.8	20 s MAF
Palomaki	0.3 - 0.9	10 - 21	

For an easier comparison, table 6.2 contains the RMSE values of the same flights expressed in polar form while figure 6.11 shows the wind estimates and measurements in polar form for flight 4 in Ramfjordmoen. Again, the RMSE values for the data averaged in 0.5 s bins are larger than the values calculated after the application of the 10 s MAF. The RMSE value for wind speed lies between 0.49 - 0.56 m/s for the binned data and between 0.26 - 0.29 m/s for the 10 s average. The values for wind direction lie between 8.9 - 10.6° for the binned data and between 4.1 - 4.9° for the 10 s average. The RMSE values found by Neumann and Bartholmai [32] and Palomaki et. al. [35] are listed in table 6.3 together with the RMSE values from this thesis. Both works experienced comparable wind speeds between 0 - 5 m/s during

their test flights. The estimates found in this thesis from flights 4 and 5 in Ramfjordmoen achieve the best RMSE values for both wind speed and direction compared to the two other works. This proves the applicability of this method for horizontal wind velocities.

6.5 Other Sources of Error

This section introduces some further sources of error in the estimated wind velocities. Their influence is small, compared to the previously discussed points.

6.5.1 Angular Orientation of the Anemometer

The accuracy of the angular orientation of the anemometer is limited by the accuracy of a compass or map used to install the device as well as some human error. As discussed in section 6.1, the error in the anemometer angle is assumed to be $\pm 5°$ which can lead to an error in wind speeds in the $x-$ and $y-$direction of up to 0.4 m/s. For the flights in Ramfjordmoen, it was easier to set up the anemometer accurately and a smaller error of $\pm 3°$ can be assumed.

6.5.2 GPS Uncertainties

As described in section 2.2.6, coordinates found via GPS have some uncertainties. This means that some of the corrections the drone undertakes while holding its position in Loiter mode, are not related to wind at all but are merely corrections for deviations in the GPS position. With HDOP values of about 1.8 during the test flights, the influence on the measurements should be small.

6.5.3 Response Time of the Quadrotor

A small time delay could be introduced by the finite response time of the quadrotor to external disturbances. However, the error in anemometer time was found to be ± 250 ms in section 4.3.1. The time delay would be smaller than this error and thus not noticeable in the results. However, due to the larger uncertainty in anemometer time, the wind estimates and measurements might be slightly mismatched by up to 250 ms. For practical applications, knowing the exact time of the measurements might not necessarily be needed to be able to get a measure of wind at a certain position.

6.5.4 Deviations Between Quadrotors

The static thrust tests for this project were conducted with a different quadrotor from the one used in flight tests. Although they are the same model, different quadrotors could exert slightly different behaviour causing deviations in the results. More information on this could be gathered from the manufacturer or further static tests could be made with several drones to map the deviations. However, this error is assumed to be very small and a deeper investigation might not be necessary.

6.5.5 Static Thrust Test Results

Another source of error are the results from the static thrust test. The formulas derived for torque and rotational velocity of the propeller could have some error, though they would not effect the results strongly. The current calculations derived from the static thrust test have a larger error, but their influence in the resulting wind velocities is still small. Another, systematic error could be introduced by the use of a mean RCOU value when calculating current. As discussed in section 4.4.5, two of the motors receive generally higher RCOU values than the others based on the orientation of the propellers' rotation. Whether or not this effects the results could be determined by conducting static thrust tests for two motor-propeller systems: one rotating clockwise and one rotating counter-clockwise.

The effect of errors in the results from the static thrust tests on the estimated wind velocity could be mapped by varying each of the parameters one by one and observing the changes in the results.

Chapter 7

Conclusion

7.1 Summary

The developed wind measuring method is based on the theoretical framework for improving quadrotor control by Allibert et. al. [6]. Their proposed estimate for the quadrotor's air velocity is put into a new context by transforming it to the inertial reference system and applying the wind triangle. Parameters for the used quadrotor are found via static thrust tests and the practicability of the theory for the purpose of measuring wind is tested by conducting three sets of test flights at two different sites.

This is a fundamentally different approach from what has been previously proposed for measuring wind with a quadrotor drone in the literature [22, 32, 35]. Compared to those works, the wind estimates presented in this thesis achieve a higher accuracy in the horizontal component. The vertical wind speed is not measured by the works found in the literature.

The horizontal wind estimates prove to be very promising with RMSE values between 0.23 - 0.30 m/s for two test flights with measured wind speeds between 1 - 5 m/s. The corresponding RMSE values for a polar representation lie between 0.26 - 0.29 m/s for wind speed and between 4.1° - 4.9° for wind direction. These values are a result of the data being smoothed with a 10 s moving average filter.

The vertical wind estimates show offsets of up to 4 m/s compared to the anemometer measurements and a lack in correlation. Reasons for this were found in the anemometer causing turbulence when used vertically, the quadrotor's downwash affecting the measurements and mostly, the lacking ability of the quadrotor to hold its altitude accurately.

7.2 Limitations of the Method

The proposed method is limited in its applicability by some practical factors.

- In section 4.1.1, two assumptions were made when developing the set of theoretical equations for this thesis. The parasitic drag from the airframe was neglected and aerodynamic conditions were assumed to be the same for all four rotors. Both of these assumptions are only valid for a slowly moving quadrotor, i.e. low speed relative to the surrounding air. This limits the applicability of the proposed method to low wind speeds of up to about 10 m/s.
- The measurement time is limited by the flight time of the quadrotor. With the IRIS$^+$, about 10 minutes of continuous measurements can be achieved, depending on the flight conditions. The use of a different quadrotor could possibly extend this.
- Regulations for flying a quadrotor have to be followed. In Norway, those are specified in the *regulations concerning aircraft without a pilot on board etc* [19], which are defined by the Civil Aviation Authority. Additionally, the safety of flying a quadrotor at the site of interest has to be considered. Highly turbulent areas should be avoided, as the drone might get unstable. Holding a reasonable distance to buildings or other structures is further advisable.

7.3 Further Work

This thesis proves the potential of the proposed method. By conducting further tests and considering the use of different devices, the accuracy and reliability of the wind estimates could be further improved. The following gives some suggestions for further work.

7.3.1 Conducting Further Flight Tests

Collecting more data by conducting further flight tests, especially in laminar conditions, can help to improve the results. The drag coefficient could be fine tuned. The effect of the quadrotor's orientation on the results could be mapped by taking several test flights in similar conditions with various quadrotor heading angles. Furthermore, tests could be conducted with different conditions in terms of wind strength to map the method's accuracy in different regions of wind speed.

7.3.2 Using a 3D Anemometer

Disturbances in the anemometer measurements when measuring vertically were attributed to the unsuitability of the used WindSonic for measuring vertical wind. Thus, higher accuracy and a better understanding of the results could be gained from the use of an anemometer that can measure wind simultaneously in three dimensions.

7.3.3 Using a Different Quadrotor

Some of the deviations between the estimates and the measurements can be tracked back to the quadrotor model and how it behaves in the air. The IRIS$^+$ lacks a direct measure of motor current which had to be modelled empirically from voltage and RCOU values. Furthermore, the position held in Loiter mode is lacking accuracy, especially in the vertical direction, due to the use of a barometer. This can also be influenced by a high level of vibration in the quadrotor.

Considering the use of a different quadrotor might eliminate some of those problems. Alternatively, the quadrotor software could be reprogrammed to implement a more accurate method of holding the quadrotor's position.

7.3.4 Mapping Errors From Static Thrust Test

The parameters found from the static thrust test, which are used in the calculation of the wind estimate, can contain some errors. The effect of these on the estimated wind velocity could be mapped by varying each of the found parameters one by one and observing the changes in the results.

The model for calculating motor current could be improved by taking measurements for a larger amount of different voltage values. Additionally, conducting a second static thrust test with an oppositely rotating motor could verify the use of a mean RCOU value for the current calculation or give reason for modifying the model.

7.3.5 Other Possibilities

- Considering alternatives to GPS for measuring the quadrotor's position and ground velocity.
- Modifying the MatLab code to improve its user-friendliness.
- Once the measurement system is established reliably, the effect of adding a payload could be investigated.

Appendix

MatLab Files

MRDataCutMean4.m

```
function Flight = MRdataCutMean4(filename,t0,tstart...
    ,tend, plots)
% calculates mean values for given time-period + creates
% plots + returns time cut vectors
%
% AUTHOR + VERSION:
%   Magdalena Simma
%   Version 4 25.09.2017
%
% INPUT:
%   filename - name of file to load
%   FlightName - name of returned structure
%   t0 - time indicating start of new time vector  [in mikrosec]
%   tstart - starting time [in mikrosec] data is cut to
%   tend - ending time [in mikrosec] data is cut to
%   plots - to turn plots on/off [1/0] - default = 0
%
% OUTPUT:
%   Flight: Structure containing:
%   GPS:    GPS.time, GPS.lat, GPS.long, GPS.alt,
%           GPS.speed, GPS.grcourse, GPS.vz
%   ATT:    ATT.time, ATT.roll, ATT.pitch, ATT.yaw
%   IMU:    IMU.time, IMU.gyrX, IMU.gyrY, IMU.gyrZ, IMU.accX,
%           IMU.accY, IMU.accZ
%   IMU2:   IMU2.time, IMU2.gyrX, IMU2.gyrY, IMU2.gyrZ,
%           IMU2.accX, IMU2.accY, IMU2.accZ
%   RCOU:   RCOU.time, RCOU.C1, RCOU.C2, RCOU.C3, RCOU.C4
%   CURR:   CURR.time, CURR.Volt, CURR.Curr
%   CTUN:   CTUN.ALT, CTUN.BAlt, CTUN.CRt
%
%   MEAN:   Structure containing mean values for all
%           previously mentioned parameters
%
```

```
% EXAMPLE:
%   filename = '2018-02-13 11-15-25.log-161762.mat'; %data
%   t0 = 293807; %defines start point for new time vectors [ms]
%   tstart = 0;         %starttime measured from t0 [ms]
%                       %(i.e. 93e3 = 93 s after t0)
%   tend = 822346 - t0; %endtime measured from t0 [ms]
%   plots = 1;          %to turn plots on/off [1/0]
%
%   Flight1 = MRdataCutMean4(filename,t0,tstart,tend,plots);
%
%-------------------------------------------------

load (filename);

% defaulting plots parameter
if ~exist('plots','var')
% plots parameter does not exist, so default it to something
plots = 0; %turns off plots
end

%-------------------------------------------------------
%% GPS

GPS_time = GPS(:,14) - tot; %airtime

t1 = find(GPS_time > tstart,1); %find starting time index
t2 = find(GPS_time > tend,1);   %find end time index

Flight.GPS.time = GPS(t1:t2,14) - tot; %cut time vector

%cut other GPS data vectors
Flight.GPS.lat = GPS(t1:t2,7); %Latitude from GPS
Flight.GPS.long = GPS(t1:t2,8); %Longitude from GPS
Flight.GPS.alt = GPS(t1:t2,10); % Altitude from GPS
Flight.GPS.grspeed = GPS(t1:t2,11); %Ground speed
Flight.GPS.grcourse = GPS(t1:t2,12); %Ground course
Flight.GPS.vz = GPS(t1:t2,13); %Vertical velocity

%calculate means:
Flight.MEAN.GPS.lat = mean(Flight.GPS.lat);
Flight.MEAN.GPS.long = mean(Flight.GPS.long);
Flight.MEAN.GPS.alt = mean(Flight.GPS.alt);
Flight.MEAN.GPS.grspeed = mean(Flight.GPS.grspeed);
Flight.MEAN.GPS.grcourse = mean(Flight.GPS.grcourse);
Flight.MEAN.GPS.vz = mean(Flight.GPS.vz);

if plots ==1
%plotting longitude/latitude
figure
plot(Flight.GPS.long,Flight.GPS.lat);
ylabel('latitude');
xlabel('longitude');
title('Flight path');

```

```
88  %plotting altitude
89  figure
90  plot(Flight.GPS.time,Flight.GPS.alt);
91  title('Altitude')
92  xlabel('time [ms]');
93  ylabel('altitude [m]');
94  grid on
95  hold on
96  else
97  end
98
99  %-------------------------------------------------------
100 %% ATT - Roll, Pitch, Yaw
101
102 ATT_time = ATT(:,2) - tot; %airtime
103 t1 = find(ATT_time > tstart,1); %find starting time index
104 t2 = find(ATT_time > tend,1);   %find end time index
105
106 Flight.ATT.time = ATT(t1:t2,2) - tot; %cut time vector
107
108 %cut other ATT data vectors
109 Flight.ATT.roll = ATT(t1:t2,4);
110 Flight.ATT.pitch = ATT(t1:t2,6);
111 Flight.ATT.yaw = ATT(t1:t2,8);
112
113 %calculating means
114 Flight.MEAN.ATT.roll = mean(Flight.ATT.roll);
115 Flight.MEAN.ATT.pitch = mean(Flight.ATT.pitch);
116 Flight.MEAN.ATT.yaw = mean(Flight.ATT.yaw);
117
118 if plots ==1
119 %plotting
120 figure
121 plot(Flight.ATT.time,Flight.ATT.pitch);
122 hold on
123 plot(Flight.ATT.time,Flight.ATT.roll,'r');
124 plot(Flight.ATT.time,Flight.ATT.yaw,'g');
125 title('Roll, Pitch, Yaw');
126 xlabel('time [ms]');
127 ylabel('angle');
128 legend('Pitch','Roll','Yaw');
129 grid on
130 else
131 end
132
133 %-------------------------------------------------------
134 %% IMU - Gyroscope, Accelerometer
135
136 IMU_time = IMU(:,2) - tot; %airtime
137 t1 = find(IMU_time > tstart,1); %find starting time index
138 t2 = find(IMU_time > tend,1);   %find end time index
139
140 Flight.IMU.time = IMU(t1:t2,2) - tot; %cut time vector
141
```

```
142 %cut other IMU data vectors
143 Flight.IMU.gyrX = IMU(t1:t2,3); %gyroscope
144 Flight.IMU.gyrY = IMU(t1:t2,4);
145 Flight.IMU.gyrZ = IMU(t1:t2,5);
146 Flight.IMU.accX = IMU(t1:t2,6); %accelerometer
147 Flight.IMU.accY = IMU(t1:t2,7);
148 Flight.IMU.accZ = IMU(t1:t2,8);
149
150 %calculating means
151 Flight.MEAN.IMU.gyrX = mean(Flight.IMU.gyrX);
152 Flight.MEAN.IMU.gyrY = mean(Flight.IMU.gyrY);
153 Flight.MEAN.IMU.gyrZ = mean(Flight.IMU.gyrZ);
154 Flight.MEAN.IMU.accX = mean(Flight.IMU.accX);
155 Flight.MEAN.IMU.accY = mean(Flight.IMU.accY);
156 Flight.MEAN.IMU.accZ = mean(Flight.IMU.accZ);
157
158 if plots ==1
159 %plotting
160 figure %Gyroscope
161 plot(Flight.IMU.time,Flight.IMU.gyrX);
162 hold on
163 plot(Flight.IMU.time,Flight.IMU.gyrY);
164 plot(Flight.IMU.time,Flight.IMU.gyrZ);
165 title('Gyroscopes');
166 xlabel('time [ms]');
167 legend('GyrX','GyrY','GyrZ');
168 grid on
169
170 figure %Accelerometer
171 plot(Flight.IMU.time,Flight.IMU.accX);
172 hold on
173 plot(Flight.IMU.time,Flight.IMU.accY);
174 plot(Flight.IMU.time,Flight.IMU.accZ);
175 title('Accelerometer');
176 xlabel('time [ms]');
177 legend('AccX','AccY','AccZ');
178 grid on
179 else
180 end
181
182 %-------------------------------------------------------
183 %% IMU2 - Gyroscope, Accelerometer
184
185 IMU2_time = IMU2(:,2) - tot; %airtime
186 t1 = find(IMU2_time > tstart,1); %find starting time index
187 t2 = find(IMU2_time > tend,1);   %find end time index
188
189 Flight.IMU2.time = IMU2(t1:t2,2) - tot; %cut time vector
190
191 %cut other IMU data vectors
192 Flight.IMU2.gyrX = IMU2(t1:t2,3); %gyroscope
193 Flight.IMU2.gyrY = IMU2(t1:t2,4);
194 Flight.IMU2.gyrZ = IMU2(t1:t2,5);
195 Flight.IMU2.accX = IMU2(t1:t2,6); %accelerometer
```

```
196 Flight.IMU2.accY = IMU2(t1:t2,7);
197 Flight.IMU2.accZ = IMU2(t1:t2,8);
198
199 %calculating means
200 Flight.MEAN.IMU2.gyrX = mean(Flight.IMU2.gyrX);
201 Flight.MEAN.IMU2.gyrY = mean(Flight.IMU2.gyrY);
202 Flight.MEAN.IMU2.gyrZ = mean(Flight.IMU2.gyrZ);
203 Flight.MEAN.IMU2.accX = mean(Flight.IMU2.accX);
204 Flight.MEAN.IMU2.accY = mean(Flight.IMU2.accY);
205 Flight.MEAN.IMU2.accZ = mean(Flight.IMU2.accZ);
206
207 if plots ==1
208 %plotting
209 figure %Gyroscope
210 plot(Flight.IMU2.time,Flight.IMU2.gyrX);
211 hold on
212 plot(Flight.IMU2.time,Flight.IMU2.gyrY);
213 plot(Flight.IMU2.time,Flight.IMU2.gyrZ);
214 title('Gyroscopes IMU2');
215 xlabel('time [ms]');
216 legend('GyrX','GyrY','GyrZ');
217 grid on
218
219 figure %Accelerometer
220 plot(Flight.IMU2.time,Flight.IMU2.accX);
221 hold on
222 plot(Flight.IMU2.time,Flight.IMU2.accY);
223 plot(Flight.IMU2.time,Flight.IMU2.accZ);
224 title('Accelerometer IMU2');
225 xlabel('time [ms]');
226 legend('AccX','AccY','AccZ');
227 grid on
228 else
229 end
230
231 %------------------------------------------------------
232 %% RCOU - hvor mye power hver motor yter
233
234 RCOU_time = RCOU(:,2) - tot;
235 t1 = find(RCOU_time > tstart,1); %find starting time index
236 t2 = find(RCOU_time > tend,1);   %find end time index
237
238 Flight.RCOU.time = RCOU(t1:t2,2) - tot; %cut time vector
239
240 %cut other RCOU data vectors
241 Flight.RCOU.C1 = RCOU(t1:t2,3);
242 Flight.RCOU.C2 = RCOU(t1:t2,4);
243 Flight.RCOU.C3 = RCOU(t1:t2,5);
244 Flight.RCOU.C4 = RCOU(t1:t2,6);
245
246 %calculating means
247 Flight.MEAN.RCOU.C1 = mean(Flight.RCOU.C1);
248 Flight.MEAN.RCOU.C2 = mean(Flight.RCOU.C2);
249 Flight.MEAN.RCOU.C3 = mean(Flight.RCOU.C3);
```

```
250 Flight.MEAN.RCOU.C4 = mean(Flight.RCOU.C4);
251
252 if plots == 1
253 %plotting the power of the four motors
254 figure
255 plot(Flight.RCOU.time,Flight.RCOU.C1);
256 hold on
257 plot(Flight.RCOU.time,Flight.RCOU.C2,'r');
258 plot(Flight.RCOU.time,Flight.RCOU.C3,'g');
259 plot(Flight.RCOU.time,Flight.RCOU.C4,'y');
260 title('RCOU of the four motors');
261 xlabel('time [ms]');
262 ylabel('RCOU');
263 legend('C1','C2','C3','C4');
264 grid on
265 else
266 end
267
268 %-------------------------------------------------------
269 %% CURR - Voltage, Current
270
271 CURR_time = CURR(:,2) - tot;
272 t1 = find(CURR_time > tstart,1); %find starting time index
273 t2 = find(CURR_time > tend,1);   %find end time index
274
275 Flight.CURR.time = CURR(t1:t2,2) - tot; %cut time vector
276
277 %cut other CURR data vectors
278 Flight.CURR.volt = CURR(t1:t2,5)/100; %Battery voltage in V
279     %[given as V*100 in log]
280 Flight.CURR.curr = CURR(t1:t2,6)/100; %Current drawn from the
281     %Battery in Amp [given as A*100 in log]
282
283 %calculating means
284 Flight.MEAN.CURR.volt = mean(Flight.CURR.volt);
285 Flight.MEAN.CURR.curr = mean(Flight.CURR.curr);
286
287 if plots == 1
288 %plotting
289 figure
290 plot(Flight.CURR.time,Flight.CURR.volt);
291 hold on
292 plot(Flight.CURR.time,Flight.CURR.curr);
293 title('Voltage, Current');
294 legend('Battery Voltage','Current drawn from Battery');
295 xlabel('time [mikro s]');
296 ylabel('V/A');
297 grid on
298 else
299 end
300
301 %-------------------------------------------------------
302 %% CTUN - Altitude
303
```

```
304 CTUN_time = CTUN(:,2) - tot;
305 t1 = find(CTUN_time > tstart,1); %find starting time index
306 t2 = find(CTUN_time > tend,1);   %find end time index
307
308 Flight.CTUN.time = CTUN(t1:t2,2) - tot; %cut time vector
309
310 %cut other CTUN data vectors
311 Flight.CTUN.alt = CTUN(t1:t2,7); % Altitude
312 Flight.CTUN.BAlt = CTUN(t1:t2,8); %Barometric altitude
313 Flight.CTUN.CRt = CTUN(t1:t2,12); %Climb rate
314
315 %calculating means
316 Flight.MEAN.CTUN.alt = mean(Flight.CTUN.alt);
317 Flight.MEAN.CTUN.BAlt = mean(Flight.CTUN.BAlt);
318 Flight.MEAN.CTUN.CRt = mean(Flight.CTUN.CRt);
319
320 if plots == 1
321 %plotting
322 figure
323 plot(Flight.CTUN.time,Flight.CTUN.alt);
324 hold on
325 plot(Flight.GPS.time,Flight.GPS.alt);
326 plot(Flight.CTUN.time,Flight.CTUN.BAlt);
327 legend('CTUN Alt','GPS Alt','CTUN BAlt');
328 xlabel('time');
329 ylabel('m');
330 title('Altitude');
331 grid on
332 else
333 end
334
335 end
```

CalcWind_from_Drone.m

```
function CalcWind_from_Drone(F,FlightName,cdrag)
%Calculates wind velocity from drone data
%
% AUTHOR + VERSION:
%   Magdalena Simma
%   Version 1 10.05.2018
%
% INPUT:
%   F - Flight data stored in structure array
%   FlightName - string containing name of the flight
%                (for plot titles)
%   cdrag - lumped drag coefficient
%
% OUTPUT:
%   Comparison plots between estimated and measured wind
%   velocity
%
% EXAMPLE:
%   load('FlightDataRamfjord.mat');
%
%   F = April_Flight4;
%   FlightName = 'Flight 4';
%   cdrag = 0.015;
%
%   CalcWind_from_Drone(4,FlightName,cdrag);
%-------------------------------------------------------------------------

run('InterpolatingVoltage.m');
run('CalcBin.m');
run('Parameters.m');
run('Variables.m');
run('CalcVehicleAirSpeed.m');

end
```

InterpolatingVoltage.m

```
%% Interpolating CURR datagroup (volt)
% Interpolates voltage
%
% AUTHOR + VERSION:
%   Magdalena Simma
%   Version 1 10.05.2018
%_____________________________

% original variables to interpolate
x = F.CURR.time;
v = F.CURR.volt;

% creating new time vector
xq = zeros(10*(length(x)-1)+1,1);
xq(1) = x(1);
for j = 1:length(x)-1
xq(10*j-9) = x(j) + (x(j+1)-x(j))/10;
xq(10*j-8) = x(j) + 1*(x(j+1)-x(j))/10;
xq(10*j-7) = x(j) + 2*(x(j+1)-x(j))/10;
xq(10*j-6) = x(j) + 3*(x(j+1)-x(j))/10;
xq(10*j-5) = x(j) + 4*(x(j+1)-x(j))/10;
xq(10*j-4) = x(j) + 5*(x(j+1)-x(j))/10;
xq(10*j-3) = x(j) + 6*(x(j+1)-x(j))/10;
xq(10*j-2) = x(j) + 7*(x(j+1)-x(j))/10;
xq(10*j-1) = x(j) + 8*(x(j+1)-x(j))/10;
xq(10*j) = x(j) + 9*(x(j+1)-x(j))/10;
xq(10*j+1) = x(j+1);
end
clear j

% Interpolation
VoltInterp = interp1(x,v,xq,'nearest');

plots = 0; % to turn plots on/off [1/0]
if plots ==1
figure
plot(x,v,'x')
hold on
plot(xq,VoltInterp,':.')
legend('data','interpolated')
xlabel('time')
ylabel('volt')
else
end

clear x v
```

CalcBin.m

```
%% Creating binned vectors
% because different data is not stored at the exact
% same points in time
%
% AUTHOR + VERSION:
%   Magdalena Simma
%   Version 1 10.05.2018
%————————————————————————

maxtime = F.GPS.time(end); %[millisec] — time vector
binsize = 0.5e3; %[millisec] — time intervals to average over
plots = 0; % turns plots on/off [1/0]

%Acceleration
[binAccX,binTime] = CreateTimeBinnedVectors(...
    maxtime,binsize,F.IMU.time,F.IMU.accX,plots); %accX
binAccY = CreateTimeBinnedVectors(...
    maxtime,binsize,F.IMU.time,F.IMU.accY,plots); %accY
binAccZ = CreateTimeBinnedVectors(maxtime,...
    binsize,F.IMU.time,F.IMU.accZ,plots); %accZ

%Roll,Pitch,Yaw
binPitch = CreateTimeBinnedVectors(maxtime...
    ,binsize,F.ATT.time,F.ATT.pitch,plots); %pitch
binRoll = CreateTimeBinnedVectors(maxtime...
    ,binsize,F.ATT.time,F.ATT.roll,plots); %roll
binYaw = CreateTimeBinnedVectors(maxtime...
    ,binsize,F.ATT.time,F.ATT.yaw,plots); %yaw

%Voltage
binVolt = CreateTimeBinnedVectors(maxtime...
    ,binsize,xq,VoltInterp,plots); %volt

%RCOU
binRCOU(:,1) = CreateTimeBinnedVectors(maxtime...
    ,binsize,F.RCOU.time,F.RCOU.C1,plots); %RCOU1
binRCOU(:,2) = CreateTimeBinnedVectors(maxtime...
    ,binsize,F.RCOU.time,F.RCOU.C2,plots); %RCOU2
binRCOU(:,3) = CreateTimeBinnedVectors(maxtime...
    ,binsize,F.RCOU.time,F.RCOU.C3,plots); %RCOU3
binRCOU(:,4) = CreateTimeBinnedVectors(maxtime...
    ,binsize,F.RCOU.time,F.RCOU.C4,plots); %RCOU4
```

CreateTimeBinnedVectors.m

```
function [binnedX,binTime] = CreateTimeBinnedVectors(...
    maxtime,binsize,time,X,plots)
% Creates equally spaced time-bins and returns an
% average function value for each bin. Returns a vector
%
% AUTHOR + VERSION:
%   Magdalena Simma
%   Version 1 28.09.2017
%
% INPUT:
%   maxtime - time-bins will be created from t=0s until
%       t=maxtime [millisec.]
%   binsize - [millisec.]
%   time - original time vector [millisec.]
%   X - vector of function values to be binned
%   plots - to turn plots on/off [1/0] - optional (default = 0)
%
% OUTPUT:
%   binTime - vector containing binned time values
%       (upper edges of bins) [millisec]
%   binnedX - vector of binned function values [same unit as X]
%
% EXAMPLE:
%     maxtime = 900e6; %[millisec]
%     binsize = 0.5e6; %[millisec]
%     plots = 0;
%     X = Flight2.IMU.accX;
%     time = Flight2.IMU.time;
%
%     [binnedAccX,binTime] = CreateTimeBinnedVectors(...
            maxtime,binsize,time,X,plots);

if ~exist('plots','var')
% plots parameter does not exist, so default it to something
plots = 0;
end

edges = 0:binsize:maxtime;

[~,~,bin] = histcounts(time,edges);

binnedX = zeros(max(bin),1);
for i = 1:max(bin)
index1 = find(bin == i,1,'first');
index2 = find(bin == i,1,'last');
binnedX(i) = mean(X(index1:index2));
end

binNumber = 1:1:max(bin);
binTime = binNumber .* binsize;
```

```
51
52 if plots ==1
53 figure
54 plot(time,X);
55 hold on
56 plot(binTime,binnedX);
57 legend('Input Data','Binned Data')
58 xlabel('time');
59 title(['Binned data - bin size = ',num2str(binsize/1e3),...
60     ' sec.']);
61 else
62 end
63
64 end
```

Parameters.m

```
1  %% Parameters
2  % Defining the parameters for the calculations
3  %
4  % AUTHOR + VERSION:
5  %   Magdalena Simma
6  %   Version 1 10.05.2018
7  %-------------------------------
8
9  % Figure of Merit
10 FOM = 0.6072; %From static thrust test
11
12 % Propeller moment of Inertia I
13 rotSize = 9.5 * 2.54 /100; % [m] rotor size (diameter)
14 rotormass = 0.0135; %[kg] rotor mass,
15     % Source: Håvards measurements
16
17 I = 1/12 * rotormass * rotSize^2; % [kg m^2]
18     % Moment of Inertia of rotor (assuming rotating rod)
19
20 % Total propeller disk area
21 Atot = (rotSize/2)^2 * pi *4; %[m^2]
22     % Total prop disk area of four rotors
23
24 % Air density
25 rho = 1.268; % [kg/m3] air density (+5degrees)
26
27 % Quadrotor mass (inkl. battery and propellers)
28 m = 1.371; %[kg] Source: Håvards measurements
29
30 % Lumped drag coefficient of rotors
31 % cdrag = 0.015; %lumped drag coefficient of rotors
32 % Given as a variable to CalcWind_from_Drone.m instead
```

Variables.m

```
%% Variables
% Calculating the variables needed to solve the set of equations
%
% AUTHOR + VERSION:
%   Magdalena Simma
%   Version 1 10.05.2018
%------------------------------

%% aX,aY,aZ - 3D Accelerometer data

aX = binAccX;
aY = binAccY;
aZ = binAccZ;

% Plotting
if plots ==1
figure
plot(binTime,binAccX);
hold on
plot(binTime,binAccY);
plot(binTime,binAccZ);
title('binned accelerometer data')
legend('aX','aY','aZ')
else
end

clear binAccX binAccY binAccZ

%-------------------------------------------------------
%% i - Motor Current
% Calculating Current from given RCOU, Voltage

% Define input for calculation
RCOUInput = mean(binRCOU,2); %[microsec]
Voltage = binVolt;
clear binRCOU

% Parameters for calculation (Found from static thrust test)
K_k = 0.001531298701177;
K_d = -1.948100260174688;
D_k = -0.004706566328902;
D_d = 5.536162554723229;

% Calculating current
kk = K_k * RCOUInput + K_d; % slope K of Current vs. Voltage
dd = D_k * RCOUInput + D_d; % offset D of Current vs. Voltage

Current = kk .* Voltage + dd; % Calculate Current from Voltage

clear K_k K_d D_k D_d kk dd
```

```
51
52 % Plotting
53 if plots ==1
54 figure
55 plot(Voltage,Current,'x');
56 title('calculated current vs. voltage');
57 xlabel('voltage [V]');
58 ylabel('calculated current [A]')
59
60 figure
61 plot(binTime, Current);
62 title('Calculated current');
63 xlabel('time [ms]');
64 ylabel('calculated current [A]');
65 else
66 end
67
68 %------------------------------------------------------
69 %% torque - Motor torque
70 % Calculating motor torque from electrical power
71
72 elPower = Voltage .* Current;
73 torque = elPower .* 0.000903 + 0.0102;
74 %formula from fit from static thrust test
75
76 % Alternative calculation (as used in paper - Allibert)
77 %   -> not exact enough
78 % Kv = 920; %[rpm/V] motor constant
79 %   % Source: Pilot's operating handbook
80 % Kq = 1/Kv; % torque constant of motor
81 % torque = Kq .* Current;
82
83 %------------------------------------------------------
84 %% omega - Propeller rotational velocity
85 % Calculating omega from electrical power
86
87 omega_rpm = -0.506 .* elPower.^2 + 96.673 .* elPower + 2468.5;
88 %formula from fit from static thrust test
89 omega = omega_rpm .* 2 .* pi ./ 60; % transforming unit to Hz
90
91 clear omega_rpm elPower
92
93 %------------------------------------------------------
94 %% domega - Time derivative of omega
95
96 % Calculating time derivative
97 domega = diff([eps; omega(:)])./diff([eps; binTime(:)]);
98 domega(1) = 0;
99
100 % Plotting
101 if plots ==1
102 figure
103 plot(binTime, domega)
104 xlabel('time')
```

```
105 ylabel('domega')
106 else
107 end
108
109 %————————————————————————————————————————————
110 %% Vx,Vy,Vz — Vehicle's ground velocity
111
112 %Vertical Speed
113 Vz = —F.GPS.vz; % [m/s] vertical speed
114
115 % Calculating Azimuthal Angle in degrees from flight path
116     % (Flight path defined by lat and long)
117 az = zeros(length(F.GPS.time),1); %preallocating azimuthal angle
118 for i = 2:length(F.GPS.time)
119 az(i) = azimuth(F.GPS.lat(i—1),F.GPS.long(i—1),...
120     F.GPS.lat(i),F.GPS.long(i));
121     %calculates azimuthal angle (clockwise from north)
122     %from point (i—1) to point i
123 end
124 az(1) = az(2); %assigning value to first index
125 clear i
126
127 % Calculating Horizontal Speed
128 Vh = F.GPS.grspeed;
129 Vx = Vh .* cosd(az);
130 Vy = Vh .* sind(az);
131 clear Vh az
132
133 % Binning vectors
134 binVx = CreateTimeBinnedVectors(...
135     maxtime,binsize,F.GPS.time,Vx,plots); %Vx
136 binVy = CreateTimeBinnedVectors(...
137     maxtime,binsize,F.GPS.time,Vy,plots); %Vy
138 binVz = CreateTimeBinnedVectors(...
139     maxtime,binsize,F.GPS.time,Vz,plots); %Vz
140
141 clear Vx Vy Vz
```

CalcVehicleAirSpeed.m

```
%% Calculating Wind Speed from Parameters and Variables
%
% AUTHOR + VERSION:
%   Magdalena Simma
%   Version 1 10.05.2018
%------------------------------
%
% Variable names: aX, aY, aZ, I, omega, domega, torque
% Parameter names: m, rho, Atot, cdrag

%-------------------------------------------------------
%% Calculating Vehicle Air Speed VaX,VaY,VaZ
% Solving the set of equations

T =  - m .* aZ; %Thrust force

VaX = + aX ./ aZ ./ cdrag; %vehicle air speed in x-dir in BFF
VaY = + aY ./ aZ ./ cdrag; %vehicle air speed in y-dir in BFF

P_H = - m ./ aZ ./ cdrag .* (aX.^2 + aY.^2);
P_r = I .* omega .* domega;
P_m = torque .* omega;
P_T = (P_m - P_r) .* FOM - P_H;

Vind_minus_VaZ = P_T ./ T;

U = sqrt( VaX.^2 + VaY.^2 + Vind_minus_VaZ.^2 );

Vind = T ./ (8 .* rho .* Atot .* U);

VaZ = Vind - P_T ./ T;

clear T P_H P_r P_m P_T Vind_minus_VaZ U Vind

%-------------------------------------------------------
%% Transferring velocities to vehicle frame

% Defining rotational matrix from BFF to VF
% line 1 entries
AA = cosd(binPitch).*cosd(binYaw);
BB = sind(binRoll).*sind(binPitch).*cosd(binYaw)...
    -cosd(binRoll).*sind(binYaw);
CC = cosd(binRoll).*sind(binPitch).*cosd(binYaw)...
    +sind(binRoll).*sind(binYaw);
% line 2 entries
DD = cosd(binRoll).*sind(binYaw);
EE = sind(binRoll).*sind(binPitch).*sind(binYaw)...
    +cosd(binRoll).*cosd(binYaw);
FF = cosd(binRoll).*sind(binPitch).*sind(binYaw)...
    -sind(binRoll).*cosd(binYaw);
```

```
% line 3 entries
GG = - sind(binPitch);
HH = sind(binRoll).*cosd(binPitch);
II = cosd(binRoll).*cosd(binPitch);

VaX_I = AA.*VaX + BB.*VaY + CC.*VaZ;

VaY_I = DD .* VaX + EE .* VaY + FF .* VaZ;

VaZ_I = GG.* VaX + HH .* VaY + II .* VaZ;

clear AA BB CC DD EE FF GG HH II

%-------------------------------------------------------------
%% Plotting a comparison BFF vs. VF

if plots ==1
figure
plot(binTime,VaX,binTime,VaY,binTime,VaZ)
hold on
plot(binTime,VaX_I,binTime,VaY_I,binTime,VaZ_I)
title('Comparison air velocity BFF vs. VF')
xlabel('time [ms]')
ylabel('velocity [m/s]')
legend('VaX','VaY','VaZ','VaX_I','VaY_I','VaZ_I')
else
end

%-------------------------------------------------------------
%% Wind Triangle

VwX = binVx - VaX_I; % calculated wind speed
VwY = binVy - VaY_I;
VwZ = binVz - VaZ_I;

%-------------------------------------------------------------
%% Plotting comparison Va vs. Vw

if plots ==1
figure
plot(binTime,VaX_I,binTime,VaY_I,binTime,VaZ_I)
hold on
plot(binTime,VwX,binTime,VwY,binTime,VwZ)
title('Comparison air velocity (IRF) vs. wind velocity')
xlabel('time [ms]')
ylabel('velocity [m/s]')
legend('VaX','VaY','VaZ','VwX','VwY','VwZ')
else
end

%-------------------------------------------------------------
%% Wind velocities from anemometer

ampl = F.Anem.ampl; % wind speed
```

```
105 angle = F.Anem.angle; % wind direction
106 time = F.Anem.time; % time
107
108 % Negative signs because Wind from North is Odeg,
109     % Wind from South is 180deg
110 VanemX = - ampl .* cosd(angle);
111 VanemY = - ampl .* sind(angle);
112
113 %-------------------------------------------------------
114 %% Binned wind velocities from Anemometer
115 %   not needed for plotting but for calculating RMSE values
116
117 binVanemX = CreateTimeBinnedVectors(...
118     maxtime,binsize,time,VanemX,plots); %VanemX
119 binVanemY = CreateTimeBinnedVectors(...
120     maxtime,binsize,time,VanemY,plots); %VanemY
121
122 %-------------------------------------------------------
123 %% Plotting wind velocity from drone vs. anemometer
124
125 % x-direction
126 figure
127 plot((F.Anem.time/1000),VanemX)
128 hold on
129 plot(binTime/1000,VwX)
130 title([FlightName,' cdrag = ',num2str(cdrag)],'FontSize',14)
131 xlim([2 inf])
132 xt = get(gca, 'XTick');
133 set(gca, 'FontSize', 12)
134 ylim([-5 -0.5]);
135 xlabel('Time [s]','FontSize',14)
136 ylabel('Vx [m/s]','FontSize',14)
137 legend({'Anemometer','Quadrotor'},'FontSize',12)
138
139 % y-direction
140 figure
141 plot((F.Anem.time/1000),VanemY)
142 hold on
143 plot(binTime/1000,VwY)
144 xlim([2 inf])
145 title([FlightName,' cdrag = ',num2str(cdrag)],'FontSize',14)
146 xt = get(gca, 'XTick');
147 set(gca, 'FontSize', 12)
148 xlabel('Time [s]','FontSize',14)
149 ylabel('Vy [m/s]','FontSize',14)
150 legend({'Anemometer','Quadrotor'},'FontSize',12)
```

Bibliography

[1] Frsky electronic co., ltd. https://www.frsky-rc.com/, . Accessed: 2017-10-31.

[2] Maps of Tromsø. kart.kystverket.no, . Accessed: 2018-03-30.

[3] Pixhawk autopilot. https://pixhawk.org/modules/pixhawk, . Accessed: 2017-10-30.

[4] De Havilland Aircraft Museum - Queen Bee. http://www.dehavillandmuseum.co.uk/aircraft/de-havilland-dh82b-queen-bee/, . Accessed: 2017-11-07.

[5] Ira H. Abbott and A. E. von Doenhoff. *Theory of Wing Sections, Including a Summary of Airfoil Data*. Dover Publications, Inc., 1959.

[6] G. Allibert, D. Abeywardena, M. Bangura, and R. Mahony. Estimating body-fixed frame velocity and attitude from inertial measurements for a quadrotor vehicle. pages 978–983, 2014. doi: 10.1109/CCA.2014.6981462. URL https://www.scopus.com/inward/record.uri?eid=2-s2.0-84920517886&doi=10.1109%2fCCA.2014.6981462&partnerID=40&md5=0a32c24f41512b3bcbd3826c3a7fb6b3. cited By 6.

[7] ArduPilot. Downloading and analyzing data logs in mission planner. http://ardupilot.org/copter/docs/common-downloading-and-analyzing-data-logs-in-mission-planner.html, . Accessed: 2017-10-20.

[8] ArduPilot. Flight modes. http://ardupilot.org/copter/docs/flight-modes.html, . Accessed: 2017-11-06.

[9] ArduPilot. Mission Planner. http://ardupilot.org/planner/index.html, . Accessed: 2018-04-02.

[10] International Civil Aviation Authority. Unmanned Aircraft Systems (UAS). *Circular 328*, 2011.

[11] *Regler for flyging med luftfartøy som ikke har fører ombord innenfor Tromsø kontrollsone*. Avinor, 3. edition, March 2017. URL https://avinor.no/konsern/pa-flyplassen/droner/kart-og-restriksjoner.

[12] M. Bangura and R. Mahony. Nonlinear dynamic modeling for high performance control of a quadrotor. 2012. URL https://www.scopus.com/inward/record.uri?eid=2-s2.0-84879951924&partnerID=40&md5=59f20b54dfac10374d182b615c9ffea5. cited By 45.

[13] M. Bangura, H. Lim, H.J. Kim, and R. Mahony. Aerodynamic power control for multirotor aerial vehicles. pages 529–536, 2014. doi: 10.1109/ICRA.2014.6906906. URL https://www.scopus.com/inward/record.uri?eid=2-s2.0-84929163334&doi=10.1109%2fICRA.2014.6906906&partnerID=40&md5=392977f3a9f50465c8ec10e8871dbe65. cited By 13.

[14] Moses Bangura, Marco Melega, Roberto Naldi, and Robert Mahony. Aerodynamics of rotor blades for quadrotors. *arXiv.org*, 2016. URL https://arxiv.org/abs/1601.00733.

[15] R.W. Beard and T.W. McLain. *Small unmanned aircraft: Theory and practice*. 2012. URL https://www.scopus.com/inward/record.uri?eid=2-s2.0-84884103949&partnerID=40&md5=45bcb710bd658f8ff819e7905028e9ec. cited By 259.

[16] Christina Beller. *Urban Wind Energy*. PhD thesis, Danmarks Tekniske Universitet, Risø Nationallaboratoriet for Bæredygtig Energi, 2011.

[17] Godfrey Boyle. *Renewable Energy - Power for a sustainable future*. Oxford University Press, third edition edition, 2012. ISBN 9780199545339.

[18] W L Chan, C S Lee, and F B Hsiao. Real-time approaches to the estimation of local wind velocity for a fixed-wing unmanned air vehicle. *Measurement Science and Technology*, 22(10):105203, 2011. URL http://stacks.iop.org/0957-0233/22/i=10/a=105203.

[19] Civil Aviation Authority - Norway. Regulations concerning aircraft without a pilot on board etc, December Published: 2015. URL http://luftfartstilsynet.no/caa_no/Regulations_concerning_aircraft_without_a_pilot_on_board_etc. Updated: 15.02.2016.

[20] Engineering ToolBox. Air - density, specific weight and thermal expansion coefficient at varying temperature and constant pressures. https://www.engineeringtoolbox.com/air-density-specific-weight-d_600.html, 2003. Accessed: 2018-05-05.

[21] *WindSonic User Manual - Ultrasonic Anemometer*. Gill Instruments Limited, Saltmarsh Park, 67 Gosport Street, Lymington, Hampshire, SO41 9EG, UK, December 2015. URL www.gillinstruments.com. Issue 22 Doc No: 1405-PS-0019.

[22] J. Gonzalez-Rocha, C.A. Woolsey, C. Sultan, N. Rose, and S.F.J. De Wekker. Measuring atmospheric winds from quadrotor motion. 2017. URL https://www.scopus.com/inward/record.uri?eid=2-s2.0-85017404471&partnerID=40&md5=cf16716903c7842bd3565ec5a32b9478. cited By 2.

[23] David Halliday, Robert Resnick, and Walker Jearl. *Fundamentals of Physics*. Von Hoffmann Press, 7th edition edition, 2005. ISBN 0-471-23231-9.

[24] Trond Ola Hågbo. Optimization of wind turbine location in urban environment. Master's thesis, UiT The Arctic University of Norway, Tromsø, June 2017.

[25] Jinhua SunMaster Solar Technology Co. Ltd. Vertical Axis Wind Turbines vs. Horizontal Axis Wind Turbines. https://www.solarlightsmanufacturer.com/vertical-and-horizontal-axis-wind-turbines/, 2017. Accessed: 2018-05-07.

[26] LabSat. GPS Time Calculator. https://www.labsat.co.uk/index.php/de/gps-time-calculator. Accessed: 2018-04-17.

[27] J.F. Manwell, J.G. McGowan, and A.L. Rogers. *Wind Energy Explained: Theory, Design and Application*. 2010. doi: 10.1002/9781119994367. URL https://www.scopus.com/inward/record.uri?eid=2-s2.0-84891584221&doi=10.1002%2f9781119994367&partnerID=40&md5=973b89f7ecf71f6f797ee11e2695916a. cited By 1234.

[28] M. Marino, A. Fisher, R. Clothier, S. Watkins, S. Prudden, and C.S. Leung. An evaluation of multi-rotor unmanned aircraft as flying wind sensors. *International Journal of Micro Air Vehicles*, 7(3):285–300, 2015. URL https://www.scopus.com/inward/record.uri?eid=2-s2.0-84959928508&partnerID=40&md5=d41529008ffc77bb9d51039eb5866837. cited By 5.

[29] Håvard Mjøen. *Pilot Operating Handbook IRIS+*. UiT The Arctic University of Norway, 2017.

[30] National Coordination Office for Space-Based Positioning, Navigation and Timing. GPS: The Global Positioning System. https://www.gps.gov/, 2017. Accessed: 2018-05-06.

[31] Vaughn Nelson. *Wind Energy: Renewable Energy and the Environment*. CRC Press, 2009.

[32] Patrick P. Neumann and Matthias Bartholmai. Real-time wind estimation on a micro unmanned aerial vehicle using its inertial measurement unit. *Sensors and Actuators A: Physical*, 235(Supplement C):300 – 310, 2015. ISSN 0924-4247. doi: https://doi.org/10.1016/j.sna.2015.09.036. URL http://www.sciencedirect.com/science/article/pii/S0924424715301539.

[33] M. Pachter, N. Ceccarelli, and P.R. Chandler. Estimating mav's heading and the wind speed and direction using gps, inertial, and air speed measurements. 2008. URL https://www.scopus.com/inward/record.uri?eid=2-s2.0-78651102570&partnerID=40&md5=845d367f3cd14d9e36f7ec7f7967b0d6. cited By 15.

[34] H. J. Palanthandalam-Madapusi, A. Girard, and D. S. Bernstein. Wind-field reconstruction using flight data. In *2008 American Control Conference*, pages 1863–1868, June 2008. doi: 10.1109/ACC.2008.4586763.

[35] Ross T. Palomaki, Nathan T. Rose, Michael van den Bossche, Thomas J. Sherman, and Stephan F. J. De Wekker. Wind estimation in the lower atmosphere using multirotor aircraft. *Journal of Atmospheric and Oceanic Technology*, 34(5):1183–1191, 2017. doi: 10.1175/JTECH-D-16-0177.1. URL https://doi.org/10.1175/JTECH-D-16-0177.1.

[36] Yuriy Posudin. *Measurement of Wind Parameters*, pages 38–56. John Wiley and Sons, Inc., 2014. ISBN 9781118914236. doi: 10.1002/9781118914236.ch4. URL http://dx.doi.org/10.1002/9781118914236.ch4.

[37] *Dynamometer Series 1580 Assembley Manual 1.13*. RCbenchmark.com.

[38] *SpaceLogger.S10 User Manual*. Richard Paul Russell Ltd, The Lodge, Unit 1 Barnes Farm Business Park, Barnes Lane, Milford on Sea SO41 0AP UK, March 2015. URL www.spacelogger.com. 017SL167/7.

[39] J. Seddon and S. Newman. *Basic Helicopter Aerodynamics: Third Edition*. 2011. doi: 10.1002/9781119994114. URL https://www.scopus.com/inward/record.uri?eid=2-s2.0-84891565497&doi=10.1002%2f9781119994114&partnerID=40&md5=2c97ccdbfa913dc68ceab6e132db6385. cited By 26.

[40] TE Connectivity. SS Cap Altimeter Pressure Sensor. http://www.te.com/usa-en/product-CAT-BLPS0036.html?q=MS5611&source=header#guest-click, 2017. Accessed: 2018-05-07.

[41] Tzivaras Vasilis. *Building a Quadcopter with Arduino*. 2006. ISBN 978-1-78528-184-6. URL `http://proquestcombo.safaribooksonline.com/book/hardware/arduino/9781785281846`.

[42] S.L. Waslander and C. Wang. Wind disturbance estimation and rejection for quadrotor position control. 2009. URL `https://www.scopus.com/inward/record.uri?eid=2-s2.0-77958473029&partnerID=40&md5=acccc58acec46137ac0e64e1e92f4ed8`. cited By 57.

[43] C. A. Wolf, R. P. Hardis, S. D. Woodrum, R. S. Galan, H. S. Wichelt, M. C. Metzger, N. Bezzo, G. C. Lewin, and S. F. J. de Wekker. Wind data collection techniques on a multi-rotor platform. In *2017 Systems and Information Engineering Design Symposium (SIEDS)*, pages 32–37, April 2017. doi: 10.1109/SIEDS.2017.7937739.